

**MICROPHOTONIC RF RECEIVER COMPONENTS
FINAL TECHNICAL REPORT**

Contract number: N00014-00-1-0458

Research Period: April 1, 2000 – March 31, 2004

Organization: University of Southern California

Principal Investigator: Prof. A.F.J. Levi
Advanced Interconnect and Network Technology
3620 S. Vermont Ave., KAP 132
Los Angeles, CA 90089-2533
voice: (213) 740-7318
fax: (213) 740-9280
email: alevi@usc.edu

USC Contract Administrator: Ms. Lourdes Creus
Dept of Contracts & Grants
University Park - STO 324
Los Angeles, CA 90089-1147
voice: (213) 740-6058
fax: (213) 740-6070
email: creus@usc.edu

BEST AVAILABLE COPY

DISTRIBUTION STATEMENT A
Approved for Public Release
Distribution Unlimited

20040623 016

FINAL TECHNICAL REPORT

Microphotonic RF receiver components

Award number N00014-00-1-0458

Start date 4.1.00

End date 3.31.04

Organization of this report

This report consists of three main sections: Part I introduces the LiNbO₃ microdisk optical modulator. In this section the microdisk optical resonator, the RF ring resonator and their electro-optic interaction is explained. Part II covers the experimental demonstration of LiNbO₃ microdisk modulator performance in wired and wireless RF-optical links. Part III outlines a novel microphotonic RF receiver architecture that exploits the nonlinear modulation in a LiNbO₃ microdisk to achieve direct photonic down-conversion from a RF carrier without using any high-speed electronic elements.

Introduction

The main objective of the microphotonic receiver project was to design and build a new type of radio frequency (RF) receiver based on the electro-optic response of a high- Q microdisk optical modulator. The high sensitivity of the microdisk modulator is a result of simultaneous optical and electrical resonance. The microdisk optical resonator provides the spatial confinement and long photon lifetime to ensure high optical sensitivity in a small volume, while a miniature RF resonator generates an amplified electric field. The electric field modulates the refractive index of the microdisk and consequently the intensity of the optical output. By optimizing the RF and optical design we were able to build a very sensitive LiNbO₃ microdisk optical modulator operating at Ku-band. The next challenge was creating a microphotonic receiver architecture that could use the sensitivity of the microdisk modulator to replace the high-speed electronic elements used in a conventional RF receiver with photonic devices and low-speed electronics. Based on the idea of nonlinear optical modulation in a microdisk modulator, we designed and demonstrated a photonic RF receiver that directly extracts baseband information from the received RF signal by using only a laser, LiNbO₃ microdisk modulator, and a low-speed photodetector. The Ku-band RF wireless receiver uses no high-speed transistors.

Part I:

LiNbO₃ microdisk optical resonator

Crystalline Lithium Niobate (LiNbO₃) is a commonly used electro-optic material in optical modulators. Its excellent optical, electrical and mechanical characteristics such as low loss at RF and optical frequencies, high electro-optic coefficient, mechanical robustness and stable crystal structure at room temperature make LiNbO₃ an ideal candidate in many electro-optical devices. We chose LiNbO₃ for our proof of principle experiments. Some of the relevant opto-electronic properties of LiNbO₃ are summarized in Table 1 [1-4].

A LiNbO₃ microdisk optical resonator supports very high- Q Whispering-Gallery (WG) resonances. The microdisk resonator is fabricated from a z-cut LiNbO₃ cylinder. As shown in Fig. 1(a), the basic geometry is a disk of radius R , and thickness t . Devices we tested have $0.1 \text{ mm} < t < 1 \text{ mm}$ and $1 \text{ mm} < (D = 2R) < 6 \text{ mm}$. The sidewall of the disk is optically polished

with a radius of curvature R , typically equal to the radius of the disk. In addition, the equator of the disk's sidewall should be accurately maintained at height $t/2$.

Table 1 [1-4]

Property	Value	Notes
Ordinary optical index of refraction (n_o)	2.223	$\lambda = 1550$ nm
Extraordinary optical index of refraction (n_e)	2.143	$\lambda = 1550$ nm
RF permittivity along c -axis ($\epsilon_{RF,e}$)	42.5 - 43	100 MHz - 140 GHz
RF permittivity perpendicular to c -axis ($\epsilon_{RF,o}$)	26-28	100 MHz - 140 GHz
Electro-optic coefficients (pm/V)	$r_{33} = 30.8$ $r_{22} = 3.4$ $r_{13} = 8.6$ $r_{51} = 28.0$	
Dielectric loss tangent along c -axis	0.004	

Using advanced optical polishing techniques we were able to acheive optical-quality curved sidewalls of LiNbO₃ microdisks that resulted in high- Q optical resonances.

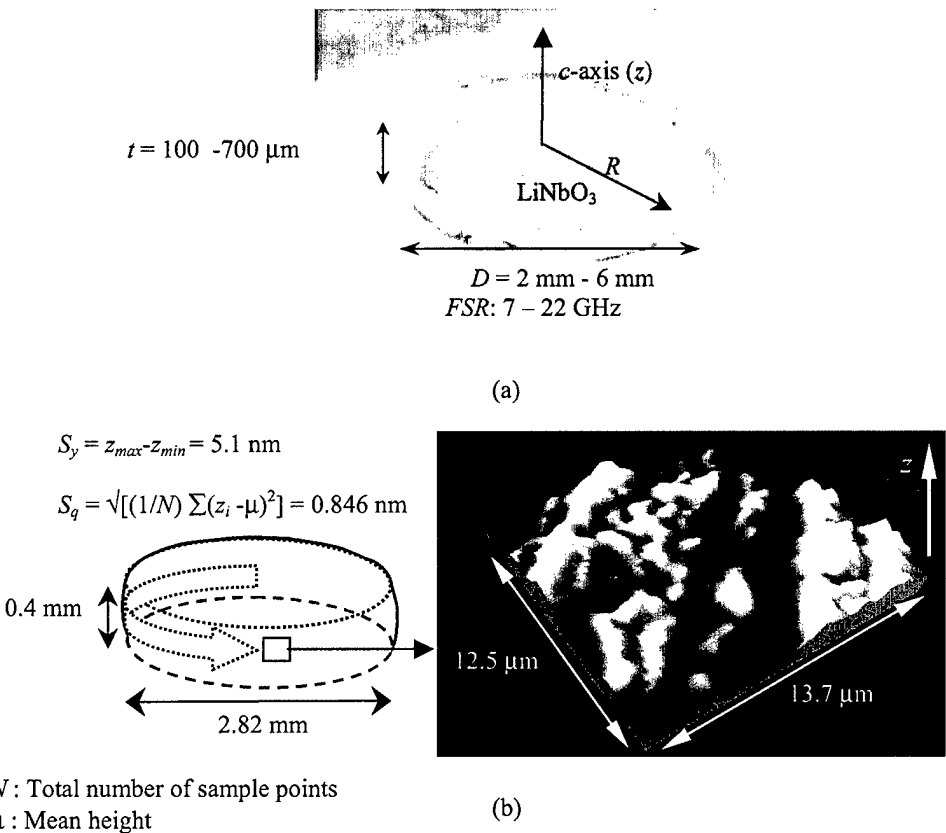


Figure 1 (a) Photograph of a LiNbO₃ disk with optically polished sidewalls. (b) 3D picture of the disk sidewall surface taken by interferometric surface profilometer.

The technology has been transferred to a company so that now one may purchase very small high- Q ($>10^6$) LiNbO₃ microdisk optical resonators ($D = 1$ mm and $t = 0.150$ mm).

Fig. 1(b) shows a 3D picture of the sidewall surface roughness for a typical microdisk (taken with an *interferometric surface profiler*). The peak-to-peak value (S_p) of surface roughness is about 5.1 nm and its rms value (S_q) is about 0.846 nm. With this surface quality loaded optical- Q s up to 7×10^6 (unloaded Q of about 2×10^7) have been achieved. This corresponds to a distributed loss of less than 0.0075 cm^{-1} (or 0.03 dB/cm). Since LiNbO₃ is an electro-optic active material its refractive indices change in the presence of an electric field. An E -field with a magnitude E_c along the c -axis changes the optical refractive indices according to:

$$\Delta n_{zz} = n_{eo}^3 r_{33} E_c / 2 \quad \Delta n_{xy} = n_{oo}^3 r_{13} E_c / 2$$

where $r_{33} \approx 30.8 \times 10^{-12} \text{ m/V}$ and $r_{13} \approx 8.6 \times 10^{-12} \text{ m/V}$.

An optical mode in a sphere is described in terms of three integers l , m and q . The value of q is the number of field maxima in the radial direction and $l - m + 1$ ($|m| \leq l$) is the number of field maxima in the polar direction, perpendicular to equatorial plane and between two poles [7-9]. The resonant frequency ($\nu_{res} = \nu_{l,q}$) is determined by q and l . The mode labeled by $l = m$ and $q = 1$ is called the fundamental Whispering Gallery (WG) mode. It has only one maximum in each direction and has a Gaussian profile.

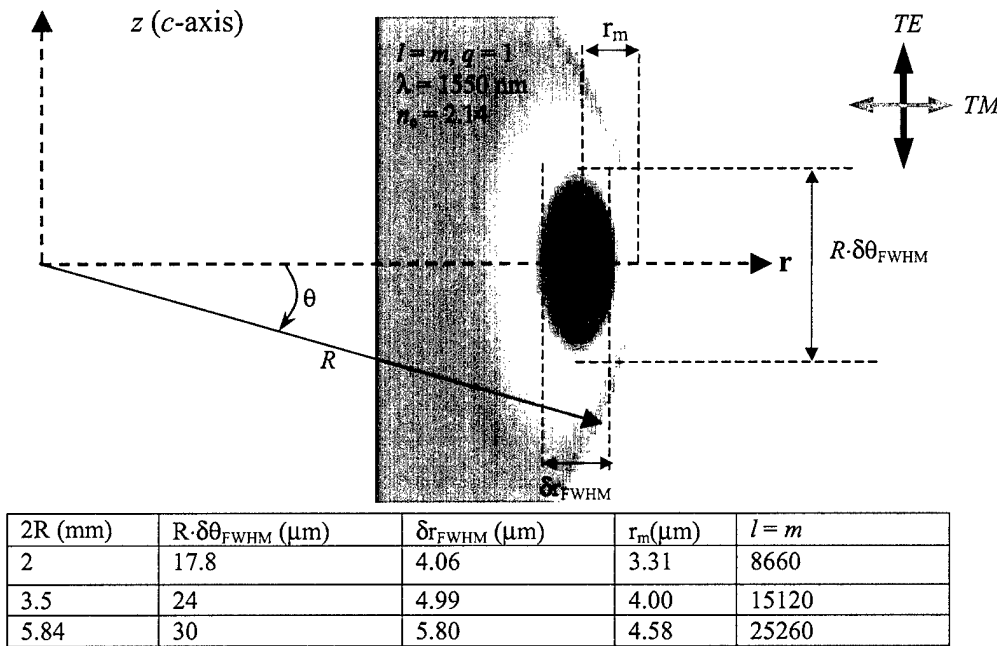


Figure 2 WGM power distribution in xz plane, for microdisks with different diameters [5]. Notice that θ is measured relative to the equatorial plane unlike the conventional definition that is measured relative to z axis. This new definition has been chosen because it is more convenient for WG resonances that are confined around the equator. Also shown is the definition of the TE and TM polarized resonances relative to c -axis.

Fig. 2 shows the definition of the fundamental mode profile parameters and their values for three LiNbO₃ microdisks with different sizes commonly used in our experiments [5]. δr_{FWHM} is the

full-width-half-maximum of the power distribution along radial direction and $\delta\theta_{FWHM}$ is the full width half maximum along polar direction.

The resonant frequency of the fundamental WG resonance and other low order resonances may be calculated using the approximation: $m(\lambda/n) = 2\pi R$, in which m is the number wavelengths around the periphery of the microdisk and n is the optical index of refraction. The optical free spectral range (FSR) frequency $\Delta\nu_{FSR}$ may be calculated using: $\Delta\nu_{FSR} = c/(2\pi nR)$.

The optical modes with an E -field polarized parallel to the c -axis are labeled as TE and those with an E -field parallel to the xy plane are labeled as TM modes. Due to the large magnitude of the electro-optic coefficient along c -axis we always use TE polarized WG modes for optical modulation.

Assuming the number of photons present in a WG mode decay exponentially in time we can express the unloaded optical quality factor of that mode as $Q_u = \omega\tau_p$ where τ_p is the 1/e photon lifetime and $\omega = 2\pi\nu_{l,q}$ (where $\nu_{l,q}$ is the resonant frequency of the mode). We can also define a distributed loss constant per unit length $\alpha = n/c\tau_p$ in which c is the speed of light and n is the effective optical refractive index for the corresponding optical mode. So Q_u and the distributed loss are related as: $\alpha = n\omega/cQ_u$. The loaded optical quality factor Q of a mode can be calculated based on the measured full-width half maximum of the spectral peak at the resonant optical frequency $\nu_{res} = \nu_{l,q}$, $Q = \nu_{res}/\Delta\nu_{FWHM}$ (or $Q = \lambda_{res}/\Delta\lambda_{FWHM}$). The typical loaded Q -factor values that we observe for optically polished LiNbO₃ microdisks is between 2×10^6 and 7×10^6 . Experimentally we measure the loaded Q so if we use the measured value of Q to calculate α , the optical coupling loss will be included in the distributed loss.

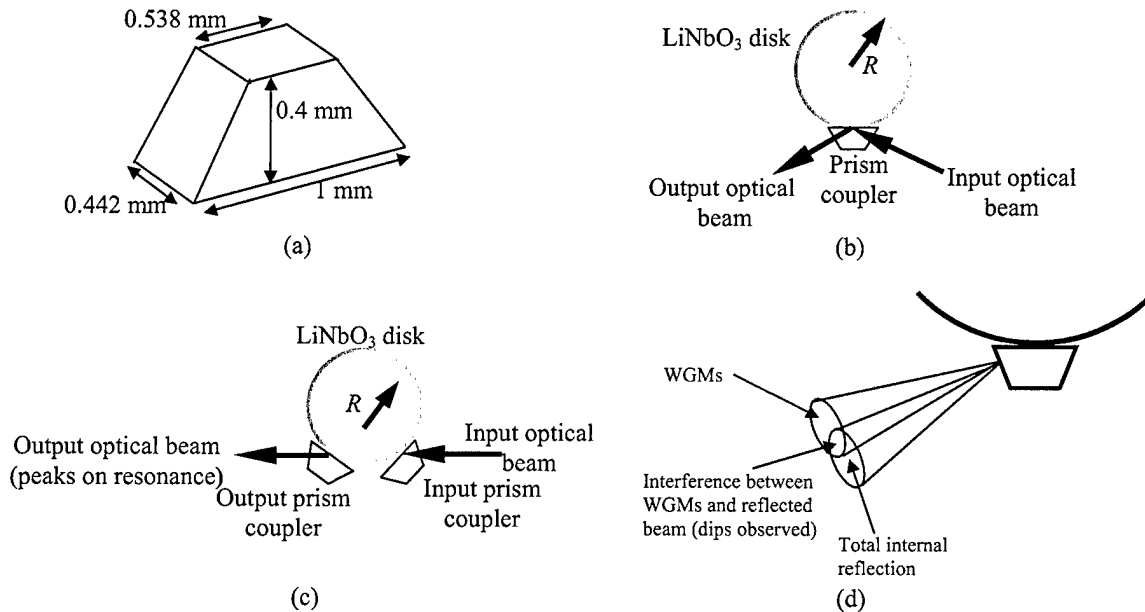


Figure 3 (a) Diamond microprism dimensions. (b) Single-prism coupling. (c) Double-prism coupling. (d) Interference effect in single-prism coupling.

Knowing the loaded quality factor of a critically coupled WG mode we were able calculate the intrinsic distributed loss in the microdisk resonator.

In our experiments we use evanescent coupling through small diamond prisms with dimensions shown in Fig. 3(a). The refractive index of diamond is about 2.4. This is larger than the refractive index of LiNbO₃ for both TE and TM modes ($n_e = 2.14$, $n_o = 2.23$). It is possible to use a single prism to couple light into and out of the microdisk (Fig. 3(b)) or use one prism to couple in and another one for coupling out (Fig. 3(c)). Detection of coupled WG peaks using two prisms is easier since the reflected (part of the input that is not coupled) and coupled light don't interfere. However, when two prisms are in contact with microdisk the Q is smaller (due to larger coupling loss) and also part of the optical WGM power that is coupled out through the first prism can't be used for modulation. In a one-prism coupling scheme this problem doesn't exist but experimental results show that the WGM cone coupled out of the disk and the totally reflected beam cone have spatial overlap (Fig. 3(d)), so depending on the location of the collecting fiber the detected output spectrum can be WGM peaks, transmission dips or just the reflected beam. This effect makes the alignment of the optical output more complex. Experimental results show two-prism coupling results in a cleaner mode structure. Using transmission dips in a one-prism coupling scheme is a better choice for nonlinear modulation and optical down-conversion due to reduced DC optical power at resonance.

Fig. 4(a) shows close up photographs of the microdisk, the microprisms and the output fiber. Here, a double-prism coupling scheme is used. The input light is a laser beam of wavelength $\lambda = 1550$ nm and a linewidth of less than 500 kHz. Due to high- Q nature of the optical resonance a very high resolution tunable laser is required for accurate alignment with the resonant wavelength. The resolution of the laser used in our experiments is less than < 0.3 pm. The laser beam is collimated and then focused on the input microprism using a matched pair lens system with a focal length of 11 mm. Fig. 4(b) shows the typical TE optical output spectrum obtained in a double prism configuration. This spectrum is measured using the LiNbO₃ microdisk in Fig. 4(a). The disk has a diameter of 5.13 mm and a thickness of 0.4 mm. The measured FSR is in very good agreement with the calculated value (assuming $n_{eo} = 2.14$). For the 5.13 mm diameter disk the calculated value is 69.24 pm and the measured value is 67.87 pm. This shows the effective refractive index of TE WG modes is almost the same as the bulk extraordinary refractive index (E -field along c -axis). The maximum optical coupling efficiency observed is about 15%. We define the coupling efficiency as the ratio of the resonant optical power of an optical mode and the total power injected to the input prism. As mentioned before using a one prism coupling scheme the optical spectrum of the collected output power could be a series of transmission dips or peaks depending on the position of the output fiber. Fig. 4(c) and (d) show the spectrum of the TE optical output power from a single prism coupled LiNbO₃ microdisk ($D = 3$ mm, $h = 0.4$ mm). In Fig. 4(c) the output fiber is located at the overlap of the WG cone and the totally reflected cone while in Fig. 4(d) it only collects the WG optical power.

If we place a conductive ring on top of a microdisk application of a DC voltage on the ring can generate an E -field (mainly along z -direction) around the disk where the WG modes are propagating. Since LiNbO₃ is an electro-optic material the E -field changes its refractive index and consequently the resonant wavelengths (frequencies) of WG modes. The magnitude of this

shift can be estimated as: $\Delta\lambda_m = \lambda_m n_{eo}^2 r_{33} E_{eff} / 2$. Here, E_{eff} is the magnitude of the E -field along z -axis in the middle of microdisk where the WG mode propagates. Ideally in the absence of fringing and other perturbing factors the E -field intensity in the middle of the disk should be equal to V/t . However, due to fringing effect E -field and the air gap between the ring and the microdisk surface the E -field intensity inside LiNbO_3 is less than the ideal value.

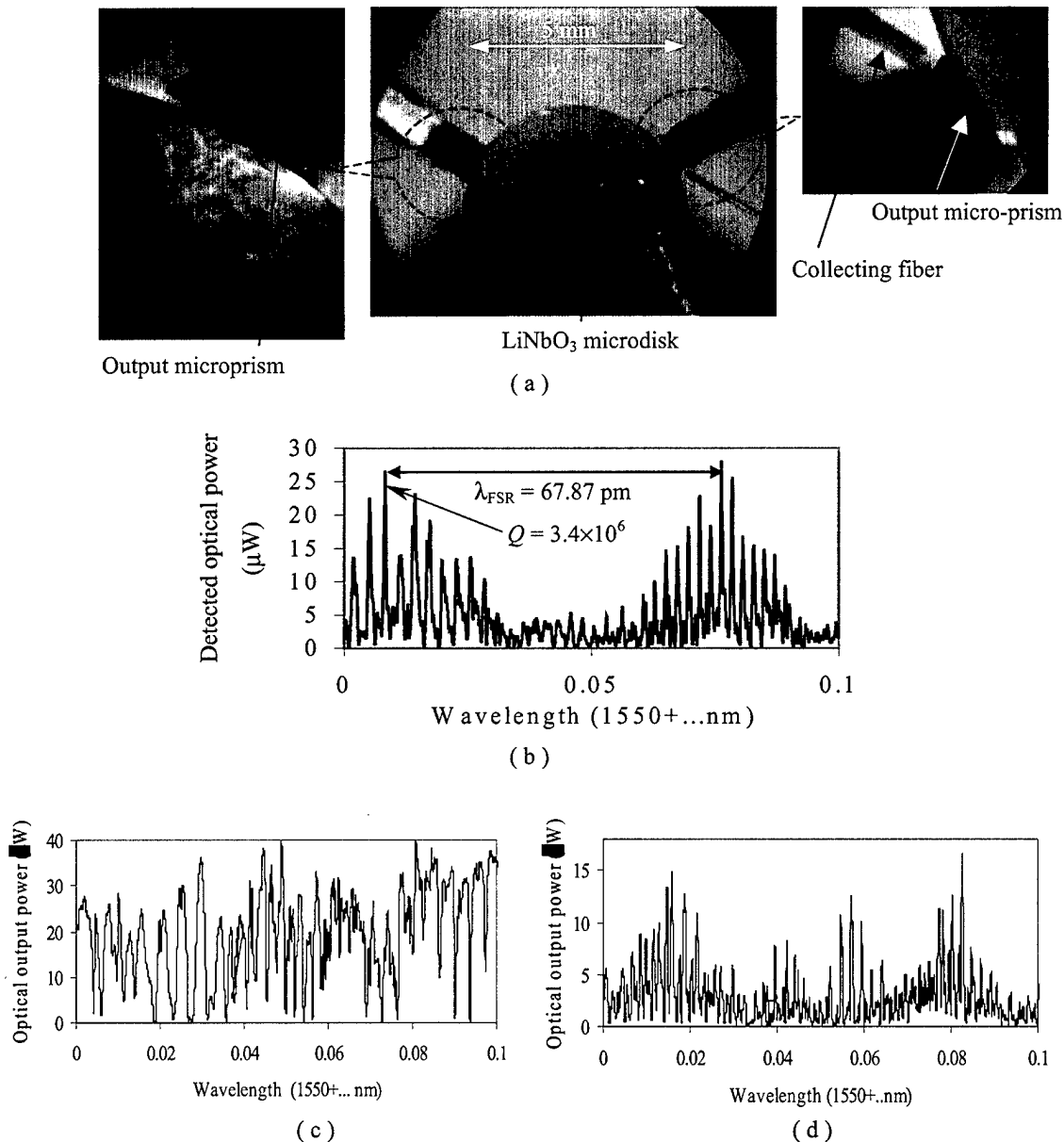


Figure 4 (a) Photograph of a 5.13 mm diameter LiNbO_3 microdisk in contact with two microprisms. (b) The detected TE WG optical output power spectrum. (c) and (d) are the measured optical out power spectrum of a single prism coupled LiNbO_3 microdisk ($D = 3 \text{ mm}$, $h = 0.4 \text{ mm}$). (c) Detected transmission dips when the output fiber is tuned to the overlap region of the WG cone and the total reflection cone. (d) Detected WG peaks when the output fiber only collects optical power from the WG cone

We summarize all these effects and the overlap integral between optical mode and the E -field in a correction factor called the optical-mode-electric-field overlap correction factor β_{EO} so: $E_{eff} = \beta_{EO}(V/t)$. When $V = 1$ V, $\Delta\lambda_m$ is called DC shift or $\Delta\lambda_{DC}$. DC shift is an important parameter in a microdisk modulator because it quantifies the electro-optic response of the modulator and is needed for calculating the RF modulation response. The measured value of DC shift for a WG resonance can be used to estimate the corresponding β_{EO} . The desired value of β_{EO} should be close to 1 but in most cases it is less than 0.5. β_{EO} is determined by many parameters and it also varies slightly for different WG resonances. It is possible to improve β_{EO} by using a geometry that forces the E-fields to overlap the optical mode region. To help achieve this, we mount the microdisk on a cylindrical ground plane with the same radius as the disk. Fig. 5(a) shows a photograph of a microdisk resonator ($D = 3$ mm, $h = 0.4$ mm) mounted on a cylindrical ground plane. Fig. 5(b) shows the measured optical output spectrum of the microdisk (shown in Fig. 5(a)) at 0 V and 5 V DC bias voltage. The resonator is coupled through a single-prism but the output fiber is tuned to the WG cone to detect the peaks. As may be seen $\Delta\lambda_{DC} = 0.13$ pm (corresponding to $\beta_{EO} = 0.53$).

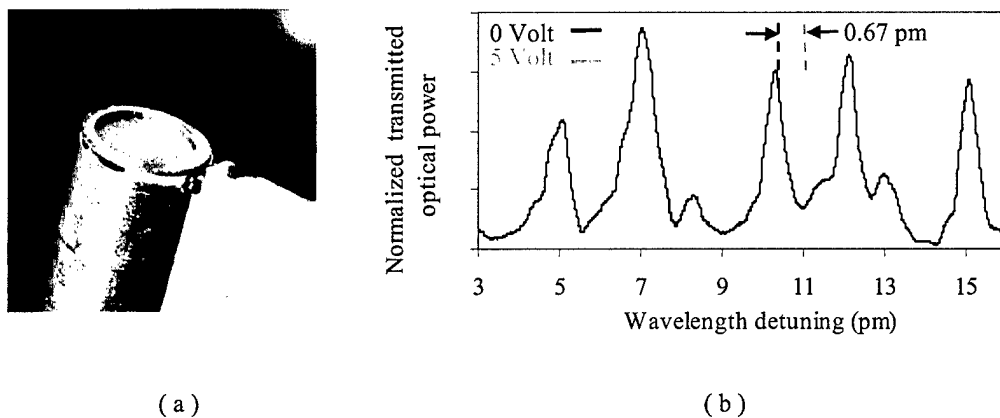


Figure 5 (a) Photograph of the microdisk resonator mounted on a cylindrical ground plane ($D = 3$ mm, $t = 0.4$ mm). (b) Measured optical output spectrum at 0 and 5 Volt DC bias voltage.

Bistable optical devices are of interest for their possible application to optical computing, optical thresholding and memory [10-11]. As an example of the slow electro-optic response of the microdisk modulator we have demonstrated the bistable behavior of the LiNbO_3 microdisk resonator with a feedback loop. This differs from the Fabry-Perot case [12] because we are using a traveling wave resonator. The reason for our interest is that the high optical Q should, in principle, make a sensitive device. The microdisk resonator has a diameter of 5.8 mm and a thickness of 0.74 mm. The measured DC shift for this configuration is about 0.09 pm/V. The experimental arrangement to measure electro-optic non-linearity is shown in Fig. 6(a). The voltage applied to the electrode is a function of resonator optical output power. Optical input power to the resonator is provided by a frequency-stabilized laser diode whose output is intensity modulated to create a 500 Hz triangle wave. Optical output power is detected using a photodiode. To study electro-optic bistability, amplified detector output voltage is fed back to the disk electrode. Fig. 6(b) shows the measured optical output-power as a function of optical input-power for the indicated values of peak-to-peak voltage feed-back, V_{fb} and optical Q -factor.

The electro-optic system shows a slight non-linearity when $V_{fb} = 1.5 V_{pp}$, using an optical mode with $Q = 7.5 \times 10^5$, and significant bistability and hysteresis behavior when $V_{fb} = 3.0 V_{pp}$, using an optical mode with $Q = 10^6$.

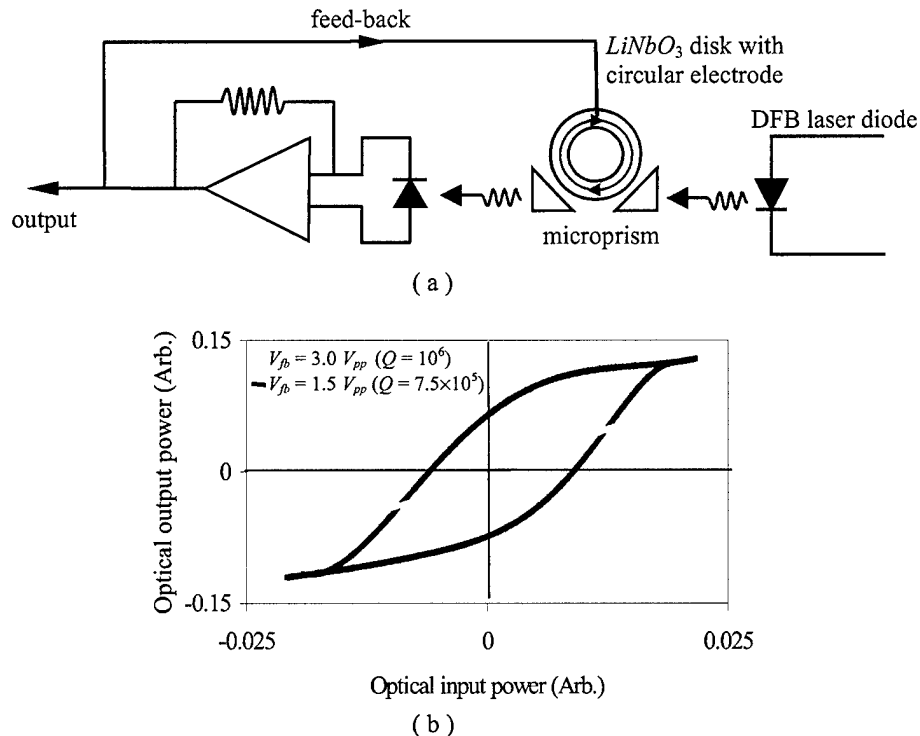


Figure 6 (a) Experimental arrangement used for demonstrating the bistable behavior of the microdisk optical resonator with a feed-back loop. (b) Measure optical output-power as a function of optical input-power for indicated values of peak-to-peak voltage feedback (V_{fb}) and optical Q -factor

RF resonator

The key characteristics of the modulating E -field for an efficient electro-optic interaction with WG modes inside the disk may be summarized as:

- 1) Oscillation frequency equal to $m_o \times \Delta\nu_{FSR}$
(m_o is an integer representing the order optical modulation)
- 2) Proper spatial distribution.
- 3) Large interaction length.
- 4) Large magnitude.
- 5) Good overlap with the optical mode (large β_{EO}).

The role of a good RF resonator is to generate an E -field that satisfies all these requirements. The first necessary condition for simultaneous RF and optical resonance in a microdisk modulator is $f_{RF} = m_o \times \Delta\nu_{FSR}$ or *RF-optical frequency matching condition* (f_{RF} is the RF resonant frequency). The resonant optical modulator can only modulate light at frequencies below Q/ν_{res} where Q is the optical quality factor and ν_{res} is the optical resonant frequency, or frequencies within a limited bandwidth ($< Q/\nu_{res}$) around integer multiples of its free-spectral-range ($\Delta\nu_{FSR}$). Proper spatial distribution, large interaction length and large magnitude of the E -field around the microdisk are required to maximize the electro-optical phase shift at each photon round trip. It is

very important to notice that in a conventional Mach-Zehnder (MZ) modulator both optical and electrical waves are traveling along an open linear trajectory and they are velocity matched for broadband operation. In contrast, in a microdisk modulator the optical wave is a traveling wave that circulates around the microdisk. Given the large difference between the RF resonant wavelength, $\lambda_{RF} = c/(n_{RF,e} \times \Delta v_{FSR})$ ($n_{RF,e}$ is the effective RF refractive index for the corresponding resonance), and resonant optical wavelength, $\lambda_{res} = c/(n_e v_{res})$ the RF field becomes a standing wave. A microstrip RF ring resonator on top of the microdisk can fulfill all of these requirements with minimum complexity. Fig. 7(a) shows a schematic diagram of the microdisk modulator that employs a ring resonator. The ring is placed on the LiNbO₃ microdisk and is side-coupled to a microstripline. Fig 7(b) shows a photograph of our experimental arrangement. The microdisk has an FSR of 14.6 GHz and its dimensions and ground plane geometry are the same as Fig. 5.

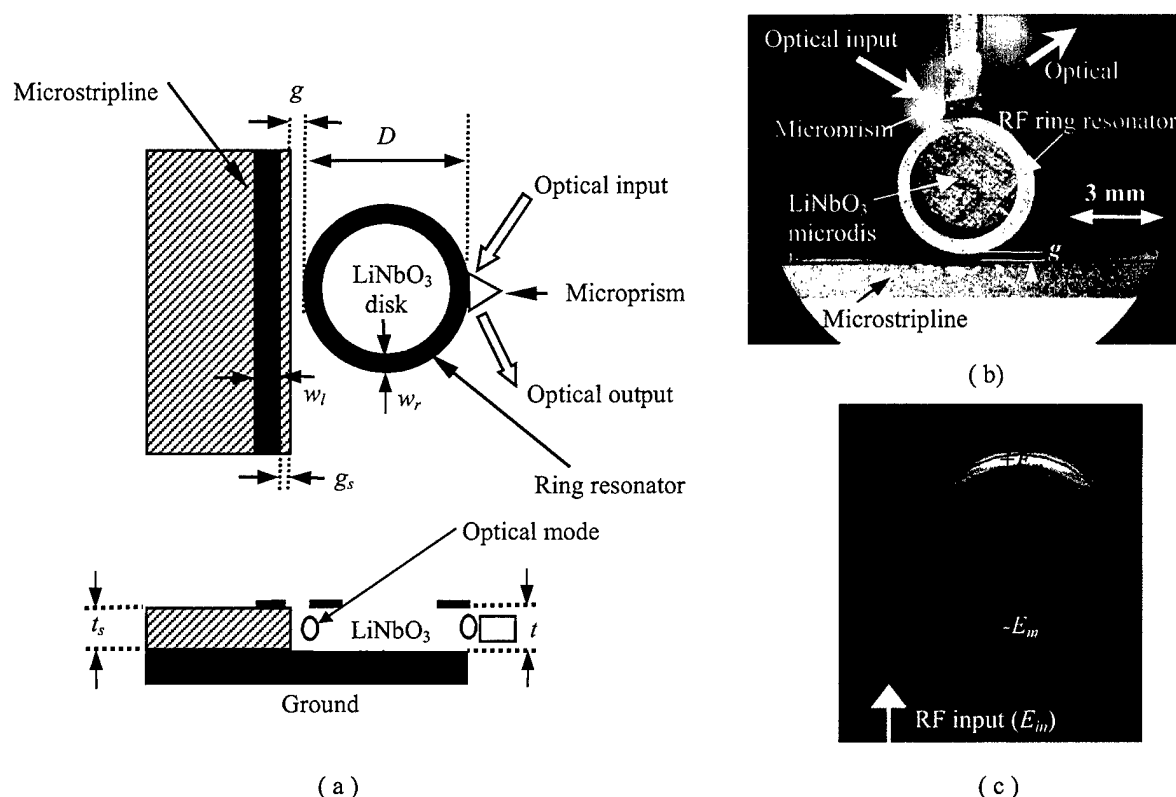


Figure 7 (a) Geometry of ring resonator on LiNbO₃ side-coupled to a microstripline (top view and side view) (b) Photograph of our latest experimental arrangement. The microdisk has an FSR of 14.6 GHz and its dimensions and ground plane geometry are the same as Fig. 5(a). (c) Simulated E -field distribution on the equatorial plane of the LiNbO₃ microdisk while the fundamental resonance of the ring resonator is excited

When a ring resonator is strongly coupled to a microstripline (small gap sizes) the symmetry breaks due to the proximity of the microstripline. The broken symmetry splits each mode into even and odd modes with slightly different resonant frequencies. Odd modes have lower frequencies and are capacitively coupled to the line, while the even modes have higher frequencies and are magnetically coupled to the line [15]. The coupling strength dependence on mode order and coupling mechanism results in different loading factors and hence different

frequency shifts and loaded Q s. Both even and odd modes can be used for optical modulation but since in most cases the resonant frequency of the even mode is closer to $\Delta\nu_{\text{FSR}}$ we use even mode.

Because of the large difference between RF and optical refractive index of LiNbO_3 ($n_{\text{RF}} = 5.1$, $n_e = 2.14$) an important challenge is matching the RF to the optical resonance. Using a combination of physical factors that influence the RF resonant frequency of the ring resonator on a dielectric disk we are able to tune the fundamental resonant frequency ($f_{\text{RF}} = f_{\text{RF},1}$) of the side-coupled ring resonator to $\Delta\nu_{\text{FSR}}$. Assuming $f_{\text{RF},1} = \Delta\nu_{\text{FSR}}$ then the harmonics of the ring resonator, $f_{\text{RF},m} = m_R \times f_{\text{RF},1}$, may be used for harmonic optical modulation at $m_R \times \Delta\nu_{\text{FSR}}$. Fig. 7(c) shows the simulated E -field distribution on the equatorial plane of the LiNbO_3 microdisk while the fundamental resonance of the ring resonator is excited. The sinusoidal spatial distribution and RF-optical frequency matching results in a phase matched electro-optic interaction and optimized optical modulation efficiency.

The ring resonator performance is evaluated by measuring the S -parameters of the coupled microstripline. We have estimated the voltage gain of the ring resonator as a function of measurable parameters in the system:

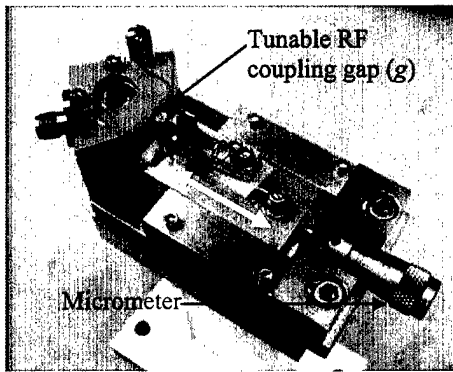
$$G_V = \frac{V_m}{V_o} = \sqrt{\frac{4tP_{\text{loss}}Q_{\text{RF},U}}{\beta_c Z_o \omega_{\text{RF}} \epsilon_{e,\text{RF}} \epsilon_0 A}}$$

V_m : Amplitude of the voltage oscillation on the ring resonator	$\epsilon_{\text{RF},e}$: RF permittivity along c -axis
V_o : Amplitude of the input voltage	ϵ_0 : Permittivity of free space
t : microdisk thickness	A : Area of the ring resonator
$Q_{\text{RF},U}$: Unloaded RF quality factor of the ring resonator	L_T : Microstripline loss factor
Z_o : Microstripline impedance	$P_{\text{RF}}^{\text{in}}$: RF input power
β_c : Capacitance correction factor	S_{21o} : Measured S_{21} at resonance
ω_{RF} : RF frequency	S_{11o} : Measured S_{21} at resonance

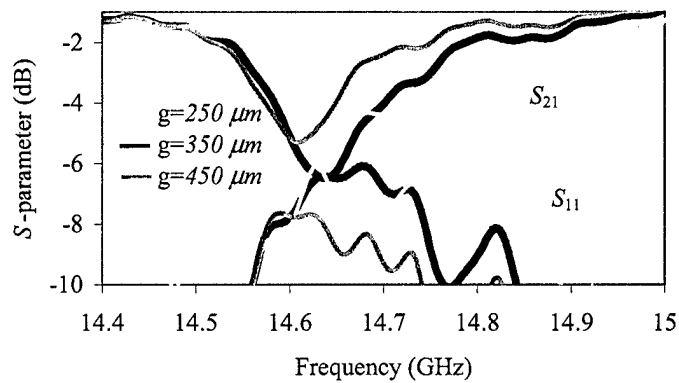
where P_{loss} is the loss factor given by:

$$P_{\text{loss}} = P_{\text{RF}}^{\text{in}} \left(1 - |S_{11o}|^2 - |S_{21o}|^2 - 1.5 \left(\frac{L_T - 1}{L_T} \right) \right)$$

$Q_{\text{RF},U}$, f_{RF} , S_{21o} and S_{11o} can be derived from measured S -parameter spectrum [14]. When $S_{11o} = S_{21o} = 50\%$ the ring is critically coupled to the microstripline and G_V is maximized.



(a)



(b)

Figure 8 (a) The optimized opto-mechanical design for tuning the RF coupling. (b) The S -parameter measurement results for a ring resonator ($w_r = 0.35$ mm) on a LiNbO_3 microdisk with an FSR of 14.6 GHz ($D = 3$ mm and $t = 0.4$ mm) at different values of the gap size (g). At $g = 350$ μm the critical coupling ($S_{11}^2 = S_{21}^2 = -6$ dB) and RF-optical frequency matching ($f_{\text{RF}} = \Delta\nu_{\text{FSR}} = 14.65$ GHz) are achieved simultaneously. Notice that the conventional definition of S -parameter is based on voltage ratios but the measured values on network analyzer are power ratios (measured in dB).

Fig. 8(a) is a photograph of the optimized opto-mechanical design that enables the accurate control of the RF coupling gap (g). Fig 8(b) shows The S -parameter measurement results for a ring resonator ($w_r = 0.35$ mm) on a LiNbO_3 microdisk with an FSR of 14.6 GHz (Fig. 7(b)). As may be seen the RF critical coupling ($S_{11o} = S_{21o}$) and RF-optical frequency matching ($f_{RF} = \Delta\nu_{FSR}$ 14.65 GHz) are achieved simultaneously. The estimated value of G_v for this ring resonator is between 5-5.5.

Fundamental single frequency modulation

The modulation efficiency and other characteristics of the microdisk modulator can be measured in a single frequency experiment at $f_{RF} = \Delta\nu_{FSR}$. We used our Ku-band modulator to demonstrate the sensitivity of RF-optical resonant modulator at 14.55 GHz. The microdisk modulator arrangement is shown in Fig. 9(a).

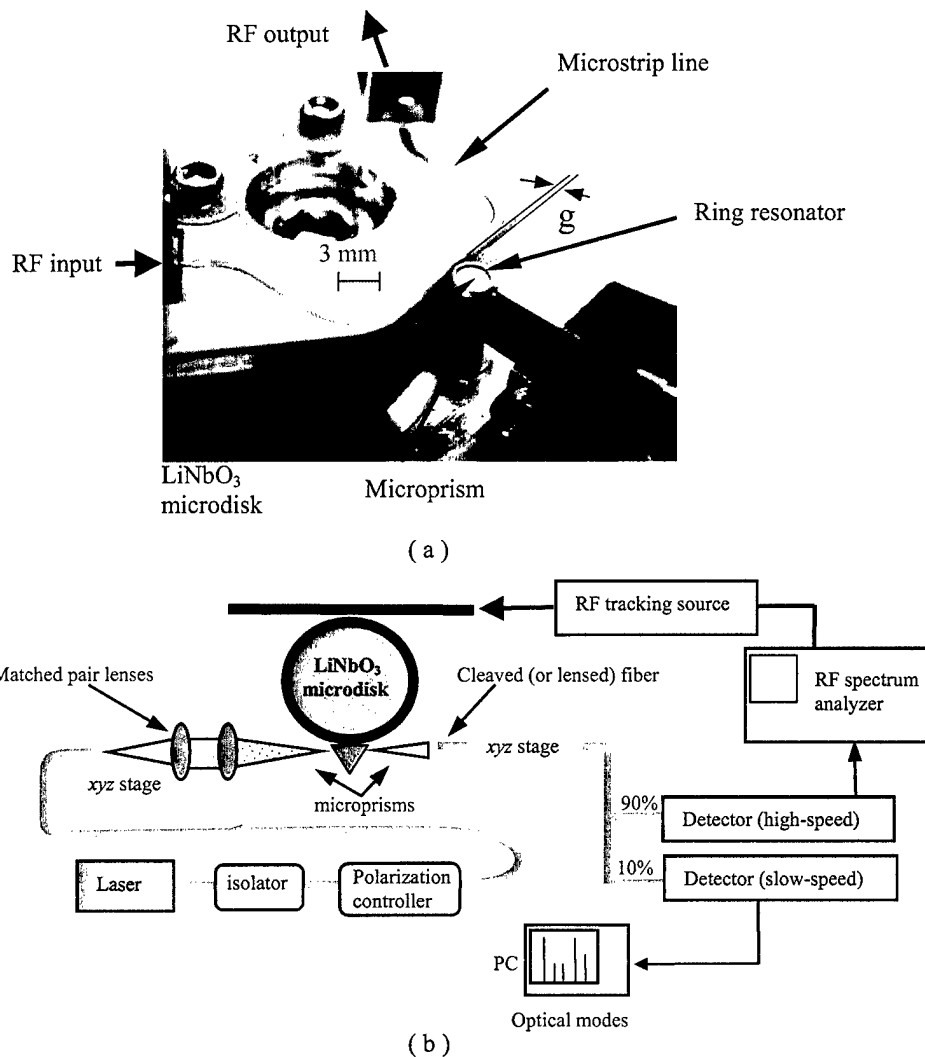


Figure 9 (a) Photograph of the Ku-band microdisk modulator. (b) Schematic diagram of the experimental arrangement used for evaluating the optical modulation performance of the microdisk modulator at single frequency.

The LiNbO₃ microdisk used in this arrangement is the same as Fig. 8(a) and 7(b) (400 μm thick, 3 mm in diameter with an optical free spectral range of 14.55 GHz). The copper ring resonator has an outer diameter of 3 mm and width of 300 μm . The RF energy stored in the ring at resonance ($f_{RF} = 14.55$ GHz) is maximized by tuning the gap size (g). Fig. 10(a) shows the variation of the modulated optical power against peak-to-peak voltage of the input signal. The inset shows the modulated optical mode with a Q of 4×10^6 . As may be seen at $V_{pp} = 0.56$ V the linear portion of the optical mode is completely modulated. Saturation of the linearly modulated optical power with increasing V_{pp} occurs because of increasing second-order harmonic generation due to nonlinear modulation.

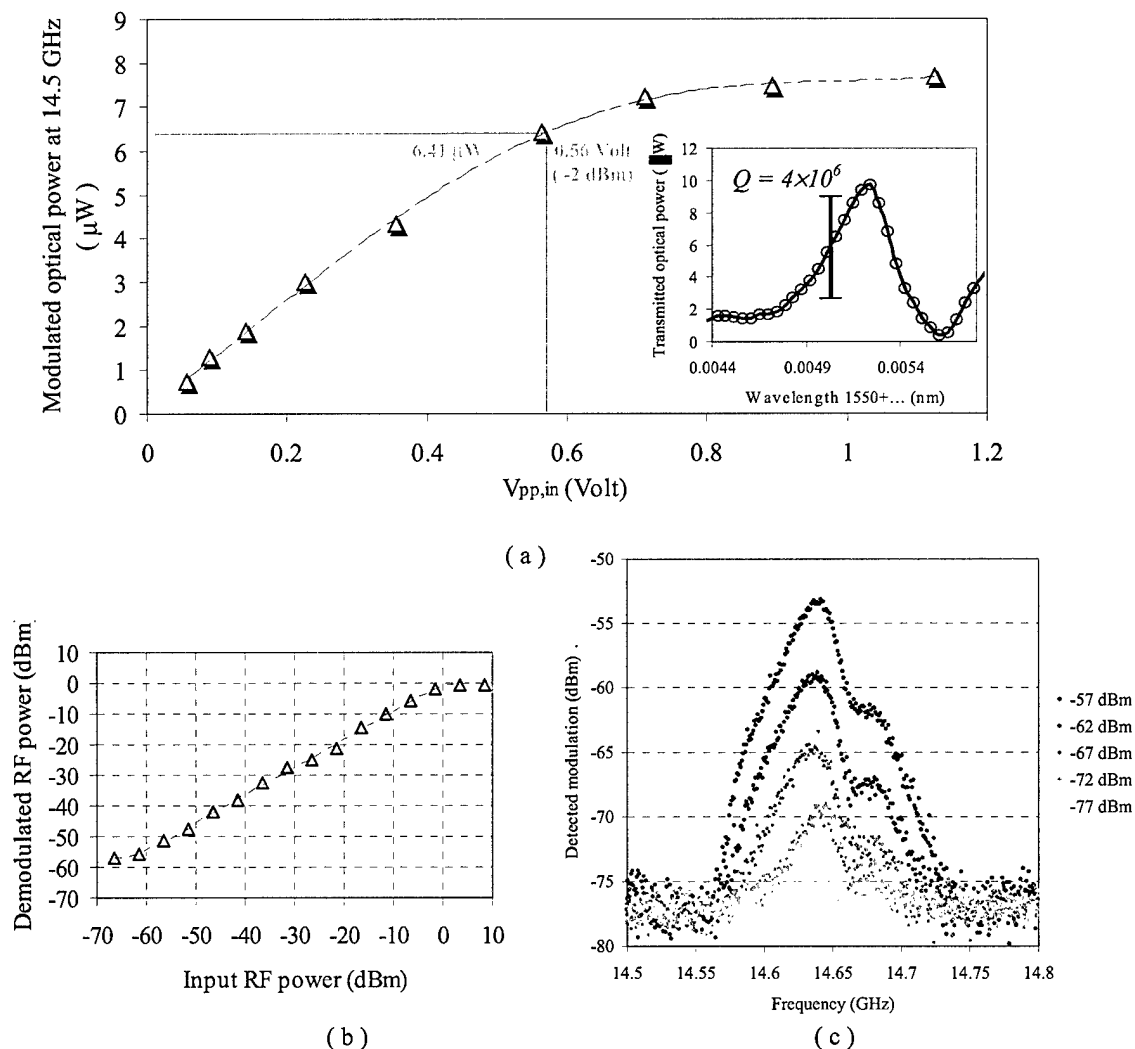


Fig. 10 (a) Linearly modulated optical intensity against peak-to-peak input voltage (and RF power). The inset shows the modulated optical mode. At $V_{pp} = 0.56$ V the optical power in the linear region of the optical mode is 100% modulated. (b) Demodulated RF power against input RF power. (c) Frequency spectrum of the detected RF power at very low RF input.

The optical intensity modulation is detected by a high-speed analog optical receiver with a responsivity of 260 $\mu\text{V}/\mu\text{W}$ at 15 GHz. The calculated effective interacting voltage (based on DC shift and detector responsivity) is 3 V at -1 dBm ($V_{pp} = 0.56$ V) RF input power that shows a voltage gain of 5.3 at resonance. The voltage gain calculated based on S -parameter measurements is 5.5. Fig. 10(b) shows the demodulated RF power against input RF power. The modulation saturation occurs around 0 dBm received RF power. Fig. 10(c) shows the frequency spectrum of the detected RF power at very low RF input powers. In this experiment an RF amplifier with a gain of 20 dB is used after the detector to amplify the weak detected RF power. At -67 dBm received RF power the signal-to-noise ratio of the detected RF power is about 13 dB. Both saturation voltage and sensitivity measurement results shown in Fig. 10(b) and (c) show 10 dB improvement compared to the best results reported previously for a 9 GHz LiNbO₃ microdisk modulator [6].

If the modulating RF frequency (f_{RF}) is very close to $\Delta\nu_{FSR}$, the behavior of the microdisk modulator may be explained using a simple model based on the optical transfer function of the microdisk optical resonator and electro-optic modulation of the WG k -vector. The time dependent extraordinary refractive index of the LiNbO₃ microdisk modulated by the voltage controlled by the ring resonator can be written as:

$$n'_e(t') = n_e + \delta n_e(t') = n_e + \frac{1}{2} n_e^3 r_{33} \frac{\beta_{EO} \beta_S}{t} \times G_V V_0 \cos(\omega_{RF} t')$$

where β_S (≈ 0.5) is a correction factor to compensate for the sinusoidal voltage distribution around the microdisk. Substituting n'_e in the optical transfer function one may estimate the modulated optical output power as a function of microdisk parameters. The modulated optical output power calculation may be simplified if we use the optical mode slope and the DC-shift as the main measurable parameters:

$$P_{o,mod} = G_V \beta_S V_0 S \Delta\lambda_{DC}$$

where $P_{o,mod}$ is the amplitude of the optical output power oscillation, and S is the optical mode slope in the vicinity of the laser wavelength (usually measured in $\mu\text{W}/\text{pm}$). In an additional single frequency experiment with the 14.55 GHz microdisk modulator we selected a symmetric and clean WG resonance to estimate the voltage gain (G_V). The maximum mode slope (S) was 80 $\mu\text{W}/\text{pm}$. The RF input power was -1 dBm corresponding to a V_0 of 0.56 V. After correcting the modulated voltage and input RF power to compensate for the RF cable losses we calculated a G_V of 5.12 using the measured values of S , V_0 and $\Delta\lambda_{dc}$.

Harmonic single frequency modulation

We have demonstrated efficient second-harmonic ($m_o = 2$) optical modulation by tuning the even second-harmonic resonance ($m_R = 2$) of the ring resonator to $2 \times \Delta\nu_{FSR}$. Fig. 11(a) shows a photograph of the experimental arrangement. The disk used is z -cut LiNbO₃ of radius $R = 2.9$ mm and thickness $t = 0.720$ mm. Optical coupling into and out of the microdisk is achieved using a single microp prism and the maximum coupled power is 100 μW . The optical Q is near 3×10^6 and $\Delta\nu_{FSR} \approx 7.6$ GHz (for TE WG modes). In this experiment first we compared the fundamental ($f_{RF} = \Delta\nu_{FSR}$) linear modulation efficiency of the ring and semi-ring resonator. Semi-ring resonator was previously used in the microdisk modulator design because its resonant frequency can be tuned simply by tuning the length [5,6,29-31].

Fig. 11(b) shows the measured S_{21} for the ring in Fig. 11(a) as well as a semi-ring on the same microdisk. The resonant dips up to the third harmonic of the ring are shown. For the ring resonator (solid line) we observe two dips (one small and one large) due to even-odd mode splitting. The coupling strength of the ring (depth of the resonant dips) at higher frequencies is better than that of the semi-ring and also the width of the resonant dips is smaller for the ring due to a better quality factor. These observations prove the superiority of the ring resonator especially at high frequencies. Fig.11(c) shows the measured S_{21} through the microstripline that is coupled to ring and semi-ring around the fundamental resonance. As may be seen the even mode of the ring and the fundamental resonance of the semi-ring are tuned to $\Delta\nu_{\text{FSR}}$. The left inset shows the simulated E -field distribution in the middle of the disk at fundamental even mode

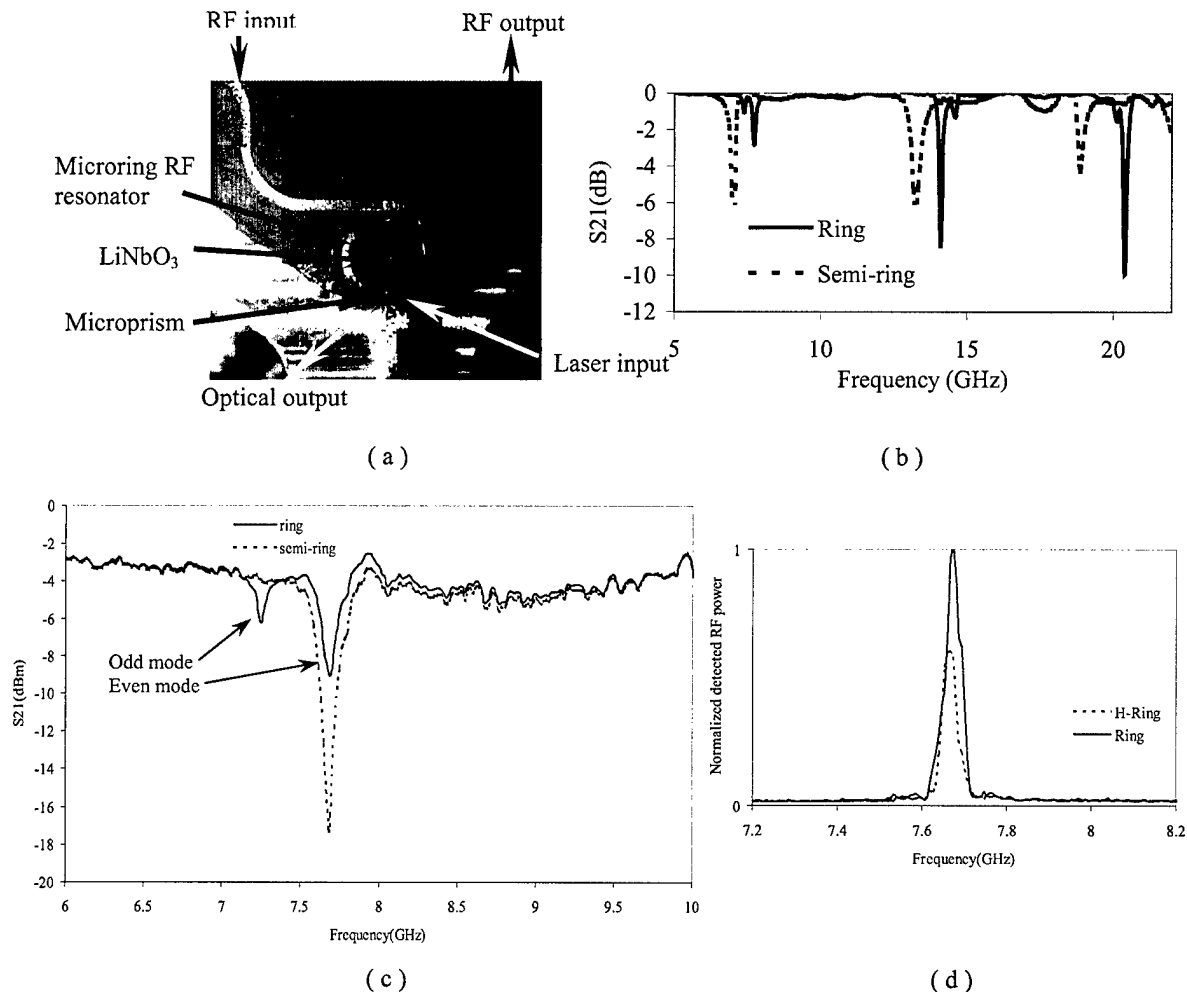


Figure 11 (a) Photograph of the experimental arrangement showing side-coupled microring, microprism, microdisk and output fiber. (b) S_{21} RF spectrum of a ring and semi-ring side-coupled to microstrip line. The copper microring has radius $R = 2.9$ mm and width $w = 0.5$ mm. (c) Measured S_{21} for semi-ring and ring at fundamental resonance. (d) The detected modulated power with semi-ring and ring resonator.

The right inset shows the detected RF power from the detector showing modulation improvement replacing semi-ring with ring. Fig. 12(a) shows a 3D view of the simulated E -field

distribution for even second-harmonic mode on the ring (Because of E -field distribution and better coupling, we use the even modes of the ring modulation). The plus sign means the E -vector is directed upward (along the c -axis) and minus sign means E -vector is pointing downward. Based on the E -vector directions it can be seen that the period of RF oscillation is half the photon round trip time ($f_{RF} = 2 \times \nu_{FSR}$) the optical field stays in phase with the RF -field. Fig. 12(b) is measured signal to noise ratio (SNR) at the fundamental ($\nu_{FSR} = 7.6$ GHz) and the second-harmonic ($2 \times \nu_{FSR} = 15.2$ GHz). To have a bit error ratio (BER) performance of better than 10^{-7} (analog SNR of 20 dB) the minimum RF power needed is -32 dBm at 15.2 GHz and -41 dBm at 7.6 GHz. At ($f_{RF} = \Delta\nu_{FSR}$).

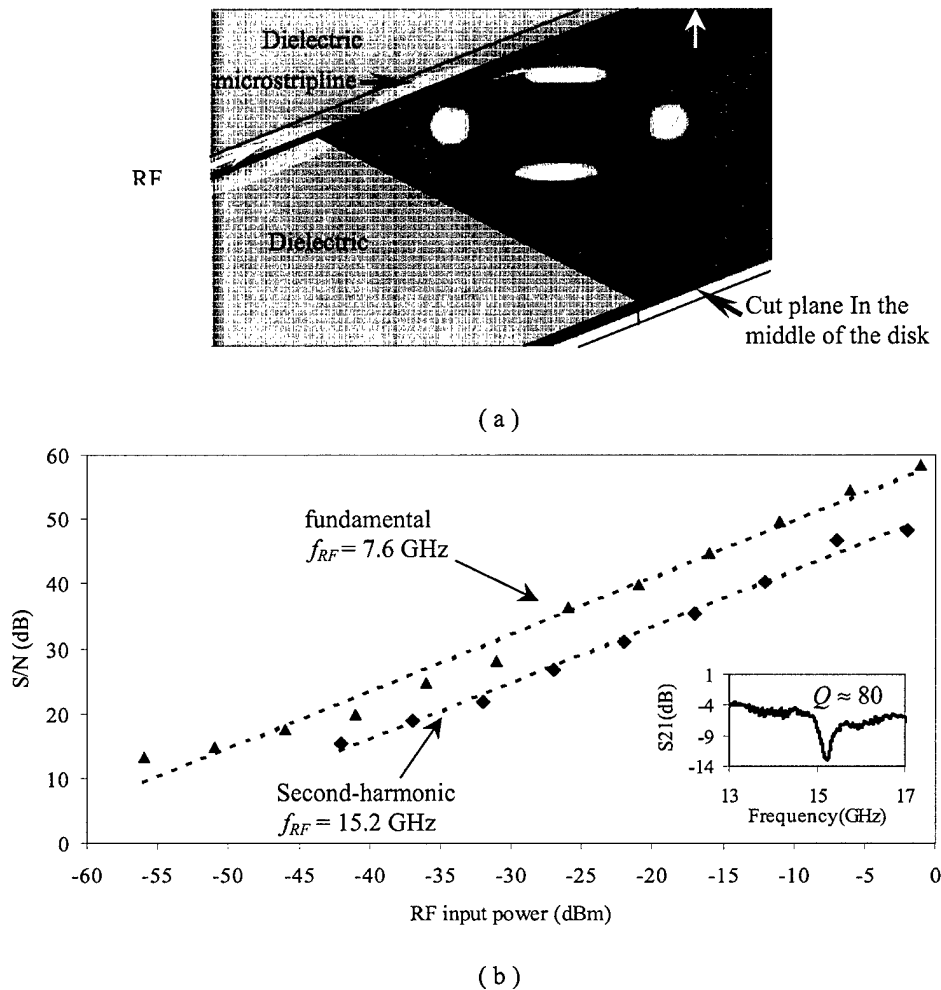


Figure 12 (a) 3D simulation of E -field distribution on a cut plane passing through middle of the disk when the even second-harmonic of the ring is excited. The plus signs correspond to E -vector directed upward along c -axis and minus signs correspond to downward direction. (b) Measured signal to noise ratio (of amplified signal) as a function of input RF power at fundamental ($f_{RF} = 7.6$ GHz) and second-harmonic ($f_{RF} = 15.2$ GHz) of the ring (the amplifiers have a gain of 30dB and noise figure of 1.7 dB and 2.6 dB respectively). The inset shows S_{21} spectrum when the even second harmonic of the ring ($f = 15.2$ GHz) is excited.

We have also demonstrated single frequency modulation at 26.1 GHz (using the 3rd harmonic of 5.13 mm disk) and 29.1 GHz (using the 2nd harmonic of 2.95 mm disk). Table 2 summarizes the fundamental and harmonic modulation frequencies that have been experimentally demonstrated.

Table 2

disk	D (mm)	t (mm)	Fundamental (GHz)	2 nd (GHz)	3 rd (GHz)
D1	2.93	0.4	15.2	-----	-----
D2	2.95	0.2	14.8	29.6	-----
D3	5.13	0.4	8.7	17.4	26.1
D4	5.8	0.72	7.6	15.2	-----
D54	3	0.4	14.6	-----	-----

Part II:

LiNbO₃ microdisk modulator in RF – optical link

We have demonstrated data and video transmission over a RF fiber-optic link using a traveling-wave LiNbO₃ microdisk resonator to modulate an optical carrier with a RF signal. Fig. 13(a) is a photograph of the side-coupled resonant modulator used in the experiments and Fig. 13(b) is a schematic diagram of the RF fiber-optic link.

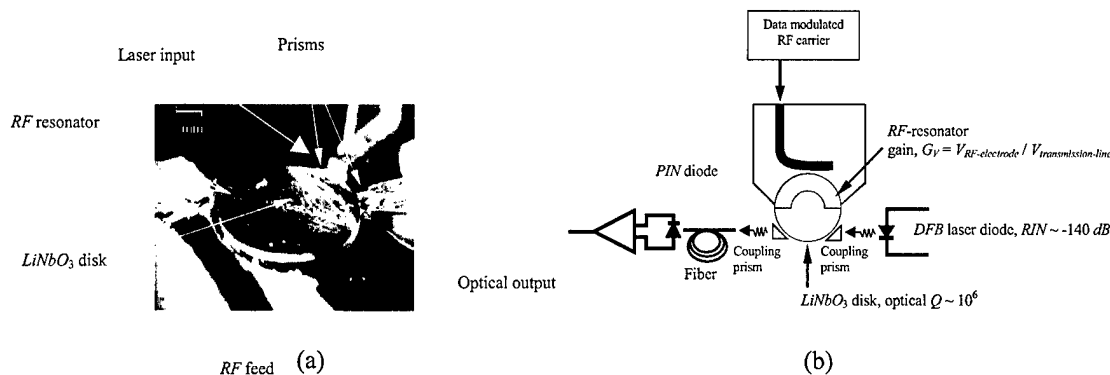


Figure 13 (a) Photograph of the side-coupled resonant traveling-wave LiNbO₃ microdisk used to modulate an optical carrier with a RF signal. (b) Schematic diagram of the RF fiber-optic link used in the experiments.

The disk employed is z-cut LiNbO₃ of radius $R = 2.56$ mm and thickness $t = 0.4$ mm. A micro-prism couples laser light into the microdisk and another prism is used to couple light out. All components are mounted on a planar structure to improve mechanical stability of the system. The RF-resonator is a semi-ring metal electrode side-coupled to a microstrip line. The fundamental resonant frequency of the RF-resonator is tuned to match the 8.68 GHz optical free-spectral-range (FSR) of the disk so that simultaneous RF and optical resonance maximizes the electro-optic interaction. A RF synthesizer generates the RF carrier (at the first resonant frequency of the half-ring) that is modulated by a non-return-to-zero pseudo-random bit-stream (NRZ 2⁷-1 PRBS) using a RF mixer. The resulting RF signal is then amplified and fed to the side-coupled ring resonator electrode used to modulate the 194 THz (wavelength $\lambda = 1550$ nm) optical carrier. After transmission through several meters of fiber, a PIN diode is used to detect and optical signal. The baseband data is down-converted through mixing with the local oscillator in a RF-mixer. The demodulated data is measured using a bit error ratio (BER) tester and a digital oscilloscope.

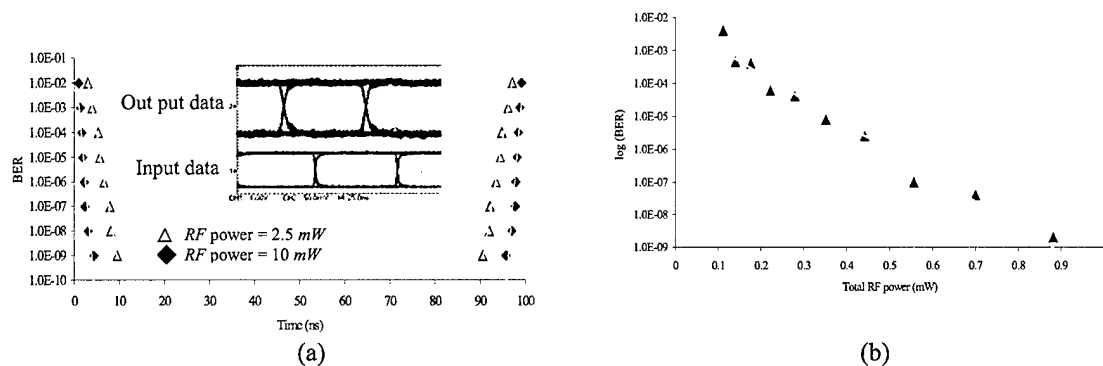


Figure 14 (a) Measured phase margin of the output at 10 Mb/s (NRZ 2⁷-1 PRBS) for 10 mW and 2.5 mW modulating RF power (the equivalent 50 ohm terminated peak-to-peak voltage (V_{pp}) is 2 and 1 Volt respectively). The inset is a representative of the corresponding output eye diagram. (b) Measured sensitivity of BER to modulating RF power (measured RF power within 150 MHz bandwidth centered at 8.68 GHz).

The laser wavelength is tuned close to the resonant wavelength of one of the high- Q TE-modes of the disk where optical modulation is maximized. The bandwidth of the chosen optical-mode is about 150 MHz, corresponding to an optical $Q = 1.3 \times 10^6$, and this limits the data transmission rate to less than 200 Mb/s. The modulating RF power is the measured power of the RF signal (data modulated RF carrier) within 150 MHz bandwidth centered at 8.68 GHz RF-carrier frequency. Fig. 14(a) shows the measured phase margin of the output at 10 Mb/s (NRZ 2⁷-1 PRBS) for two different modulating RF-powers, 10 mW and 2.5 mW (2 and 1 Volt equivalent 50 ohm terminated peak-to-peak voltage). The inset is a representative of the corresponding output eye-diagram. Fig. 14(b) shows the measured sensitivity of BER to modulating RF power. The optical output power for all of these measurements is between 18 μ W to 27 μ W and the laser wavelength is tuned close to the middle of the optical mode slope. Fig. 15 shows input and demodulated output eye-diagrams transmitted over the RF fiber-optic link at (a) 50 Mb/s and (b) 100 Mb/s NRZ 2⁷-1 PRBS data rates.

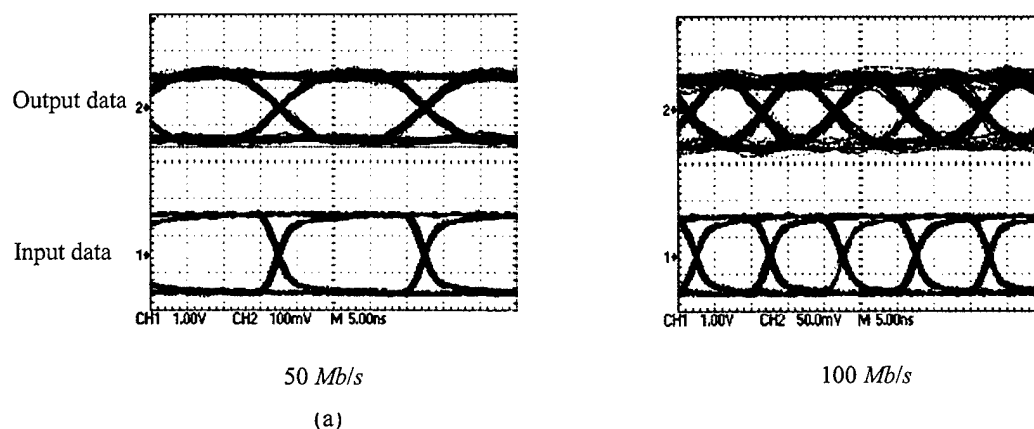


Figure 15 Input and demodulated output eye-diagrams transmitted over the RF fiber-optic link at (a) 50 Mb/s and (b) 100 Mb/s NRZ 2⁷-1 PRBS data rates. The modulating RF power is 40 mW and 60 mW respectively.

The critical factors for high-quality data transmission are the purity and Q -factor of the chosen optical mode, the magnitude of the rising or falling slope of the optical mode in the vicinity of the laser wavelength, and the optical output power from the disk. By tuning the laser wavelength and RF carrier frequency it is possible to optimize the modulation quality and efficiency. Because of the high- Q of the optical modes ($1 - 3 \times 10^6$), the sensitivity of modulation quality and efficiency to the mode's slope, wavelength stability of the laser is also important. A stable, high-quality, data transmission requires a wavelength stability of less than 0.1 pm.

To gain insight into the variables which most influence signal-to-noise and hence ultimate performance of the microdisk modulator for RF wireless applications we have investigated the sensitivity and BER performance of the modulator using realistic values of critical parameters. Contributions to signal-to-noise come from many sources these include laser relative intensity noise (RIN) laser line-width, optical detector dark current, detector amplifier noise, antenna background noise, etc. We found that laser RIN , microdisk optical Q , and RF electrode gain factor G_v are the important parameters determining sensitivity. Optical disk thickness, t , is also an important factor because, in the geometry we use, RF electric field intensity is proportional to t . Fig. 16(a) illustrates the sensitivity of the receiver to variation in optical Q . Increasing optical Q by a factor of two from 2×10^6 to 4×10^6 changes sensitivity by a factor of eight from 4.5 nW to 0.55 nW while decreasing the data bandwidth from 100 MHz to 50 MHz. Fig. 16(b) illustrates the sensitivity of the receiver to variation in microdisk thickness t . Decreasing t by a factor of two from 200 μm to 100 μm changes sensitivity by a factor of four from 2.5 nW to 0.66 nW. The improved value of sensitivity dramatically decreases BER so that values of BER in the 10^{-9} range can be achieved with RF input powers of less than 100 nW.

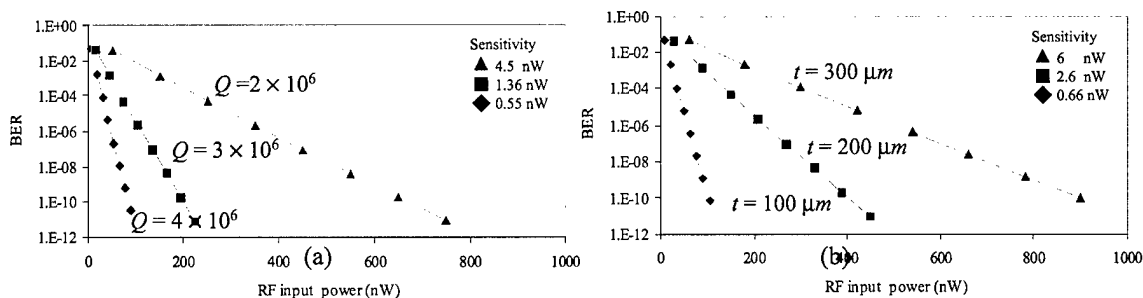


Figure 16 (a) Calculated sensitivity and BER as a function of RF input power assuming the indicated value of optical Q , optical coupling efficiency 15%, laser RIN of -150 dB/Hz, disk thickness $t = 400 \mu\text{m}$, and RF Electrode voltage gain, $G_v = 2$. (b) Calculated sensitivity of BER as a function of RF input power assuming the indicated values of disk thickness t , an optical coupling efficiency of 15%, an optical Q -factor, $Q = 1.5 \times 10^6$, laser RIN of -150 dB/Hz, and RF electrode voltage gain, $G_v = 2$.

To achieve 10^{-9} BER with a few nW of received RF power requires simultaneous optimization of a few parameters. Fig. 17 shows the result of calculating sensitivity and BER as a function of RF input power assuming the indicated value of laser RIN and optical coupling efficiency. The device has thickness $t = 400 \mu\text{m}$, Q -factor is 2×10^6 , RF electrode voltage gain $G_v = 10$. Notice, for the parameters simulated, optical coupling efficiency has little influence on BER with essentially the same results being obtained for 15% and 80% coupling efficiency for both curves. However, dramatically improved results occur when RIN is reduced from -140 dB/Hz to -150

dB/Hz. In the latter case, sensitivity is 50 pW and BER of 10^{-9} may be achieved at an RF input power of approximately 7 nW. These results are very encouraging and provide a systematic approach with which to optimize the microphotonic modulator in the RF receiver.

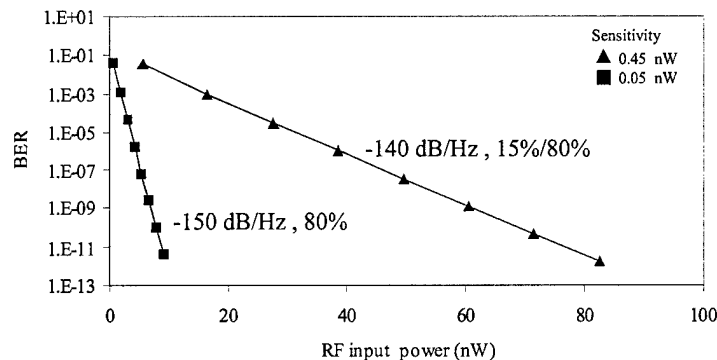
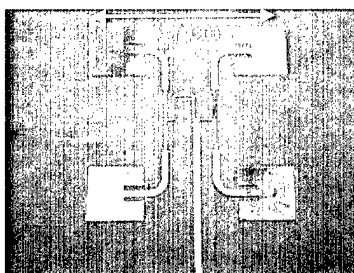


Figure 17 - Calculated sensitivity and BER as a function of RF input power assuming the indicated value of laser RIN and optical coupling efficiency. Disk thickness $t = 400 \mu\text{m}$, Q -factor is 2×10^6 , RF electrode voltage gain $G_V = 10$.

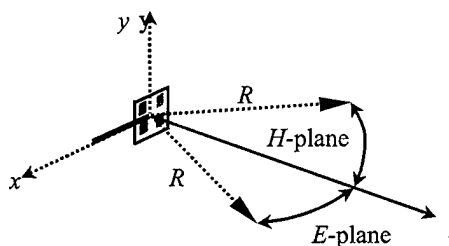
Patch antenna and patch antenna arrays

Antennas for operation at 8 GHz, 15 GHz and 30 GHz RF carrier frequency have been designed, fabricated to enable the demonstration of microdisk modulator performance in a wireless RF-optic link. We started working on planar antenna structures by design and fabrication of the single patch antenna at 8 GHz, 15 GHz and 30 GHz. In order to increase the radiated and detected power as well as improving the directionality of the radiation we switched to antenna patch arrays. Four-patch antenna array has been successfully designed and tested at 8 GHz and 14.5 GHz for application in two different microdisk optical receivers with 5.13 mm and 3 mm diameter disks respectively.

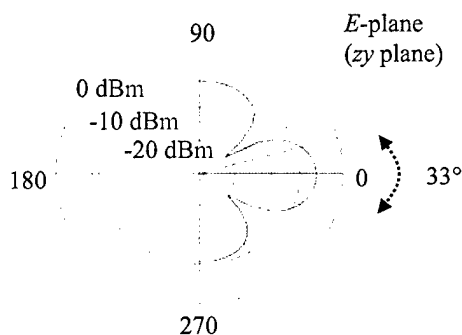
Fig. 18(a) shows the photograph of the fabricated four-patch antenna array at 8 GHz. The antenna has been fabricated on 0.5 mm thick duroid board with a permittivity of 2.94 and loss tangent of 0.00119. Fig. 18(b) shows the simulated radiation pattern of the antenna. As we see the radiation is effectively concentrated inside a 33° cone (3 dB angular width) in both H and E plane. Fig. 18(c) shows the experimental results of measuring the radiation patterns that are in good agreement with calculated results. The transmitting and receiving antennas were identical. The same design has been scaled to 14.5 GHz and four-patch antenna array has been fabricated and successfully tested at 14.5 GHz. To increase the radiation power and make the radiation more directive we switched to a series-fed ten-patch antenna array. Fig. 19(a) shows a photograph of the fabricated ten-patch series fed antenna array (on the same dielectric material). Fig. 19(b) shows the experimental results of measuring the radiation pattern as we see the vertical 3dB angular width (E-plane) decreased to 14° .



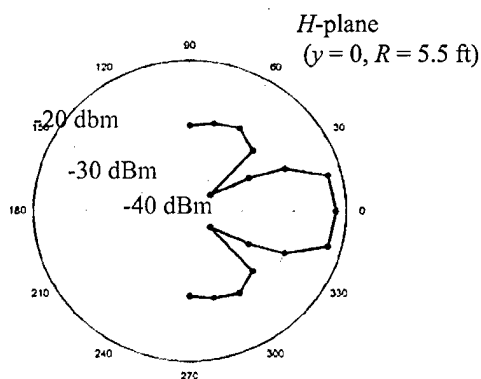
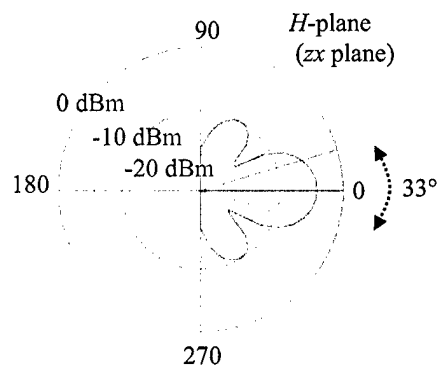
(a)



(b)



(c)



(d)

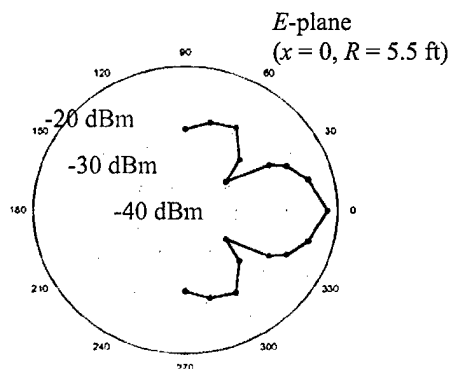


Figure 18 (a) Photograph of the fabricated 8.7 GHz four-patch antenna array and definition. (b) Definition of coordinates for characterizing the radiation pattern. (c) Calculated radiation pattern for antenna. (d) Experimental results of measuring the radiation pattern at 8.7 GHz.

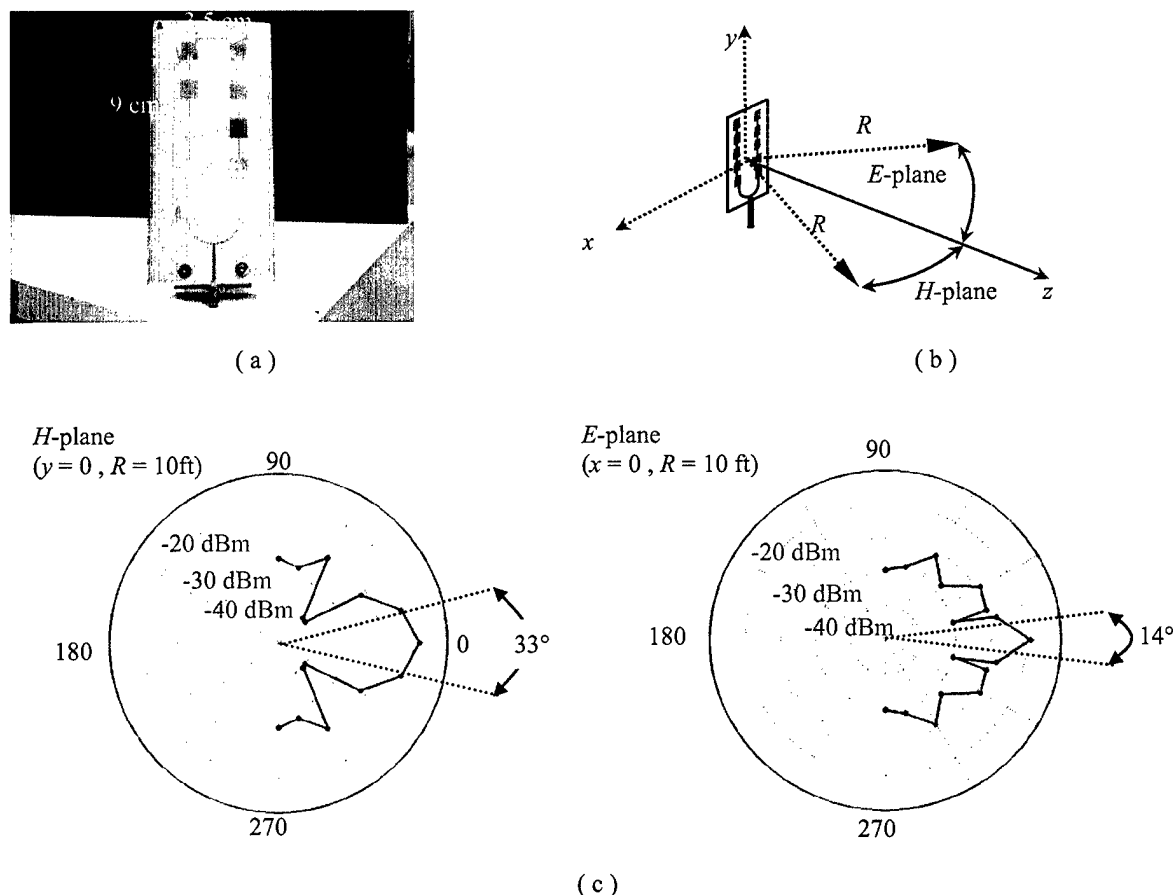


Figure 19 (a) Photograph of the fabricated 8.7 GHz series-fed ten-patch antenna array. (b) Definition of the coordinates for characterizing the radiation pattern. (c) Experimental results of measuring the radiation pattern at 8.7 GHz.

LiNbO₃ microdisk modulator in wireless RF – optical link

We have used the 4 and 10 patch antenna arrays designed for 8.7 GHz to demonstrate the performance of the microdisk modulator in a wireless RF-optical link. The antenna was directly attached to the microdisk modulator shown in Fig. 13. The transmitting antenna was a similar patch array fed by amplified data or video modulated 8.7 GHz carrier. We have successfully transmitted up to 100 Mb/s data stream and video signal over a 10 ft link. The operational distance of the link can be improved by employing more efficient antennas and more sensitive microdisk modulator.

Part III:

RF mixing/Down-conversion in optical domain

Processing microwave and mm-wave signals in the optical domain has been the subject of intensive research for the past few years [16-18]. Placing a RF signal on an optical carrier enables a wide variety of photonic signal processing techniques and, at the same time, avoids the use of lossy transmission lines and high-speed electronic devices. One of the key operations in microwave communication is frequency mixing. Several techniques have been proposed for RF mixing in the optical domain such as nonlinear modulation in a Mach-Zehnder modulator [19]

and nonlinear detection in a photodiode [20]. Here we introduce a new photonic RF mixing technique that exploits simultaneous RF and optical resonance in the microdisk modulator. This is used to realize a photonic RF receiver without any high-speed electronic components.

In a conventional super-heterodyne RF receiver architecture a local oscillator (LO) and mixer are used to down-convert the signal to IF frequencies. Baseband information is subsequently extracted from the IF signal in a detector/demodulator. Alternatively, in a direct-conversion (homodyne) radio receiver, baseband information is obtained by mixing the received signal and the LO without using an IF frequency [21]. In addition to such approaches, self-heterodyne techniques have been proposed to reduce the number of components as well as size, weight, and power consumption in high-carrier frequency (mm-wave), short distance, applications [22]. In a self-heterodyne transmission system the transmitter broadcasts a RF modulated signal *and* the local carrier so the IF signal can be down-converted by mixing the received carrier and modulated signal in a nonlinear device called a self-mixer. The receiver power consumption, phase noise, and complexity are reduced as a result of eliminating the conventional LO and mixer. Although such an approach suffers from reduced power efficiency, it has been shown that it can lower overall cost and complexity in mm-wave local area networks and indoor wireless transmission systems.

Our photonic self-homodyne architecture combines direct-conversion, self-heterodyning, and microdisk modulator technology, to directly extract baseband information from the received signal by self-mixing of the transmitted carrier and the sidebands in the optical domain. We show that the second-order nonlinearity in the transfer function of a LiNbO₃ microdisk optical modulator when biased at its minimum transmission point may be used to realize the self-mixing process.

Microphotonic self-homodyne RF receiver

A photonic self-homodyne RF-receiver replaces the function of a single-ended diode or FET mixer in a transmitted carrier wireless link with a sensitive optical modulator that performs down-conversion in the optical domain. In this approach the nonlinear dependence of the modulator's transmitted optical power (P_{ot}) on applied RF voltage (V_{RF}) is the source of nonlinearity in the system. Fig. 20 illustrates the photonic self-homodyne RF receiver architecture. The received RF signal contains both sidebands and the center frequency (transmitted-carrier double-sideband modulation format) and is fed to an optical modulator biased at its nonlinear operating point. The carrier and sidebands are mixed through the second-order nonlinearity ($P_{ot} \propto V_{RF}^2$), hence the optical output intensity spectrum contains the baseband and high-frequency products around the second-harmonic of the carrier frequency. A photoreceiver with a bandwidth matched to the baseband signal generates the baseband photocurrent (i_p) and automatically filters out the high-frequency components. The bandwidth of all electronic circuitry used in the system is no greater than that of the baseband signal.

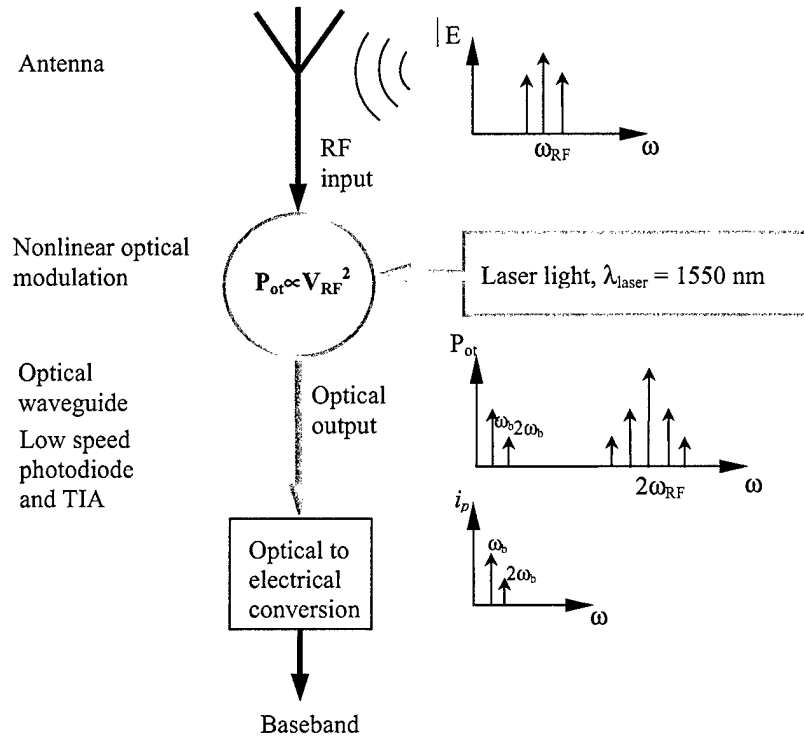


Figure 20 Schematic diagram of the photonic self-homodyne RF receiver. The transmitted carrier RF signal is received by the antenna and is directly fed to a square-law optical intensity modulator. Through nonlinear optical modulation the optical output intensity spectrum contains the baseband and high frequency components that are filtered out by the response of the low-speed photodetector.

The electro-optic transfer function of an optical intensity modulator $P_{ot}(V_{RF})$ can be expanded around $V_{RF} = 0$ to give

$$P_{ot} = P_o^{(0)} + P_o^{(1)} + P_o^{(2)} + \dots = N_0 + N_1 V_{RF} + \frac{N_2}{2} V_{RF}^2 + \dots$$

Here, N_i ($i > 0$) is the i th Taylor expansion coefficient of $P_{ot}(V_{RF})$ at $V_{RF} = 0$ and N_0 is the transmitted optical power at $V_{RF} = 0$. At a fixed wavelength the magnitude of N_i depends on modulator properties and the chosen bias point. The first-order term linear optical intensity modulation ($P_{ot} \propto V_{RF}$) while other terms contribute nonlinear frequency components. Usually, such nonlinearities are minimized in conventional direct detection (DD) optical communication links. If the RF voltage amplitude is small enough and the modulator is biased at its extreme transmission point (where $dP_{ot}/dV_{RF} = 0$) the second-order term $P_o^{(2)}$ dominates the behavior of the modulator and the transmitted optical power (P_{ot}) dependence on voltage around $V_{RF} = 0$ will be similar to an ideal square-law mixer with:

$$P_{ot} \approx N_0 + \frac{N_2}{2} V_{RF}^2$$

If the baseband is a pure sinusoidal signal, the received RF voltage can be written as:

$$V_{RF} = V_0 (1 + m_I \cos(\omega_b t)) \cos(\omega_{RF} t)$$

where m_I is the RF modulation index, ω_b is the baseband frequency and $\omega_{RF} = 2\pi f_{RF}$ is the RF carrier frequency. The second-order term can be written as:

$$P_o^{(2)} = \frac{N_2}{2} \times V_{RF}^2 = \frac{N_2}{2} V_0^2 (1 + m_I \cos(\omega_b t))^2 \cos^2(\omega_{RF} t)$$

Expanding the right-hand-side of this equation one obtains a DC term equal, high frequency components centered around $2\omega_{RF}$ and the two down-converted low-frequency terms at ω_b and $2\omega_b$ are given by

$$\frac{N_2 V_0^2 m^2}{8} \cos(2\omega_b t) + \frac{N_2 V_0^2}{2} m_I \cos(\omega_b t)$$

The total second-order modulated optical power is

$$P_{o,max}^{(2)} = (1 + m_I^2 + 2m_I) \frac{N_2}{2} V_0^2$$

If we use a slow speed photodetector with a responsivity R , The optical power modulated at ω_b generates the baseband photocurrent i_b that carries the received information:

$$i_b = R \frac{N_2 V_0^2}{2} m_I \cos(\omega_b t)$$

The efficiency of this down-conversion process may be defined as the ratio between the amplitude of the optical power modulated at ω_b and $P_{o,max}^{(2)}$. This efficiency is limited by the generation of undesired frequency components at $2\omega_b$, $2\omega_{RF} \pm 2\omega_b$, and $2\omega_{RF} \pm \omega_b$ as well as the DC component. The linearity of the down-conversion is also an important parameter in receiver operation and is defined as the ratio of optical power modulated at ω_b and $2\omega_b$. Here we assume that the strength of the second-order nonlinearity dominates higher order terms in Equation (1) so the generation of higher harmonics of the baseband ($3\omega_b$, $4\omega_b$, etc.) can be ignored. The down-conversion efficiency and its linearity are determined by the RF modulation index (m_I).

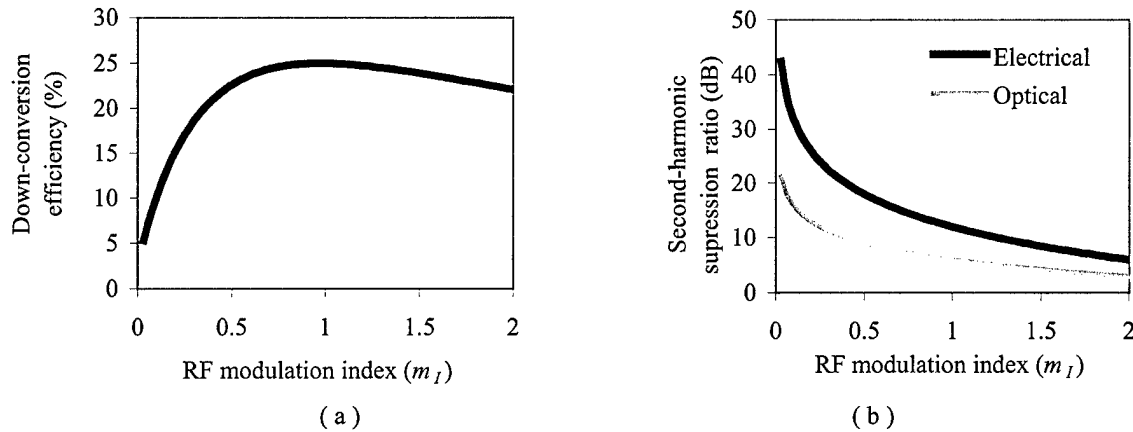


Figure 21 (a) Calculated down-conversion efficiency ($P_{o,\omega_b}/P_{o,max}^{(2)}$) versus RF modulation index (m_I). (b) Second-harmonic suppression ratio against m_I . The electrical (after detection) and optical suppression ratios are related through $P_{e,\omega_b}/P_{e,2\omega_b} = (i_{\omega_b}/i_{2\omega_b})^2 \propto (P_{o,\omega_b}/P_{o,2\omega_b})^2$

In Fig. 21 the down-conversion efficiency (a) and second-harmonic suppression ratio (b) are calculated against m_I . The second-harmonic baseband term ($2\omega_b$) can be suppressed relative to the baseband (ω_b) by employing a transmitted carrier RF modulation format ($m_I < 2$) and the down-conversion efficiency reaches its maximum value of 25% around $m_I = 1$. By choosing $m_I = 0.8$ an efficiency of about 25% and second-harmonic suppression of 7 dB optical (14 dB

electrical, $P_e \propto i_p^2 \propto P_{ot}^{(2)}$) can be achieved. The sensitivity of a photonic RF receiver strongly depends on the magnitude of the second-order nonlinearity (N_2) and so is determined by the modulator sensitivity and the transfer function P_{ot} . Given that most wireless links only require a limited bandwidth around a high frequency carrier, a microdisk resonant optical modulator [??] is a suitable choice for this application.

LiNbO₃ microdisk photonic RF mixer

At given RF voltage depending on the laser input wavelength the electro-optic transfer function of the microdisk modulator can have a linear or nonlinear functionality. Fig. 22 shows how the value of the laser wavelength relative to the resonant wavelength can change the linearity of the optical modulation in a microdisk modulator. Two cases has been simulated (a) the laser wavelength is tuned to the middle of the mode slope where $P_{o,mod} \propto V_{RF}$ (b) the laser wavelength is tuned to a resonant wavelength where $P_{o,m} \propto (V_{RF})^2$.

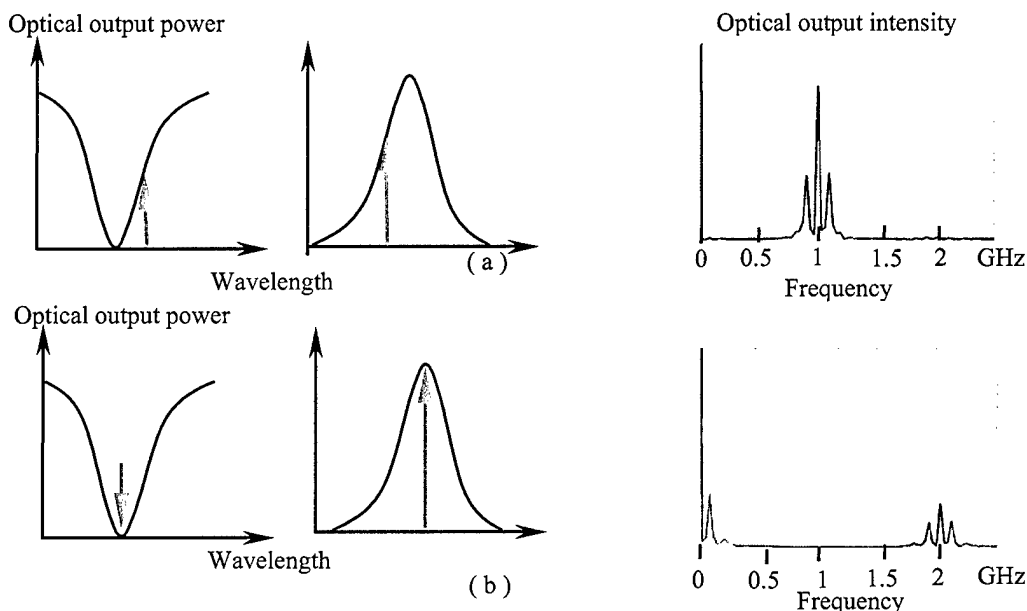


Figure 22 Simulated optical output power spectrum of microdisk modulator at linear (a) and nonlinear (b) operation regime. The RF input power is a 1 GHz RF carrier modulated by a 100 MHz (single frequency) baseband signal

The RF input voltage has the form $V_{RF} = V_o(1+m_I \cos(\omega_b t)) \cos(\omega_{RF} t)$. The simulation clearly shows that when $\lambda_{laser} = \lambda_{res}$ the spectrum of the optical output power is similar to what is shown in Fig. 19. Fig. 23 illustrates the measured spectrum of the detected RF power when the microdisk modulator is fed by a single frequency RF signal ($V_{RF} = V_o \cos(2\pi f_{RF} t)$) $f_{RF} = \Delta \nu_{FSR} = 8.7$ GHz). As may be seen when the laser wavelength is tuned to the resonant wavelength the linear modulated optical power (at 8.7 GHz) is suppressed and its second-harmonic (at 17.4 GHz) increases as a result of second-order nonlinear modulation or $P_{o,m} \propto (V_{RF})^2$.

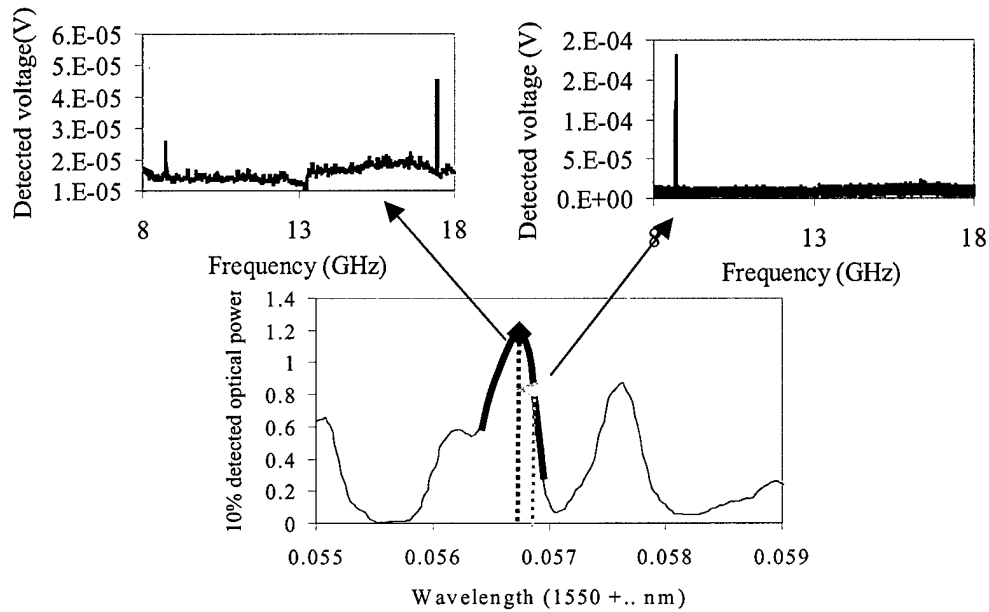


Figure 22 Nonlinear modulation with microdisk modulator. The microdisk is fed by a 0 dBm single frequency RF signal ($f_{RF} = 8.7$ GHz is the optical free spectral range of the disk). When the laser wavelength is set to the middle of the optical mode slope the modulation is linear so we observe modulation only at 8.7 GHz (right) when the wavelength is at the peak, modulation becomes nonlinear and modulation occurs at 17.4 GHz while the linear component becomes small (left).

In the previous section we estimated the amplitude of the down-converted baseband modulated optical power for a general second-order nonlinear modulator. We showed that the baseband power is proportional to the second-order derivative of the electro-optic transfer function at a certain biased point (N_2). In Fig. 24 the transmitted optical power (P_{ot}) for a typical microdisk modulator is simulated as a function of input RF voltage (V_{RF}). In our simulation the modulator parameters are chosen to be representative of the experimental values with $Q = 3.5 \times 10^6$ (corresponding to $\alpha = 0.0075 \text{ cm}^{-1}$ and $\kappa_0 = 0.095$), $h = 400 \text{ }\mu\text{m}$, and $G_v = 6$. The optical input power is $50 \text{ }\mu\text{W}$ and $\lambda_{\text{laser}} \sim 1550 \text{ nm}$. The laser wavelength is tuned to an optical resonance of the microdisk ($\lambda_{\text{res}} = \lambda_{\text{laser}}$) so in the absence of an external voltage ($V_{RF} = 0$) the transmitted optical power is minimized. At this bias point N_1 is zero and N_2 is maximized so the modulator is operating in the extreme nonlinear regime. The sensitivity of the modulator can be quantified by a voltage amplitude V_{HMM} that modulates half of the optical mode power ($P_{o,mod} = P_{o,in} - P_{o,min}$). V_{HMM} is determined by the optical Q , t , r_{33} , and G_v . If $V_{RF} < 0.1V_{HMM}$ (small signal operating regime) the microdisk modulator is effectively operating as a square law optical intensity modulator ($N_i \sim 0$, $i > 2$) as explained in the previous section. Since the baseband modulated optical power is equal to $m_l N_2 V_{02}/2$. N_2 is the critical parameter for down-conversion and is directly proportional to V_{HMM} and optical input power. Fig. 23 shows that $V_{HMM} = 0.48 \text{ V}$ and optical input power of $50 \text{ }\mu\text{W}$ results in $N_2 = 0.037 \text{ mW/V}^2$.

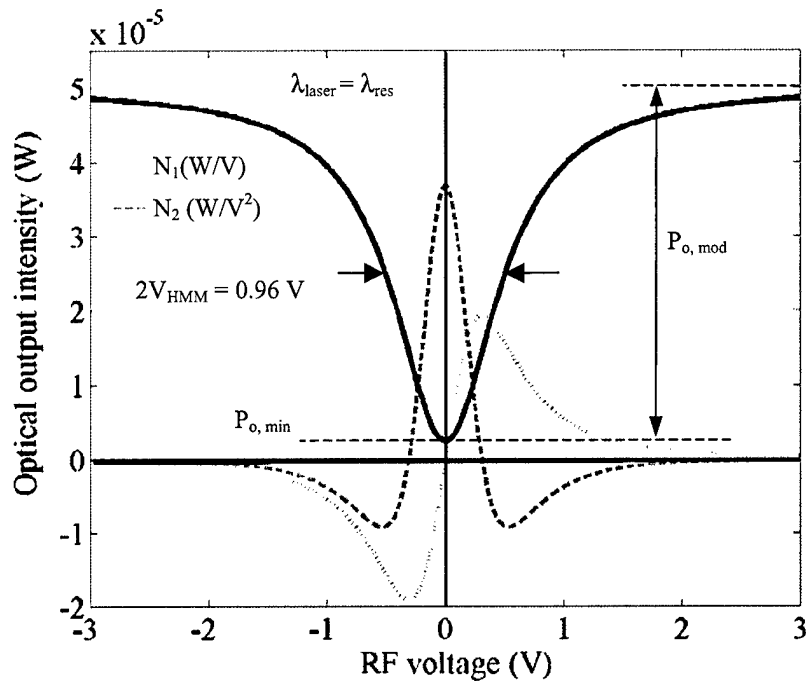


Figure 24 Calculated optical output intensity of an ideal microdisk modulator as function of RF input voltage ($Gv = 6$). The dashed and the dotted lines are generated as the first (N_1) and second (N_2) Taylor coefficients in an expansion of the optical transfer function (solid line). The laser is biased to the extreme nonlinear operating regime $\lambda_{\text{laser}} = \lambda_{\text{res}}$.

LiNbO₃ microdisk self-homodyne RF receiver

In our initial experiments we use a single tone baseband signal to study the effect of RF modulation index (m_I) and RF power on down-conversion efficiency and its linearity. Fig. 25(a) and (b) are the photographs of the 14.6 GHz microdisk modulator. Fig. 25(c) is a schematic diagram of the experimental arrangement. The modulator uses a 400 μm thick LiNbO₃ microdisk of 3 mm diameter and a free spectral range of $\Delta\nu_{\text{FSR}} = 14.6$ GHz. The laser source is a tunable single mode laser with 0.05 pm wavelength resolution and a linewidth of less than 0.5 MHz. The laser wavelength is always tuned to the minimum of the chosen transmission dip to maximize the second-order nonlinear modulation strength (N_2). The RF signal is a 10 MHz single tone baseband signal mixed with a 14.6 GHz RF-carrier in a double-balanced RF-mixer. By DC-biasing the IF port of the mixer we can control the modulation index (m_I) and magnitude of the transmitted power at the carrier frequency. The RF signal is fed to the microdisk modulator through a bandpass RF filter with 1 GHz bandwidth around 14.5 GHz, to make sure that all of the nonlinear products generated in the RF components are filtered out. The optical output is detected in an amplified photodetector with a bandwidth of 150 MHz and responsivity of 3 mV/ μW .

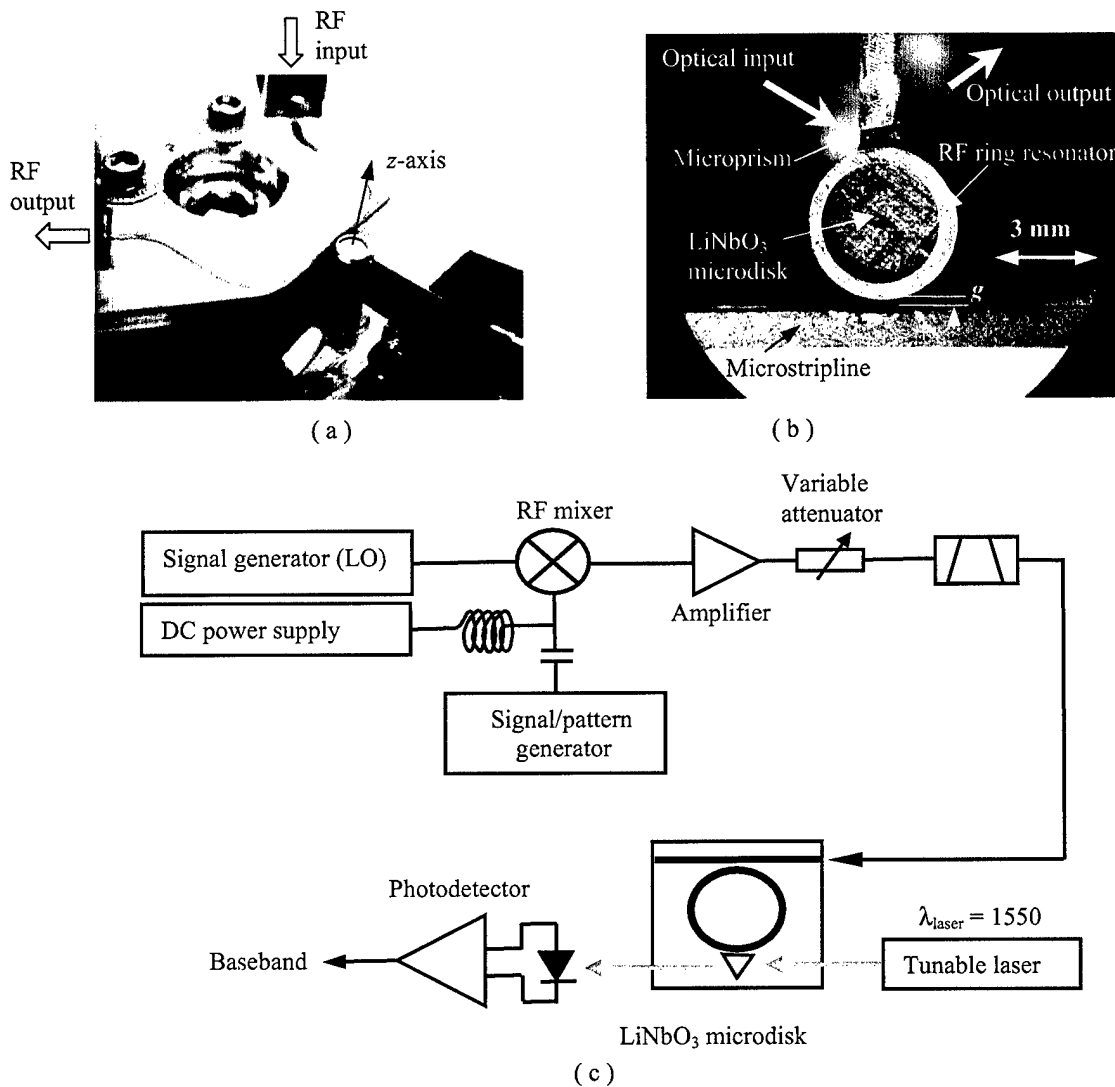


Figure 25 (a) Photograph of the LiNbO₃ microdisk modulator. (b) A close up view of the modulator showing the microstripline, LiNbO₃ microdisk, microprism, microring RF resonator and the output fiber. (c) Schematic diagram of the experimental arrangement used for photonic RF down-conversion measurements. The RF modulation index (m) is tuned using the DC bias on the mixer. The laser is a tunable single mode laser with a resolution of 0.1 pm and linewidth of less than 0.5 MHz. The RF filter eliminates any low frequency component generated due to nonlinearities in RF devices. The local oscillator frequency is 14.6 GHz that is equal to the optical free spectral range of the microdisk modulator.

Fig. 26 shows the down-converted optical power against the total RF input power when $m = 0.8$. The black circles are the experimental data and the white circles and dashed line are the simulated data. The inset shows the optical resonance selected for nonlinear modulation. The black arrow indicates the location of the laser wavelength, λ_{laser} . The optical resonance has $Q = 2.7 \times 10^6$ and a N_2 coefficient of 0.023 mW/V^2 ($V_{\text{HMM}} = 0.7 \text{ V}$). The simulated data in Fig. 20 are calculated using $mN_2V_0^2/2$ and knowing that the total average RF power of a single tone modulated RF carrier is given by $P_{\text{RF}} = V_0^2(1+m^2/2)/100$.

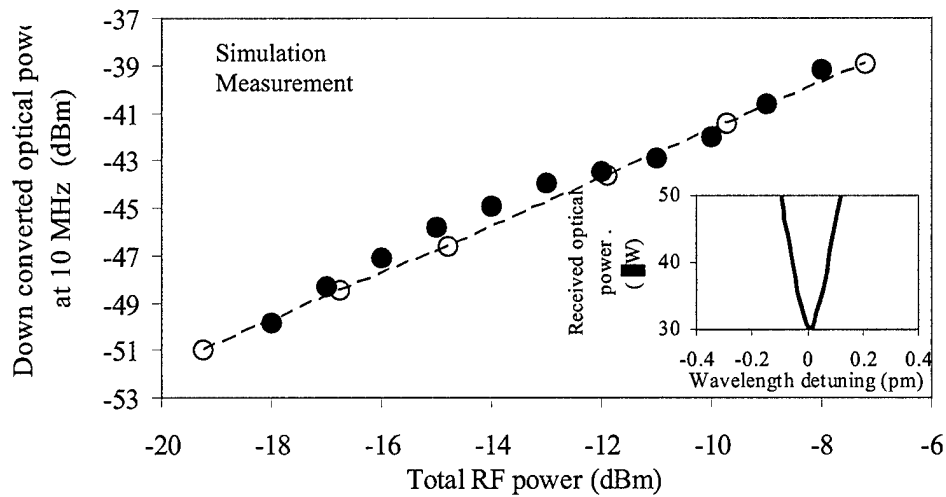


Figure 26 Measured baseband modulated (10 MHz) optical output power against m for three optical modes with different optical quality factors?

Fig. 27(a) shows the variation of the down-converted optical power at 10 MHz as a function of the modulation m and for three resonances with different quality factors. The modulation index is tuned to the desired values by changing the DC bias applied to the mixer.

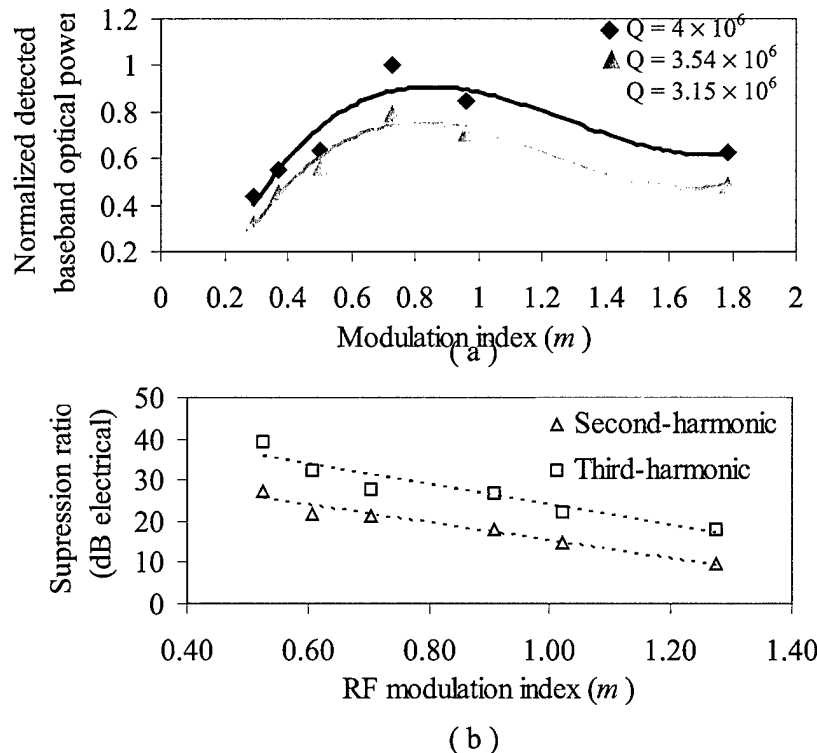
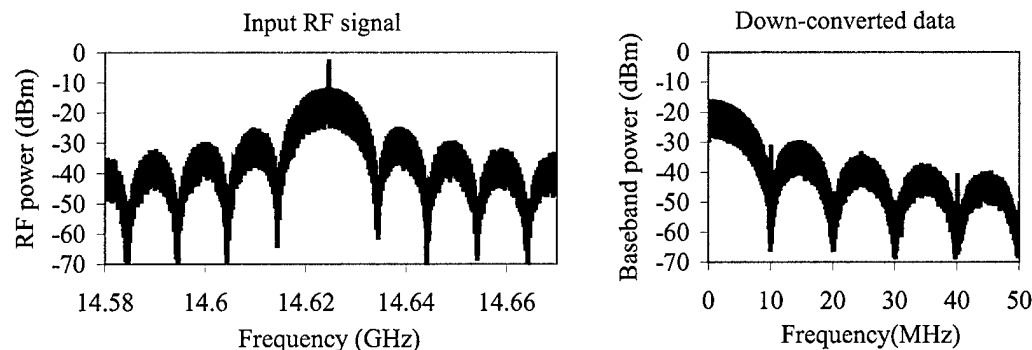
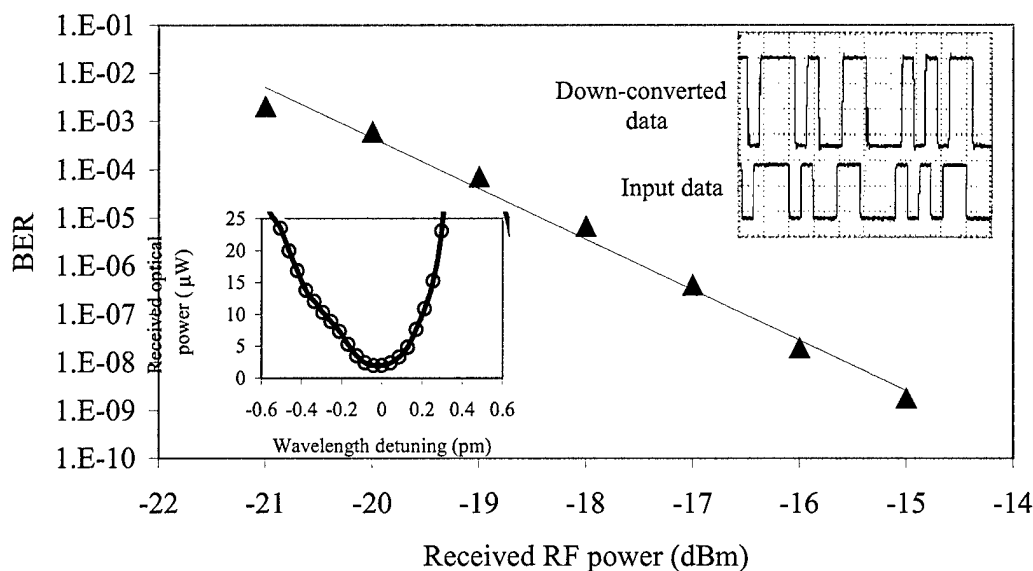


Figure 27 (a) The measured and calculated baseband modulated optical power versus total RF input power. The inset shows the optical spectrum of the WG resonance chosen for down-conversion ($Q = 2.7 \times 10^6$, $N_2 = 2.23 \times 10^{-2}$ mW/V²). (b) Measured second and third Harmonic suppression ratios (electrical) against m .

The total received RF power is about -15 dBm that corresponds to $V_0 = 0.05$ V (3). The V_{HMM} is around 0.8 V for the optical resonance used, so $V_0 < 0.25 V_{HMM}$ guarantees device operation in the small-signal regime. As may be seen in Fig. 27(a), down-conversion efficiency is maximized around $m = 0.8$, in very good agreement with the simulated curve for an ideal square law mixer. Also, as anticipated, the amount of down-converted power increases as we increase the optical Q (a larger Q results in a larger V_{HMM} and therefore a larger N_2). To evaluate the linearity of the down-conversion process we have measured the detected power at the second and third harmonic of the baseband signal (20 MHz and 30 MHz respectively).



(a)



(b)

Figure 28 Measurement results of photonic data down-conversion in LiNbO₃ microdisk modulator. (a) The frequency spectrum of the input RF signal and down-converted signal. The RF carrier frequency is 14.6 GHz and it is modulated by a 10 Mb/s 2⁷-1 NRZ PRBS bit stream. (b) The BER sensitivity of the photonic RF receiver. The RF power is the measured RF power within 10 MHz bandwidth centered around 14.6 GHz. The right inset shows the input and detected data in time domain. The left inset shows the optical spectrum of the selected WG resonance

In a perfect square law modulator the third harmonic should be absent but the chosen optical resonance doesn't have an ideal symmetric shape and so generates odd harmonics. Fig. 27(b) shows the harmonic suppression ratio against m . As predicted (Fig. 20(b)) the suppression ratio

decreases when we increase m . At $m = 0.8$ the second-harmonic suppression ratio is about 17 dB (electrical).

For experimental demonstration of data transmission we use the arrangement in Fig. 24(c) but replace the signal generator with a NRZ pattern generator and the photodetector with a digital photoreceiver. The photoreceiver has a -3 dB frequency bandwidth of 120 MHz and a sensitivity of -34.5 dBm. Fig. 28(a) shows the measured frequency spectrum of the input RF signal and the down-converted signal after detection. The carrier frequency is 14.62 GHz and the baseband data is a 10 Mb/s NRZ 2^7-1 pseudo-random bit stream (PRBS). Fig. 28(b) shows the measured bit error ratio (BER) against the total RF input power. The received RF power is defined as the measured RF power within 10 MHz bandwidth centered around 14.6 GHz. The left inset shows the spectrum of the optical resonance with $Q = 2 \times 10^6$. The inset on the right shows the input and down-converted data in the time domain.

In Fig. 29 the measured eye diagrams at 10 Mb/s, 50 Mb/s and 100 Mb/s are shown. The received RF power is -15 dBm. In this particular case the maximum data rate is limited by the optical Q to approximately 100 Mb/s.

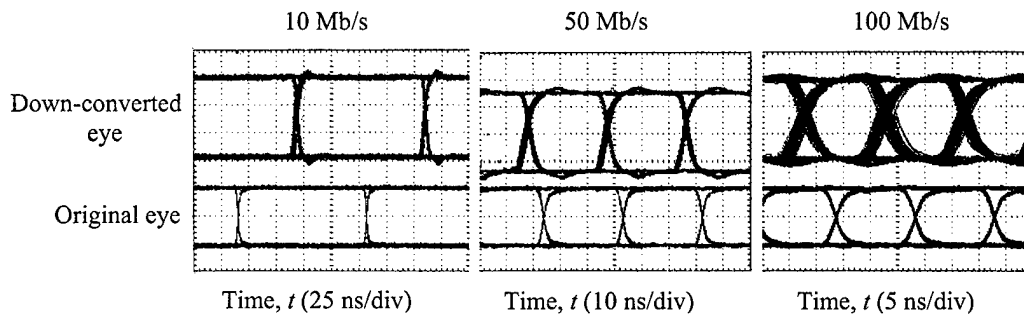


Figure 29 Measured eye diagrams at 10 Mb/s, 50 Mb/s and 100 Mb/s.

We note that the detected down-converted signal can be increased by reducing the disk thickness (t) and employing a high- Q RF ring resonator (both these factors lead to a larger N_2 coefficient). We can also reduce the signal-to-noise in the photonic receiver by employing a bandpass optical filter after the microdisk modulator. A filter with a bandwidth less than $4f_{RF}$ can eliminate high frequency optical components around $2f_{RF}$ given and therefore reduce the noise generated by the optical power at these frequencies in the slow-speed photoreceiver.

We have designed and fabricated a 4-patch antenna array with 1 GHz bandwidth around 14.6 GHz carrier frequency to demonstrate the first microphotonic RF wireless receiver in Ku-band. The antenna is directly attached to the microdisk modulator. The transmitter is a similar 4-patch array and is fed through an amplifier. We have successfully transmitted 10 Mb/s data stream (NRZ 2^7-1 PRBS) over a short link. Fig. 30(a) shows a photograph of the antenna coupled Ku-band microdisk modulator. Fig. 30(b) shows the spectrum of the WG resonance selected for nonlinear optical modulation. The laser was tuned to the minimum transmission point. In Fig. 30(c) the transmitted and received data amplitude is demonstrated in time domain.

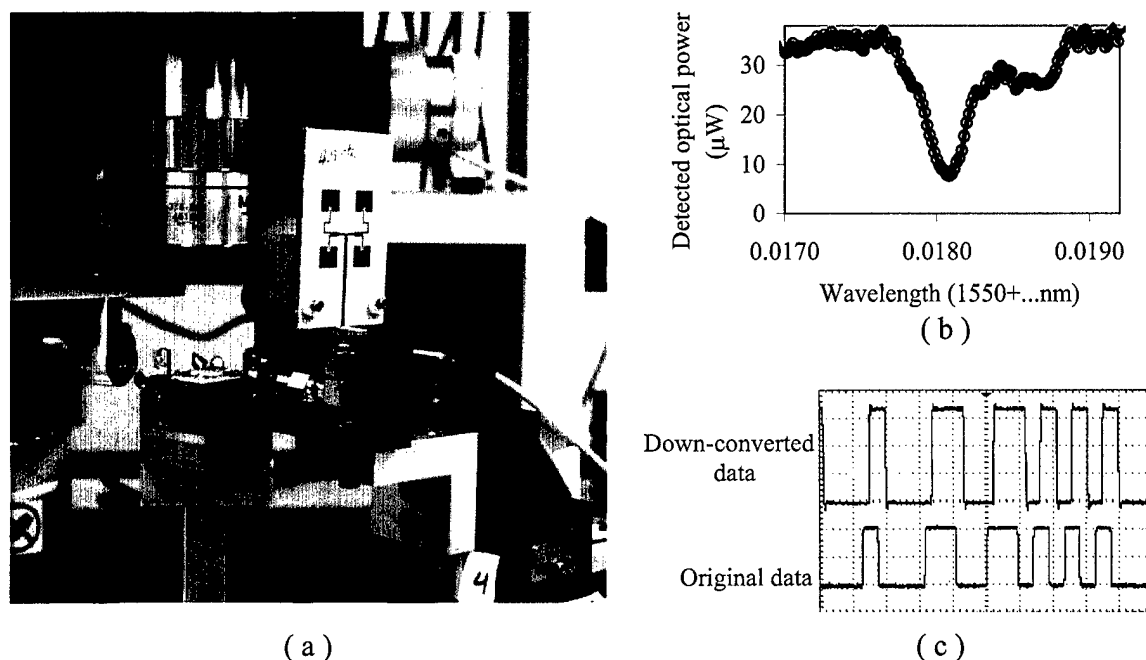


Figure 29 (a) photograph of the experimental arrangement for photonic RF wireless receiver demonstration. A four patch antenna array with 1 GHz bandwidth around 14.6 GHz carrier frequency is directly attached to the 14.6 GHz LiNbO₃ microdisk modulator. (b) The optical power spectrum of the WG resonance used for nonlinear optical modulation. (c) The original and down-converted data measured in time domain.

Conclusion

Results of analysis, modeling, device fabrication and measurement indicate that a microphotonic RF receiver is feasible. A novel self-homodyne photonic RF receiver based on a microdisk modulator has been developed. Down-conversion occurs in the optical domain through *nonlinear* modulation, thereby eliminating the need for an RF local oscillator and mixer. Experimental verification of the receiver architecture has been achieved by measuring BER and eye-diagrams using signals down-converted from a NRZ digital data modulated transmitted carrier RF signal with $f_{RF} = 14.6$ GHz carrier frequency. The microdisk modulator and the photonic self-homodyne architecture have the potential to be incorporated into a photonic integrated circuit by using alternative electro-optic materials (such as polymers and compound semiconductors). Reducing the disk diameter will extend the carrier frequency into mm-wave regime so that this receiver architecture has potential to be used in future indoor mm-wave wireless systems. The main challenges for future are

- 1) Improving the sensitivity of the microdisk modulator.
- 2) Designing more compact and efficient narrow band and directional planar antennas.
- 3) Reducing the size and a proper package design.
- 4) Increasing the carrier frequency to mm-wave regime.

Publications

We have published a number of papers describing our work of both part I and part II of this research program [23-33].

References

- [1] R. S. Weis and T. K. Gaylord, "Lithium Niobate: Summary of physical properties and crystal structure," *Appl. Phys. A*, Vol. 37, pp 191-203, 1985.
- [2] W. M. Robertson, G. Arjavalingam, and G. V. Kopcsay, "Broadband microwave dielectric properties of LiNbO₃," *Electron. Lett.*, vol. 27, pp. 175-176
- [3] K. K. Wong, "Properties of lithium niobate," *ISPEC*, institution of electrical engineers, 1989.
- [4] A. M. Prokhov and Y. S. Kuz'minov, "Physics and chemistry of crystalline lithium niobate," The Adam Hilger series on optics and optoelectronics, 1990.
LiNbO₃ microdisk modulator
- [5] D. A. Cohen, "Lithium Niobate microphotonic modulators" , Ph.D dissertation, USC May 2001.
- [6] V. S. Ilchenko, A. A. Savchenkov, A. B. Matsko, and L. Maleki, "Sub-microwatt photonic microwave receiver", *IEEE photonics technol.*, Vol 14, No. 11, Nov 2002.
- [7] B. Little, J. P. Laine, H. A. Haus, "Analytic theory of coupling from tapered fibers and half-blocks into microsphere resonators", *J. of Lightwave Technol.*, Vol. 17, No. 4, pp 704-714, April 1999.
- [8] S. Schiller and R. L. Byer, "High-resolution spectroscopy of whispering gallery modes in large dielectric spheres", *Optics Lett.*, Vol. 16, No. 15, pp 1138-1440, Aug. 1991.
- [9] M. L. Gorodetsky and V. S. Ilchenko, "High-Q optical whispering-gallery microresonators:precession approach for spherical mode analysis and emission patterns with prism couplers", *Optics comm.*, Vol. 113, pp 133-143, Dec. 1994.
- [10] T. Ikegami and K. Kubodera, "Nonlinear optical devices for switching applications", Communications, 1990. ICC 90 IEEE international conference on, Vol. 3, pp 1152-1156, Apr.
- [11] P. W. Smith, E. H. Turner, and P. J. Maloney, "Electro-optic nonlinear Fabry-Perot devices", *IEEE J. of quantum electron.*, Vol. 14, No. 3, pp 207-212, March 1978.
- [12] R. S. Jameson and W. T. Lee, "Operation of an all-optical bistable device dependent upon incident and transmitted optical power", *IEEE J. of quantum electron.*, Vol. 25, No. 2, pp 139-143, Feb. 1989.
- [13] Y. S. Wu, and F. J. Rosenbaum, " Mode chart for microstrip ring resonators ", *IEEE trans. on microwave theory and techniques*, Vol. MTT-21, pp 487-489, July 1973.
- [14] A. Khanna, and Y. Garault, "Determination of loaded, unloaded, and external quality factors of a dielectric resonator coupled to a microstripline", *IEEE trans. on microwave theory and techniques*, Vol. MTT-31, No 3, pp 261-264, March 1993.
- [15] S.-L. Lu, and A. M. Ferendeci, " Coupling parameters for a side-coupled ring resonator and a microstrip line ", *IEEE trans. on microwave theory and techniques*, Vol. 44, No. 6, pp 953-956, June 1996.
- [16] B. Vidal, V. Polo, J. L. Corral, and J. Marti, "Efficient architecture for WDM photonic microwave filters," *IEEE Photon. Technol. Lett.*, vol. 16, pp. 257-259, Jan. 2004.
- [17] P. O. Hedekvist, B.-E. Olsson, and A. Wiberg, "Microwave harmonic frequency generation utilizing the properties of an optical phase modulator," *J. Lightwave Technol.*, vol. 22, pp. 882-886, March 2004.
- [18] Hirata, M. Harada, and T. Nagatsuma, "120-GHz wireless link using photonic techniques for generation, modulation, and emission of millimeter-wave signals," *J. Lightwave Technol.*, vol. 21, pp. 2145-2153, Oct. 2003.

- [19] G. K. Gopalakrishnan, W. K. Burns, and Catherine H. Bulmer, "Microwave-optical mixing in LiNbO₃ modulators," *IEEE Trans. Microwave Theory and Tech.*, vol. 41, pp. 2383-2391, Dec 1993.
- [20] M. Tsuchiya and T. Hoshida, "Nonlinear photodetection scheme and its system applications to fiber-optic millimeter-wave wireless down-links," *IEEE Trans. Microwave Theory and Tech.*, vol. 47, pp. 1342-1350, July 1999.
- [21] A. A. Abidi, "Direct-conversion radio transceivers for digital communications," *IEEE J. Solid-State Circuits*, vol. 30, pp 1399-1410, Dec 1995.
- [22] Y. Shoji, K. Hamaguchi, H. Ogawa, "Millimeter-wave remote self-heterodyne system for extremely stable and low cost broad-band signal transmission", *IEEE Trans. Microwave. Theory and Tech*, vol. 50, pp1458-1468, June 2002.
- [23] M. Hossein-Zadeh, A. F. J. Levi, "RF Mixing in a LiNbO₃ microdisk modulator," *IEEE/LEOS summer topical meetings*, 2004, section MC4: WGM microcavities IV.
- [24] M. Hossein-Zadeh, A. F. J. Levi, "Self-Homodyne RF-Optical LiNbO₃ microdisk receiver," *Technical digest CLEO conference*, 2004, Microwave photonics session, CWQ5.
- [25] M. Hossein-Zadeh, A. F. J. Levi, "Self-Homodyne RF-Optical LiNbO₃ microdisk receiver," *GOMACTech-04 conference*, 2004.
- [26] M. Hossein-Zadeh, A. F. J. Levi, "A new electrode design for microdisk electro-optic RF modulator," *Technical digest CLEO conference*, 2003, CTuW3.
- [27] M. Hossein-Zadeh, F. Harriague, A. F. J. Levi, "Mb/s data transmission over an RF-Optical-link using a LiNbO₃ microdisk optical modulator," *Technical digest CLEO conference*, 2002, pp 277.
- [28] M. Hossein-Zadeh, A. F. J. Levi, "14.6 GHz LiNbO₃ microdisk photonic self-homodyne RF receiver," submitted to *Journal of Light Wave Technology*, April 2004.
- [29] M. Hossein-Zadeh, A. F. J. Levi, "Mb/s data transmission over a RF fiber-Optic link using a LiNbO₃ microdisk optical modulator," *Solid-State Electronics*, 46, 2173-2178, 2002.
- [30] D.A. Cohen, M. Hossein-Zadeh, A. F. J. Levi, "High-Q microphotonic electro-optic modulator," *Solid-State Electronics*, 45, 1577-1589, 2001.
- [31] D.A. Cohen, M. Hossein-Zadeh, A. F. J. Levi, "Microphotonic modulator for microwave receiver," *Electronics Letters*, 37, 300-301, 2001.
- [32] D. A. Cohen and A. F. J. Levi, "Microphotonic millimeter-wave receiver architecture," *Electron. Lett.*, 37, 37-39, 2001.
- [33] D. A. Cohen and A. F. J. Levi, "Microphotonic components for a mm-wave receiver," *Solid State Electron.*, 45, 495-505, 2001.

RF mixing in LiNbO₃ microdisk modulator

Mani Hossein-Zadeh and A.F.J Levi

Advanced Network Technology Lab, University of Southern California, Los Angeles, CA 90089-2533

Phone: (213)-740-5583, email: hosseinz@usc.edu

Abstract- For the first time we demonstrate that nonlinear electro-optic modulation in a LiNbO₃ microdisk modulator can be used to achieve RF mixing in optical domain.

I. INTRODUCTION

A LiNbO₃ microdisk modulator [1] operates based on resonant electro-optic interaction of optical whispering-gallery modes (WGM) and E-field generated by an RF resonator [2]. Long photon lifetime, RF voltage gain and simultaneous RF-optical resonance provide a high RF-optical sensitivity that can be used in RF-photonics signal processing applications [3,4]. Fig. 1 shows the simulated optical output power of a typical LiNbO₃ microdisk modulator in the transmitting mode when the laser wavelength (λ_{laser}) is tuned to one of the resonant wavelengths (λ_{res}) where a transmission dip occurs (modulator parameters are chosen very close to the experimental values). The sensitivity of the microdisk can be quantified by a voltage amplitude V_{HMM} that modulates half of the optical mode power ($P_{o,in} - P_{o,min}$).

In this paper we demonstrate that the second-order nonlinearity of an optical microdisk modulator, biased at its minimum transmission point, may be used to realize the optical mixing process required to extract the baseband signal from the transmitted carrier RF signal.

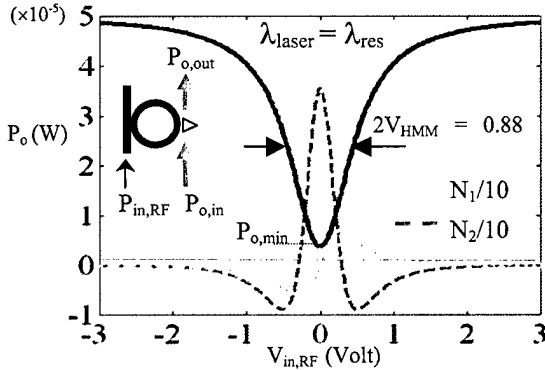


Fig. 1. The simulated optical output power of a typical LiNbO₃ microdisk modulator as a function of input RF voltage. The dashed and dotted lines are generated as the first and second Taylor coefficients in an expansion of the optical transfer function (solid line). Simulation parameters: $Q = 3.7 \times 10^6$, DC shift = 0.135 pm/V, $G_V = 6$, distributed loss (/cm) = 0.0075, optical coupling factor = 0.114, optical input power ($P_{o,in}$) = 50 μ m.

II. RF-PHOTONIC MIXER

A. Second-order nonlinear modulation

We can expand the electro-optic transfer function of the microdisk, $P_o(V_{RF})$ around $V_{RF} = 0$ as:

$$P_o = N_0 + N_1 V_{RF} + \frac{N_2}{2} V_{RF}^2 + \dots \quad (1)$$

Where N_i ($i > 0$) is the i th Taylor expansion coefficient of $P_o(V_{RF})$ at $V_{RF} = 0$ and N_0 is the minimum transmitted optical power ($P_{o,min}$). When the modulator is biased at its extreme nonlinear operation regime ($\lambda_{laser} = \lambda_{res}$) and $V_{RF} < 4V_{HMM}$ (small signal regime), the behavior of P_o can be estimated as $P_{o,min} + (1/2)N_2 V_{RF}^2$. The dotted and dashed lines in Fig 1 are the calculated N_1 and N_2 coefficients for the simulated transfer function (solid line). As one may see, around the transmission minimum, N_1 is zero and the modulator is effectively operating as a square-law RF-photonics device. N_2 is the second-order modulation strength and its value is determined by modulator parameters and optical input power. An optical detector is used to convert the optical power to an electrical signal creating an effective square-law RF mixer.

B. Self-homodyne RF-photonics receiver

In a self-homo and self-heterodyne wireless transmission system the transmitter broadcasts an RF modulated signal and the local carrier so the baseband/IF signal can be down-converted by mixing the received carrier and modulated signal in a nonlinear device (self-mixer) [5]. If the baseband is a pure sinusoidal signal, the received RF voltage can be expressed as:

$$V_{RF} = V_0 (1 + m \cos(\omega_b t)) \cos(\omega_{RF} t) \quad (2)$$

Where m is the modulation index, ω_b is the baseband frequency and ω_{RF} is the RF carrier frequency. If we feed this signal to a microdisk modulator biased at pure nonlinear modulation regime ($\lambda_{laser} = \lambda_{res}$) the transmitted optical power can be written as:

$$P_o = P_{o,min} + \frac{N_2}{2} V_0^2 (1 + m \cos(\omega_b t))^2 \cos^2(\omega_{RF} t) \quad (3)$$

Expanding the second term on the right hand side of (3) one obtains a DC term, high frequency terms around $2\omega_{RF}$ and two down-converted terms at ω_b and $2\omega_b$ given by:

$$\frac{N_2 V_0^2 m^2}{8} \cos(2\omega_b t) + \frac{N_2 V_0^2}{2} m \cos(\omega_b t) \quad (4)$$

So the optical output intensity is baseband modulated and can be detected with a slow speed photodetector. The second-harmonic baseband term ($2\omega_b$) may be suppressed relative to the baseband (ω_b) by employing a transmitted carrier RF modulation format ($m < 2$). In the small-signal operating regime ($V_{RF} < 0.1V_{HMM}$), with modulation index of $m = 0.4$, a second-harmonic baseband suppression of 20 dB and down-conversion efficiency of 20% (corresponding to 20% of the total modulated optical power being modulated at baseband frequency) can be achieved.

III. EXPERIMENT AND RESULTS

The LiNbO₃ microdisk used in our experiment is 400 μ m thick, 3 mm in diameter, and has an optical free spectral range of 14.6 GHz. The RF signal applied is a 14.6 GHz RF-carrier mixed with the baseband signal in a double-balanced RF-mixer. Fig. 2(a) shows a schematic diagram of the experimental arrangement.

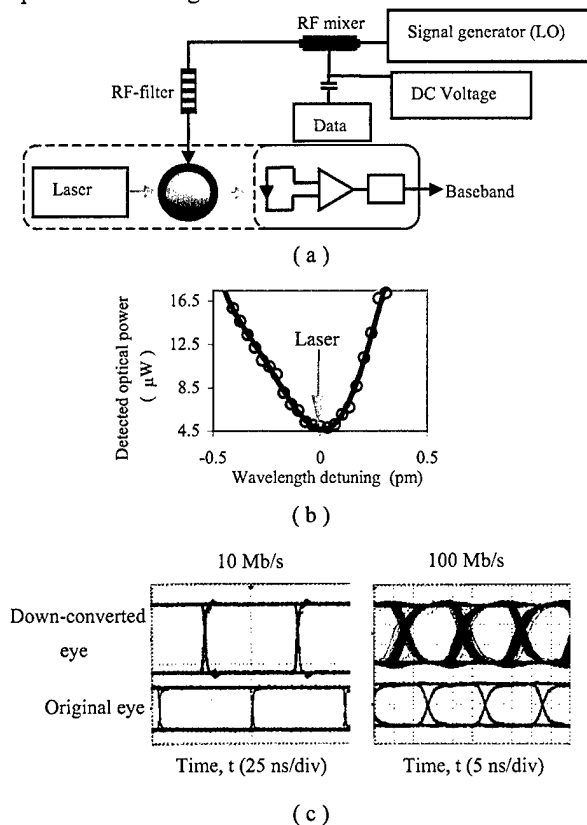


Fig. 2. (a) Schematic diagram of the experimental arrangement for demonstrating all-optical down-conversion with microdisk modulator. (b) The optical mode selected for data down-conversion with a Q of 3.5×10^6 . (c) Receiver eye-diagrams and demodulated data for 2^7-1 PRBS data sequences at 10 Mb/s and 100 Mb/s rates after electro-optical down-conversion (total RF input power = 7 dBm).

By DC-biasing the IF port of the mixer we can control the modulation index m and in our experiment $m = 0.5$. The RF signal is applied to the microdisk modulator after passing through a bandpass RF filter (14.6 GHz center frequency and 1 GHz bandwidth) to ensure any nonlinear products of the oscillator and amplifier are filtered out. Fig. 2(b) shows the optical mode selected for nonlinear modulation. Optical output is detected using a digital photoreceiver with a sensitivity of -34.5 dBm and -3 dB bandwidth of 100 MHz. Fig. 2(c) shows the clean eye-diagrams after electro-optical down-conversion when the RF carrier is modulated by a pseudo-random bit stream (PRBS 2^7-1) at 10 Mb/s and 100 Mb/s.

IV. CONCLUSION

We have proposed a novel RF mixing method based on *nonlinear* optical modulation in LiNbO₃ microdisk WGM resonator. This method is employed in a self-homodyne RF-photonics receiver where down-conversion occurs in the optical domain through *nonlinear* modulation, thereby eliminating the need for an RF local oscillator and mixer. Clean eye-diagrams at 10 Mb/s and 100 MB/s are down-converted from a transmitted carrier RF signal with 14.6 GHz carrier frequency. This is the first Ku-band microphotonic RF receiver architecture without any high-speed transistors. By reducing the microdisk diameter and improving modulator sensitivity the architecture has the potential to be used in future indoor mm-wave wireless systems.

ACKNOWLEDGEMENTS

This work is sponsored by DARPA and NASA.

REFERENCES

- [1] D. A. Cohen, M. Hossein-Zadeh and A. F. J. Levi, "High-Q microphotonic electro-optic modulator," *Solid-State Electronics*, vol 45, pp. 1577-1589, 2001.
- [2] M. Hossein-Zadeh, A. F. J. Levi, "A new electrode design for microdisk optical modulator," *CLEO Technical digest*, CTuW3, June 2003.
- [3] V. S. Ilchenko, A. A. Savchenkov, A. B. Matsko, and L. Maleki, "Sub-microwatt photonic microwave receiver," *IEEE photonics technol.*, vol 14, Nov 2002.
- [4] M. Hossein-Zadeh and A. F. J. Levi, "Mb/s data transmission over a RF fiber optic link using a LiNbO₃ microdisk optical modulator," *Solid-State Electronics*, vol. 46, pp. 2173-2178, 2002.
- [5] Y. Shoji, K. Hamaguchi and H. Ogawa, "Millimeter-wave remote self-heterodyne system for extremely stable and low cost broad-band signal transmission," *IEEE Trans. Microwave. Theory and Tech*, vol. 50, pp. 1458-1468, 2002.

Self-homodyne RF-optical microdisk receiver

M. Hossein-Zadeh and A. F. J. Levi

Department of Electrical Engineering, University of Southern California, Los Angeles, California 90089-2533
(213) 740 5583, (213) 740 9280, hosseinz@usc.scf.edu

Abstract: Nonlinear optical modulation in a LiNbO_3 microdisk RF-optical receiver is used in a self-homodyne configuration to demodulate 50 Mb/s data on an 8.7 GHz RF carrier.

©2004 Optical Society of America

OCIS codes: (070.4340) Nonlinear optical signal processing; (230.4110) Modulators; (140.4780) Optical resonators.

1. Introduction

Previous work on microdisk modulator technology was focused on the linear modulation regime [1,2]. Here, for the first time we demonstrate that the nonlinearity in the transfer function of an optical microdisk modulator when biased at its maximum transmission point may be used to optically mix and extract the baseband signal from the modulated RF signal.

2. Self-homodyne RF-optical receiver

Fig. 1 is a block diagram of the RF-optical receiver. The received RF signal, which has a transmitted carrier RF-modulation format, is fed to a microdisk optical modulator [2] biased at its maximum transmission point. The carrier and sidebands are mixed through the second-order nonlinearity in the optical transfer function of microdisk resonant modulator; hence the optical output intensity spectrum contains the baseband and high-frequency products around the second-harmonic of the carrier frequency. A photoreceiver with bandwidth matched to the baseband signal detects and automatically filters out higher-frequency components.

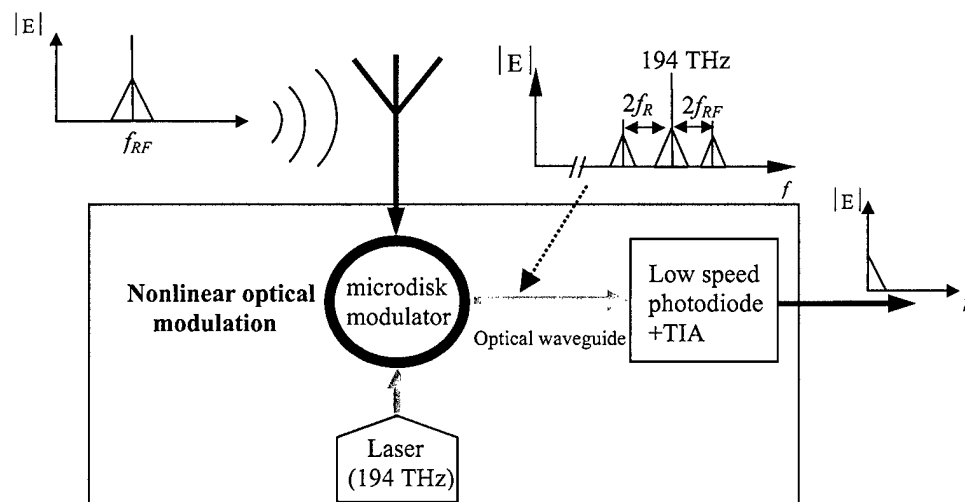


Fig. 1. RF-optical receiver architecture. The received microwave signal nonlinearly modulates the laser light, so the optical output intensity is baseband modulated. The optical signal is transmitted through a waveguide and fed to a low-speed photoreceiver for baseband detection.

3. Simulation and experimental results

Fig. 2 shows the simulated signal flow in the RF-optical microdisk receiver. The transmitted-carrier RF input signal (a) modulates the optical transfer function of the microdisk (b). When the laser emission wavelength (λ_0) is centered on the peak of the microdisk optical resonance the second-order nonlinear modulation generates the baseband and high-frequency components (c). The photodetector bandwidth (dashed line) filters out the high-frequency components and only the baseband can be converted to an electric signal. The second-order modulation ($P_{o,mod}$) is directly proportional to $\Delta\lambda_{RF}$, the maximum optical output power ($P_{o,max}$) and optical quality factor ($Q = \lambda_0/\Delta\lambda_{FWHM}$), where $\Delta\lambda_{RF}$ is the amplitude of the resonant wavelength oscillation due to applied RF voltage. For a given input voltage amplitude (RF power), $\Delta\lambda_{RF}$ is determined by the disk thickness, and the RF-resonator voltage gain [1].

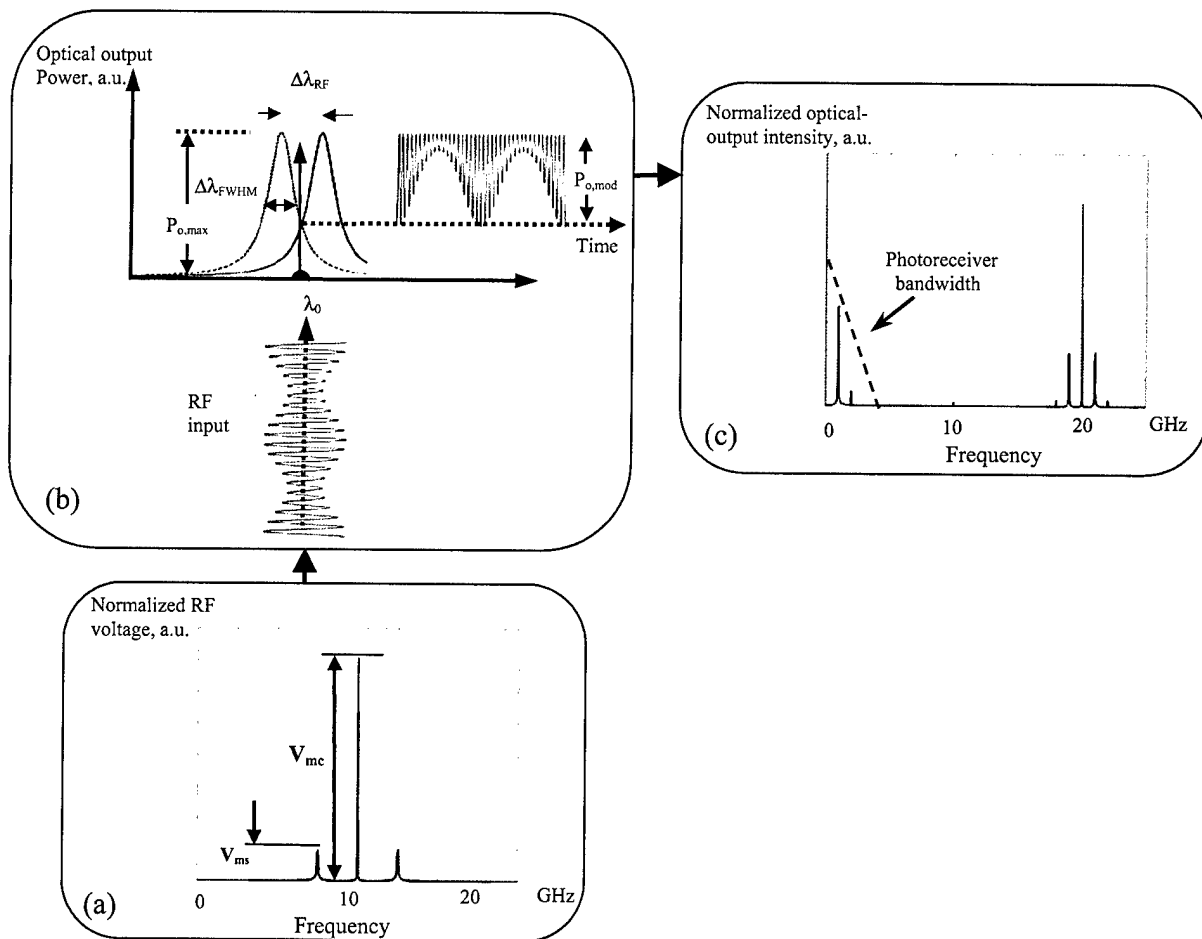


Fig. 2. The simulated signal flow in a microdisk RF-optical receiver. (a) The spectrum of transmitted-carrier RF signal. carrier frequency = 10 GHz, Baseband frequency = 1 GHz (sinusoidal) and $A = V_{mc}/V_{ms} = 7$. (b) Second-order nonlinear modulation in microdisk modulator when the laser wavelength (λ_0) has been tuned to the peak of the transfer function. (c) The spectrum of the optical output intensity. The high-frequency components are filtered out by photodetector bandwidth (dashed line) and only the baseband is converted to electric signal.

(c)

In our experiment we use a LiNbO_3 microdisk modulator with a 400 μm thick, 5.13 mm diameter disk and free spectral range of 8.7 GHz. The modulating electric field is generated by an RF-ring resonator [3] with a voltage gain of 5.5. The RF signal applied is an 8.7 GHz RF-carrier mixed with the baseband signal (data) in a double-balanced RF-mixer. By DC-biasing the IF port of the mixer we can control the magnitude of transmitted power at carrier frequency and adjust the carrier – sideband ratio A (in our experiment $A = V_{mc} / V_{ms} = 7$). The RF signal is applied to the microdisk modulator and finally the optical output is detected using a digital photoreceiver with 100

MHz bandwidth. The laser wavelength ($\lambda_0 \approx 1550$ nm) is tuned to the maximum transmission of an optical resonance of the microdisk modulator. The measured optical Q of the mode is 2×10^6 and transmitted optical output power ($P_{o,max}$) is 20 μ W. Fig. 3 shows the receiver eye-diagrams for 2^7-1 PRBS data sequences at 10 Mb/s and 50 Mb/s rates after electro-optical down-conversion from 8.7 GHz RF carrier frequency. The measured bit error ratios are 10^{-9} and 8×10^{-9} respectively.

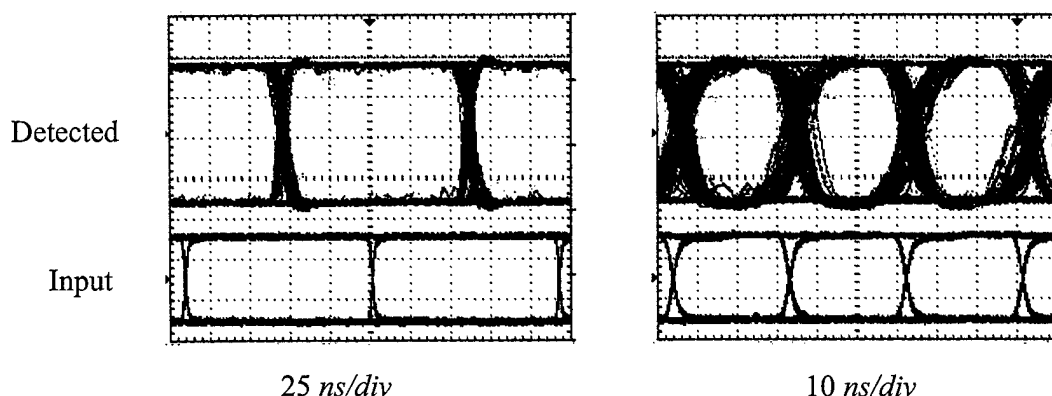


Fig. 3 Receiver eye-diagrams for 2^7-1 PRBS data sequences at 10 Mb/s and 50 Mb/s rates after electro-optical down-conversion from 8.7 GHz RF carrier frequency. The measured bit error ratios are 10^{-9} (5.6 dBm RF input power) and 8×10^{-9} (9.5 dBm RF input power) respectively.

4. Conclusion

A novel self-homodyne RF-optical receiver has been demonstrated. In this new approach the down-conversion occurs in the optical domain through *nonlinear* modulation in a microdisk modulator and there is no need for an RF local oscillator and mixer.

5. References

- 1 M. Hossein-Zadeh, A. F. J. Levi, "Mb/s data transmission over an RF-optical-link using a LiNbO₃ microdisk optical modulator", *Solid-State Electronics* **46**, 2173-2178 (2002)
- 2 D. A. Cohen, M. Hossein-Zadeh, and A. F. J. Levi, "High-Q microphotonic electro-optic modulator", *Solid-State Electronics* **45**, 1577-1589 (2001)
- 3 M. Hossein-Zadeh, and A.F.J Levi, "A new electrode design for microdisk optical modulator", CLEO 2003 Technical digest, CTuW3.

Self-homodyne RF-optical LiNbO₃ microdisk receiver

Mani Hossein-Zadeh and A.F.J Levi

Advanced Network Technology Lab, University of Southern California, Los Angeles, California

1-213-740-7318 / alevi@usc.edu

Abstract

A novel RF-optical receiver architecture based on nonlinear optical modulation in a LiNbO₃ microdisk modulator is presented. This is the first RF-optical receiver without high-speed electronic components for transmitted carrier links. We demonstrate receiver operation by demodulating 50 Mb/s digital data from a 8.7 GHz carrier frequency.

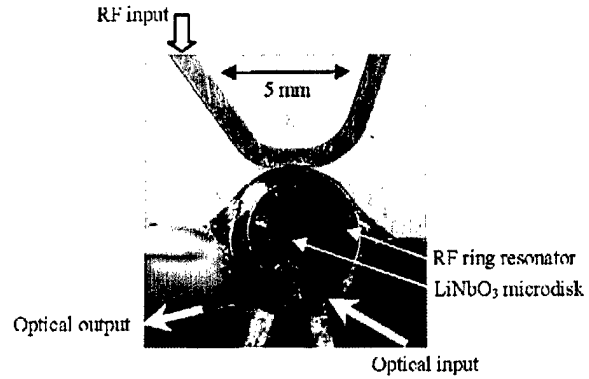
1. Introduction

In homodyne and super-heterodyne RF receiver architectures local oscillators (LOs) and mixers are used to down-convert and extract the baseband information from the received RF signal. Due to a desire for reduced part counts, size, weight, power consumption in high-carrier frequency short distance applications self-homo and self-heterodyne systems have been proposed [1,2]. In a self-homo and self-heterodyne transmission system the transmitter broadcasts a RF modulated signal and the local carrier so the baseband/IF signal can be down-converted by mixing the received carrier and modulated signal in a nonlinear device (self-mixer). The receiver power consumption, phase noise, and complexity are reduced as a result of eliminating the LO and the mixer. Although such an approach suffers from reduced power efficiency, it has been shown that it can lower overall cost and complexity in mm-wave local area networks and indoor wireless transmission systems [1]. In this paper we demonstrate that the second-order nonlinearity of an optical microdisk modulator, biased at its maximum transmission point, may be used to realize the mixing process required to extract the baseband signal from the transmitted carrier RF signal.

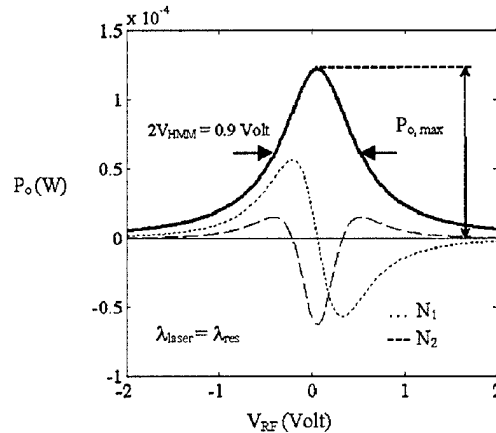
2. LiNbO₃ microdisk modulator

Fig 1(a) is a photograph of the LiNbO₃ modulator configuration. The optical power from a tunable laser is fed by fiber to a lens system that focuses laser light through a microprism and couples the light to the Whispering-Gallery (WG) modes of microdisk. A second prism couples out the optical power that is fed by a second fiber to an optical receiver. Typically, a microdisk modulator has a very high sensitivity within a limited bandwidth centered at frequencies equal to integral multiples of the optical free spectral range (FSR) [3]. The optical transfer function of the microdisk modulator has a Lorentzian shape around each resonant wavelength (λ_{res}) with a loaded optical-Q ($Q = \lambda_0/\Delta\lambda_{FWHM}$) limited by optical coupling factor (κ_0) and the distributed internal loss (α). The modulating voltage across the optical mode is created by an RF-ring resonator [4] with a voltage gain G_v at resonance [5]. Fig. 1(b) shows the simulated optical output power of a typical LiNbO₃ microdisk modulator as a function of input RF voltage (notice that the actual interacting RF voltage seen by

the optical mode is larger due to electrical resonance). The laser wavelength (λ_{laser}) is tuned to an optical resonance of the microdisk so in the absence of an external voltage the transmitted optical power is maximized



(a)

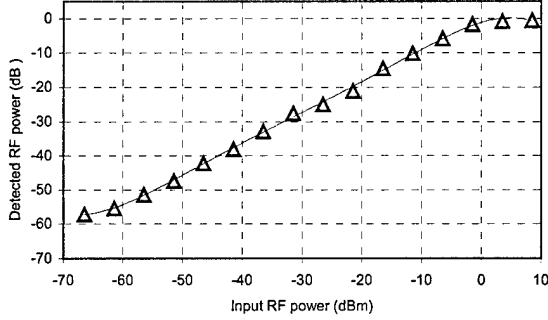


(b)

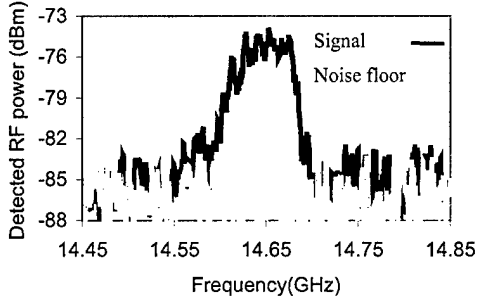
Figure 1. Photograph of a LiNbO₃ microdisk modulator with two prism couplers and the ring resonator. (b) The simulated optical output power of a typical LiNbO₃ microdisk modulator as a function of input RF voltage. The dashed and dotted lines are generated as the first and second Taylor coefficients in an expansion of the optical transfer function (solid line).

The sensitivity of the modulator can be quantified by a voltage amplitude V_{HMM} that modulates half of the maximum transmitted power ($P_{o,max}$). V_{HMM} is determined by the optical-Q, disk

thickness (t_d), the electro-optic coefficient (r_{33}) and G_v . In our simulation the modulator parameters are chosen to be representative of the experimental values: $Q = 4 \times 10^6$ (corresponding to $\alpha = 0.014 \text{ cm}^{-1}$ and $\kappa_0 = 0.08$), $t_d = 400 \text{ }\mu\text{m}$, $G_v = 6 \text{ V}$, $V_{HMM} = 0.45 \text{ V}$ and input optical power = 1 mW .



(a)



(b)

Figure 2. (a) Detected RF power at 14.5 GHz versus RF input power. The detected power is normalized to saturation power. (b) Detected RF power versus input RF frequency at -66 dBm RF power.

Fig. 2(a) shows the linear modulated optical power at 14.5 GHz vs. RF input power for a $400 \text{ }\mu\text{m}$ thick and 3 mm diameter LiNbO_3 disk that has an FSR of 14.5 GHz . The optical mode used in the experiment had a Q of 4.5×10^6 and the laser wavelength is tuned to the middle of the mode slope. The modulation is detected with an amplified high-speed optical detector. The detected power is normalized to the saturation power at which the linear portion of the optical mode is completely modulated. In this case the saturation occurs at 0 dBm RF input power that corresponds to a V_{HMM} of about 0.32 V . Fig. 2(b) shows the detected RF power versus input RF frequency at -66 dBm (250 pW) RF input power. As may be seen even at sub-nanowatt regime a signal-to-noise ratio of about 10 dB and bandwidth of about 70 MHz is obtained.

3. Self-homodyne RF-optical receiver

A self-homodyne RF-optical receiver replaces the function of a single-ended diode or FET mixer in a transmitted carrier wireless link with a sensitive optical modulator that performs down-

conversion in the optical domain. In this approach the nonlinear dependence of transmitted optical power (P_o) on applied RF voltage (V_{RF}) is the source of nonlinearity in the system. Fig. 3 illustrates the block diagram of the self-homodyne RF-optical receiver.

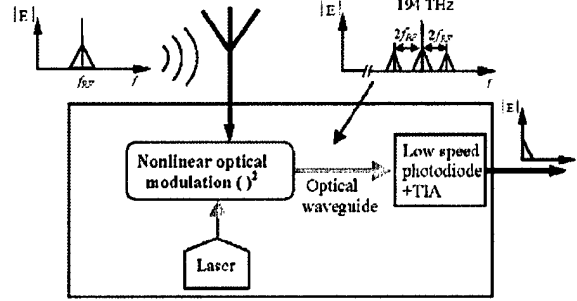


Figure 3. RF-optical receiver architecture. The transmitted carrier received microwave signal nonlinearly modulates the laser light in optical modulator. The baseband intensity modulation is generated as a result of carrier-sideband mixing in optical domain. Finally optical output is fed to a low-speed photodetector for baseband detection.

The received RF signal that contains both sidebands and the center frequency (transmitted-carrier double-sideband modulation format) is fed to an optical modulator biased at its nonlinear operating point. The carrier and sidebands are mixed through the second-order nonlinearity, hence the optical output intensity spectrum contains the baseband and high-frequency products around the second-harmonic of the carrier frequency. A photoreceiver with a bandwidth matched to the baseband signal detects and automatically filters out the high-frequency components. In this way the bandwidth of electrical circuitry used in the system is limited to that of the baseband signal. The efficiency of a RF-optical receiver strongly depends on the sensitivity of the optical modulator and the magnitude of its second-order nonlinearity. Given that most wireless links only require a limited bandwidth around a high frequency carrier, a microdisk modulator is a suitable choice for this application since it fulfills both criteria when biased at maximum optical transmission. We can expand the electro-optic transfer function of the microdisk, $P_o(V_{RF})$ around $V_{RF} = 0$ as:

$$P_o = N_0 + N_1 V_{RF} + N_2 V_{RF}^2 + \dots$$

Where N_i ($i > 0$) is the i th Taylor expansion coefficient of $P_o(V_{RF})$ at $V_{RF} = 0$ and N_0 is the maximum transmitted optical power ($P_{o,max}$). When the modulator is biased at its extreme nonlinear operation regime ($\lambda_{laser} = \lambda_{res}$) and $V_{RF} < 4V_{HMM}$ (small signal regime), the behavior of P_o can be estimated as $P_{o,max} + N_2 V_{RF}^2$. The dotted and dashed lines in Fig 2(b) are the calculated N_1 and N_2 coefficients for the simulated transfer function (solid line). As one may see, around the transmission peak $N_2 \gg N_1$ and the modulator is effectively operating as a square-law detector. At a given voltage the value of N_2 is proportional to V_{HMM} and $P_{o,max}$. If the baseband is a pure sinusoidal signal, the received RF voltage can be expressed as: $V_{RF} = V_0(1 + m \cos(\omega_b t)) \cos(\omega_{RF} t)$ Where m is the modulation index, ω_b is the baseband frequency and ω_{RF} is the RF carrier frequency. In the pure nonlinear

modulation regime ($\lambda_{laser} = \lambda_{res}$) the transmitted optical power can be written as:

$$P_o = P_{o,max} + N_2 \times V_{RF}^2 = P_{o,max} + N_2 V_0^2 (1 + m \cos(\omega_b t))^2 \cos^2(\omega_{RF} t)$$

Expanding the second term on the right hand side of the above equation one obtains a DC term equal to $(N_2 V_0^2 / 2)(1 + m^2 / 2)$, high-frequency components centered around $2\omega_{RF}$ given by:

$$\frac{N_2 V_0^2}{2} ((1 + m^2 / 2) \cos(2\omega_{RF} t) + (m^2 / 4) \cos^2(2\omega_b t) \cos(2\omega_{RF} t)) + m \cos(\omega_b t) \cos(2\omega_{RF} t)$$

and two down-converted low frequency terms at ω_b and $2\omega_b$ given by:

$$\frac{N_2 V_0^2 m^2}{4} \cos(2\omega_b t) + N_2 V_0^2 m \cos(\omega_b t)$$

The total (nonlinearly) modulated optical power is:

$$P_o^N = |(1 + m^2 + 2m) N_2 V_0^2|$$

The second-harmonic baseband term ($2\omega_b$) may be suppressed relative to the baseband (ω_b) by employing a transmitted carrier RF modulation format ($m < 2$). In the small signal operating regime ($V_{RF} < 4V_{HMM}$), with a second-harmonic baseband suppression ratio of 10 dB ($m = 0.4$), the theoretical power efficiency of this down-conversion process is 20% corresponding to 20% of the total modulated optical power being modulated at baseband frequency. At peak optical transmission N_2 is negative so the down converted baseband signal is 180 degree shifted relative to the original signal. In a data link we may use a digital photoreceiver to detect the baseband and simply recover the original data from the data bar port. Another possible solution is to use optical transmission dips (as opposed to peaks) and bias the microdisk at its minimum transmission point. The results of simulating the signal flow in the RF optical receiver are shown in Fig. 4.

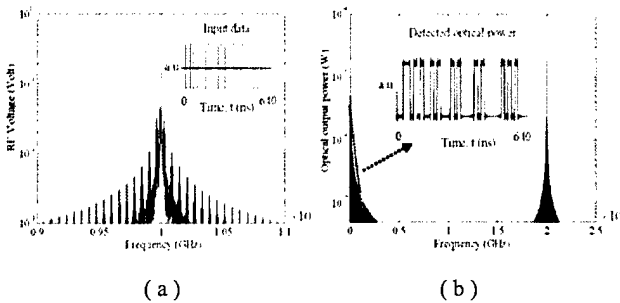


Figure 4. The simulated signal flow in a microdisk RF-optical receiver. The input RF signal is a 10 GHz RF carrier modulated by a 62.5 Gb/s data stream. (a) The spectrum of transmitted-carrier RF signal. The inset shows the original data in a 640 ns time interval. (b) The spectrum of the optical output intensity after nonlinear modulation. The high-frequency components are filtered out by the photodetector bandwidth (dashed line) and only the baseband is converted to electric signal. The inset shows the detected data in the same time interval.

In this simulation the microdisk modulator parameters are the same as Fig. 2(b). Fig 4(a) shows the spectrum of the transmitted-carrier RF input signal. The RF carrier frequency of 10 GHz is modulated by a 62.5 Mb/s data stream with modulation index of $m = 0.5$. The inset shows the original data stream in a short time interval (640 ns). Fig 4(b) shows the calculated spectrum of the optical output intensity. Nonlinear modulation generates the baseband signal and high-frequency components around 20 GHz. The photodetector bandwidth ($= 0.1$ GHz, dashed line) filters out the high-frequency components and only the baseband is converted to an electric signal. The inset shows the detected data stream again in a 40 ns time interval.

4. Experiment and results

The LiNbO₃ microdisk used in experiments is 400 μ m thick, 5.13 mm in diameter, and has an optical free spectral range of 8.7 GHz. A copper ring electrode on top of the microdisk with a resonant RF voltage gain of 5.5 at 8.7 GHz is used to create the electric field for electro-optic modulation. The RF signal applied is an 8.7 GHz RF-carrier mixed with the baseband signal in a double-balanced RF-mixer.

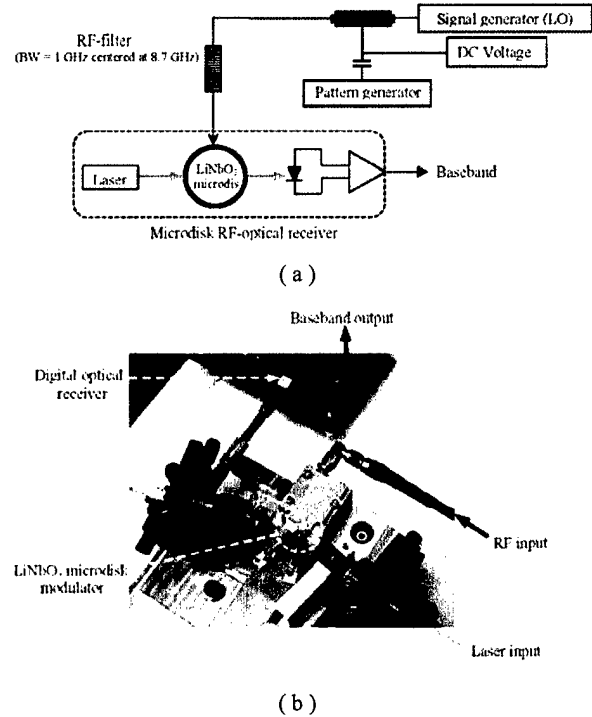
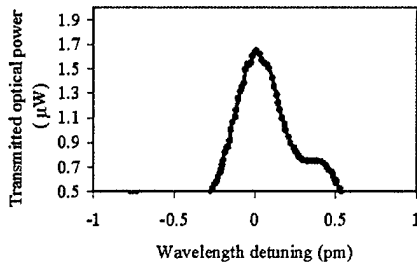


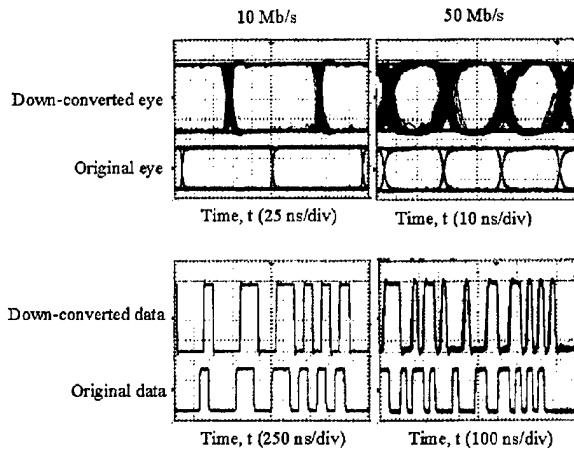
Figure 5. (a) Schematic diagram of the experimental arrangement for demonstrating all-optical down-conversion with microdisk modulator. The carrier frequency is 8.7 GHz and it is modulated with data stream from the pattern generator. (b) Picture of the RF-optical receiver showing the microdisk modulator and the digital optical receiver.

By DC-biasing the IF port of the mixer we can control the

modulation index m and consequently the magnitude of transmitted power at the carrier frequency (in our experiment $m = 0.4$). The RF signal is applied to the microdisk modulator after passing through a bandpass RF filter (8.7 GHz center frequency and 1 GHz bandwidth) to ensure any nonlinear products of the oscillator and amplifier are filtered out. Fig. 5(a) shows a schematic diagram of the experimental arrangement and Fig. 5(b) is a photograph of the RF-optical receiver showing the microdisk modulator and the digital receiver. Optical input to the microdisk modulator is provided by a tunable single mode laser with 0.3 pm wavelength resolution and < 0.5 MHz linewidth. Optical output is detected using a digital photoreceiver with a sensitivity of -34.5 dBm and -3 dB bandwidth of 100 MHz. The measured Q of the optical mode is 3.5×10^6 and transmitted optical output power ($P_{o,max}$) is $1.8 \mu\text{W}$. The laser wavelength ($\lambda_0 \approx 1550$ nm) is tuned to the optical resonator's peak transmission. Fig 6(a) shows the optical resonance spectrum used in experiment.



(a)



(b)

Figure 6. (a) The optical mode selected for data down-conversion with a Q of 3.5×10^6 . (b) Receiver eye-diagrams and demodulated data for 2^7-1 PRBS data sequences at 10 Mb/s and 50 Mb/s rates after electro-optical down-conversion from 8.7 GHz RF carrier frequency. The measured bit error ratios are 10^{-9} (5.6 dBm RF input power) and 8×10^{-9} (9.5 dBm RF input power) respectively.

Fig. 6(b) shows the detected data and clean eye-diagrams after electro-optical down-conversion when the RF carrier is modulated by a pseudo-random bit stream (PRBS 2^7-1) at 10 Mb/s and 50 Mb/s. The measured bit error ratios are 10^{-9} and 8×10^{-9} respectively.

5. Conclusion

A novel self-homodyne RF-optical receiver has been described. Down-conversion occurs in the optical domain through *nonlinear* modulation, thereby eliminating the need for an RF local oscillator and mixer. Clean eye-diagrams at 10 Mb/s and 50 Mb/s are down-converted from a transmitted carrier RF signal with 8.7 GHz carrier frequency using a microdisk modulator. The sensitivity of the microdisk modulator can be maintained up to mm-wave frequencies by reducing the disk diameter, so the receiver has potential to be used in future indoor mm-wave wireless systems.

6. ACKNOWLEDGEMENTS

This work is sponsored by DARPA.

7. References

- [1] Shoji Y, Hamaguchi K, Ogawa H. "Millimeter-wave remote self-heterodyne system for extremely stable and low cost broad-band signal transmission" IEEE Trans. Microwave. Theory and Tech, 50, 1458-1468 (2002).
- [2] Park J, Wang Y, Itoh T. A microwave communication link with self-heterodyne direct downconversion and system predistortion. IEEE Trans. Microwave. Theory and Tech, 50, 3059-3063 (2002).
- [3] Cohen DA, Hossein-Zadeh M, Levi AFJ. High-Q microphotonic electro-optic modulator. Solid-State Electronics, 45, 1577-1589 (2001).
- [4] Hossein-Zadeh M, Levi AFJ. A new electrode design for microdisk optical modulator. CLEO Technical digest, CTuW3 (2003).
- [5] Hossein-Zadeh M, Levi AFJ. Mb/s data transmission over a RF fiber optic link using a LiNbO₃ microdisk optical modulator. Solid-State Electronics, 46, 2173-2178 (2002).

A new electrode design for microdisk electro-optic RF modulator

M. Hossein-Zadeh and A. F. J. Levi

*Department of Electrical Engineering, University of Southern California, Los Angeles, California 90089-2533
(213) 740 5583, (213) 740 9280, hosseinz@usc.scf.edu*

Abstract: A LiNbO₃ microdisk electro-optic modulator that uses a microring RF resonator is presented. For the first time we demonstrate efficient modulation at the second-harmonic frequency ($2 \times v_{\text{FSR}}$) and also improve sensitivity at the fundamental frequency (v_{FSR}).

©2003 Optical Society of America

OCIS codes: (230.4110) Modulators; (230.2090) Electro-optical Devices; (230.5750) Resonators

1. Introduction

Recently a new type of electro-optic modulator at GHz frequencies has been developed that uses high-Q optical whispering gallery (WG) modes of a LiNbO₃ disk [1-3]. So far the fundamental resonant mode of a semi-ring RF resonator has been used for modulation at the optical free-spectral-range frequency (v_{FSR}) of (WG) optical modes. Here we present experimental results showing efficient modulation at $f_{\text{RF}} = 2 \times v_{\text{FSR}}$ and sensitivity improvement at $f_{\text{RF}} = v_{\text{FSR}}$ when modes of a microring resonator are excited at these frequencies. A ring resonator that is tuned to $m \times v_{\text{FSR}}$ (where m is a non-zero integer) can provide the modulating E-field with the right phase along the full photon path length around the disk and therefore doubles the electro-optic interaction at each round trip compared to a semi-ring resonator. Using the microring resonator also improves coupling to higher harmonics ($2 \times v_{\text{FSR}}$ or $3 \times v_{\text{FSR}}$) where the semi-ring has low efficiency because of poor coupling, reduced effective interaction length and radiation from open ends.

2. Experimental results

The disk employed is z-cut LiNbO₃ of radius $R = 2.9$ mm and thickness $t = 0.720$ mm. Optical coupling (in/out) is achieved using a micropism and the maximum coupled power is 100 μW . The optical Q is about 3×10^6 and $v_{\text{FSR}} \approx 7.6$ GHz (for TE WG modes). A copper ring electrode ($R = 2.9$ mm, $w = 0.5$ mm) is placed on top of the disk and is side coupled to a microstripline (see Fig.1).

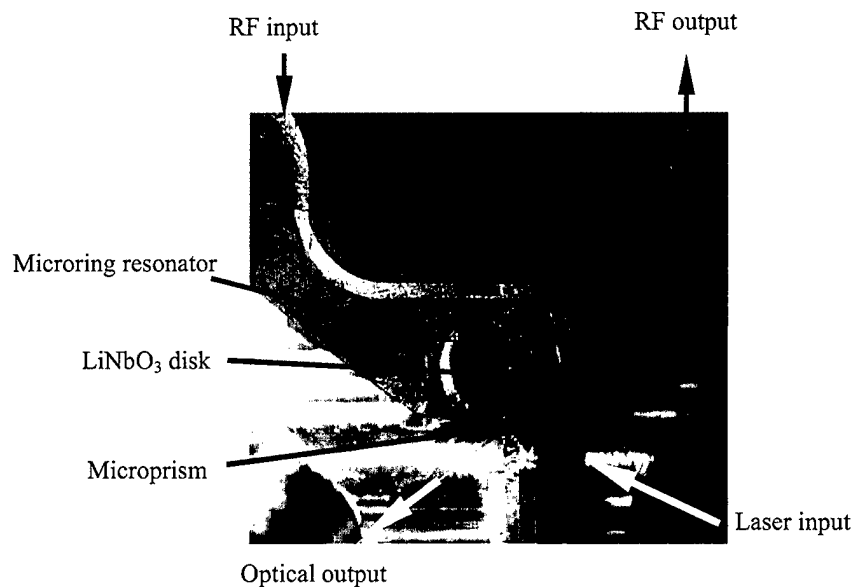


Fig. 1. Photograph of the experimental arrangement.

Fig.2 shows a 3D view of the simulated E-field distribution for even second-harmonic mode on the ring. The arrows on the ring show the E-vector directions in each region. When the period of RF oscillation is half the photon round trip time ($f_{RF} = 2 \times v_{FSR}$) the optical field stays in phase with the RF-field.

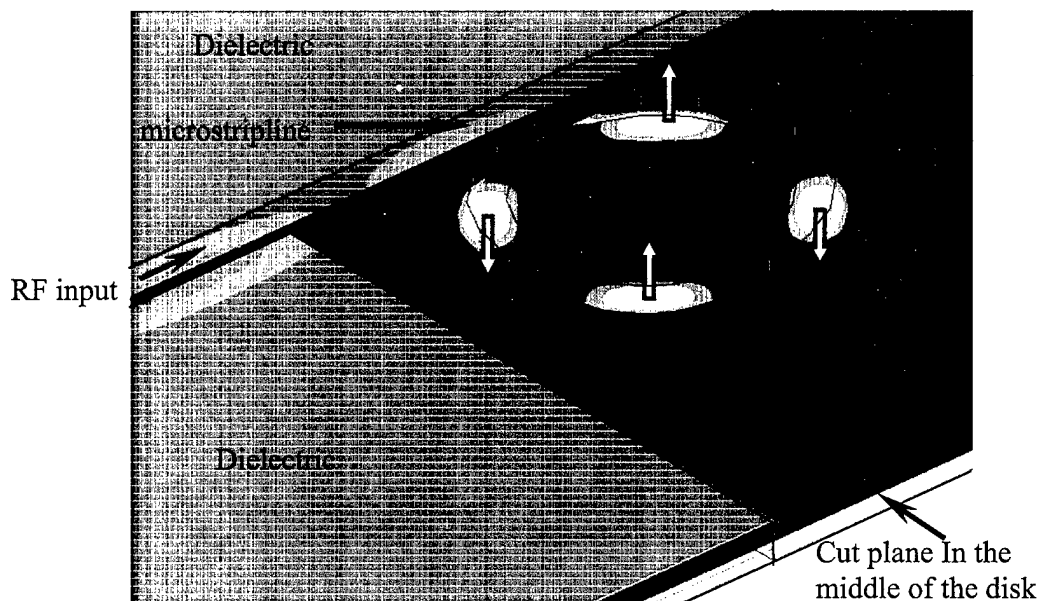


Fig. 2. 3D simulation of E-field distribution on a cut plane passing through middle of the disk when the even second-harmonic of the ring is excited.

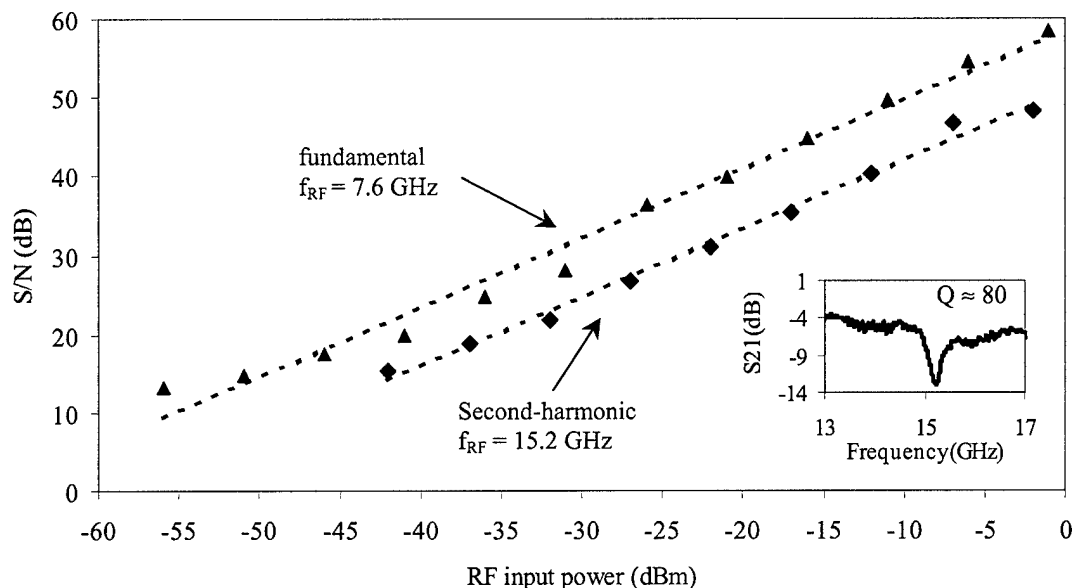


Fig. 3. Measured signal to noise ratio (of amplified signal) as a function of input RF power at fundamental ($f_{RF} = 7.6$ GHz) and second-harmonic ($f_{RF} = 15.2$ GHz) of the ring (the amplifiers have a gain of 30dB and noise figure of 1.7 dB and 2.6 dB respectively). The inset shows S_{21} spectrum when the even second harmonic of the ring ($f = 15.2$ GHz) is excited.

Fig. 3 is measured signal to noise ratio (S/N) at the fundamental ($\nu_{FSR} = 7.6$ GHz) and the second-harmonic ($2 \times \nu_{FSR} = 15.2$ GHz). At -56 dBm (≈ 2.5 nW) RF power, $f_{RF} = \nu_{FSR} = 7.6$ GHz, the SNR is 13.5 dB which is close to the best sensitivity reported with a 150 μ m thick disk and 200 μ W coupled optical power [3]. Reducing disk thickness and increasing optical power to these values will increase SNR by 18 dB.

4. Conclusion

By using a novel microring RF resonator in the design of a microdisk modulator, efficient modulation at $f_{RF} = 2 \times \nu_{FSR}$ and sensitivity improvement at $f_{RF} = \nu_{FSR}$, is demonstrated. Possibility of modulation at higher harmonics ($m \times \nu_{FSR}$) pushes the carrier frequency to higher frequencies without facing the technical problems associated with using very small diameter disks.

5. References

- 1 D. A. Cohen, M. Hossein-Zadeh, A. F. J. Levi, "High-Q microphotonic electro-optic modulator", *Solid-State Electronics* **45**, 1577-1589 (2001)
- 2 M. Hossein-Zadeh, F. Harriague, A. F. J. Levi, "Mb/s data transmission over an RF-optical-link using a LiNbO₃ microdisk optical modulator", *CLEO 2002 Technical digest*, 277.
- 3 V.S. Ilchenko, A.A. Savchenkov, A.B. Matsko, L. Maleki, "Sub-MicroWatt Photonic Microwave Receiver", *IEEE photon. Tech. Lett.*, **14**, no. 11, 1602-1604 (2002)

Mb/s data transmission over an RF-link using a LiNbO₃ microdisk optical modulator

M. Hossein-Zadeh, F. Harriague and A. F. J. Levi

Department of Electrical Engineering, University of Southern California, Los Angeles, California 90089-1111

Phone: (213) 740 5583, Fax: (213) 740 9280, hosseinz@usc.scf.edu

Abstract: For the first time, we demonstrate use of a LiNbO₃ microdisk optical modulator to transmit Mb/s data on an RF-carrier. Initial experimental results demonstrate high quality digital data transmission up to 100 Mb/s.

©2001 Optical Society of America

OCIS codes: (230.4110) Modulators; (230.2090) Electro-optical Devices; (060.4510) Optical communications; (230.5750) Resonators

1. Introduction

Recently a new microphotonic receiver with direct electrical-to-optical conversion was proposed [1,2]. The receiver uses a high-Q LiNbO₃ microdisk optical resonator that operates in simultaneous resonance with a RF microstrip resonator, whose resonant frequency is tuned to the free spectral range (FSR) of the disk. Experimental results have demonstrated efficient modulation at GHz frequencies [3,4].

In this paper, for the first time we present experimental results of Mb/s data transmission via an RF-link using the microdisk as an optical modulator.

2. The experiment

The microdisk modulator is a z-cut LiNbO₃ disk-shaped optical resonator. The disk employed has a radius $R = 2.92$ mm and a thickness $t = 0.7$ mm. Two micropisms couple laser light into and out of the microdisk. Optical input and output are mechanically tuned to maximize the coupling to TE polarized (z-oriented) whispering-gallery modes (WGM) inside the disk. All components are mounted on a planar structure to improve mechanical stability of the system (Fig. 1). A half-ring metal electrode resonator side-coupled to a microstrip line is placed on the top of the disk to provide a resonant RF electric field. The fundamental resonant frequency of the half-ring RF resonator is tuned to match the optical FSR of the disk (7.6 GHz), so that simultaneous RF and optical resonance maximize the electro-optic interaction. An RF synthesizer generates the RF carrier at 7.6 GHz. This signal is modulated by a non-return to zero pseudo-random bit-stream (NRZ 2⁷-1 PRBS) using a RF mixer. The resulting RF signal is then amplified and applied on the ring resonator to modulate the 194 THz ($\lambda = 1550$ nm) optical carrier.

The receiver is a photo diode that converts the optical output from the disk to a RF signal. The output RF signal is then amplified and mixed with the original RF carrier to demodulate the data. Finally the data goes to the receiving port of a Bit Error Ratio (BER) tester.

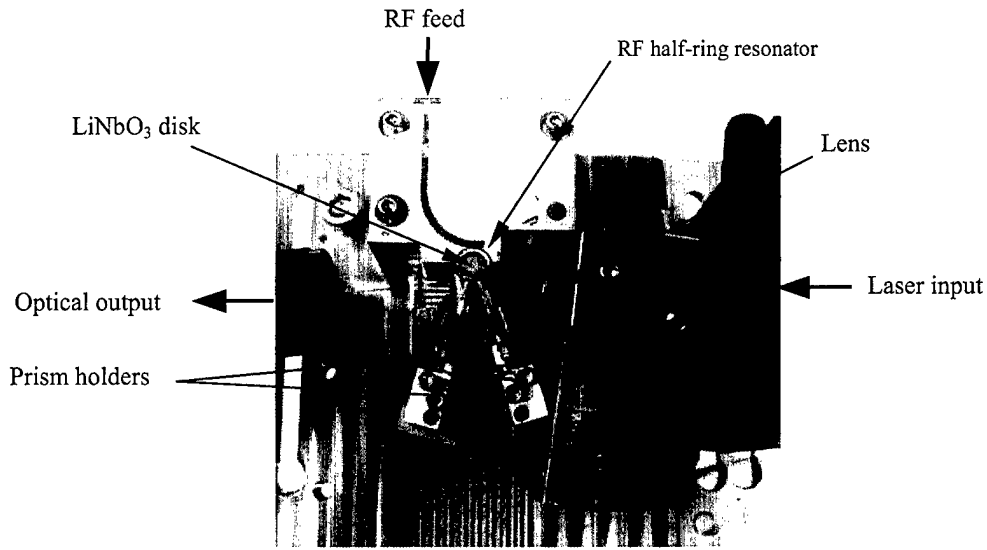


Fig. 1. Photograph of the experimental arrangement showing lens focusing system, microprisms, microdisk, RF resonator and output fiber.

3. Results

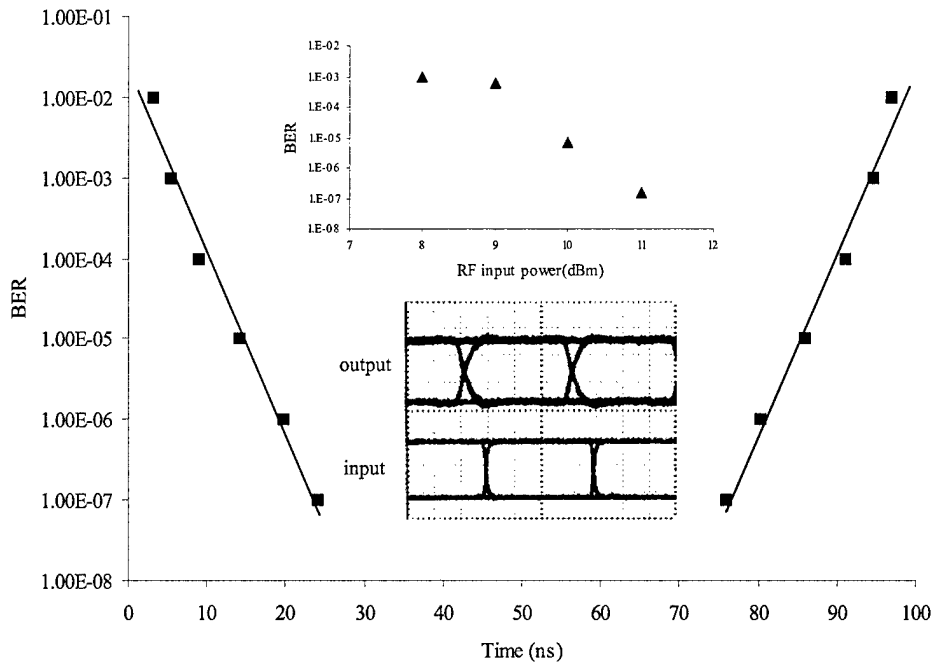


Fig. 2. Measured (10 Mb/s, 100 ns bit-period) phase-margin and eye-diagram for RF input power 11 dBm. Upper inset shows BER sensitivity to input RF power, using NRZ 2⁷ - 1 PRBS.

Fig. 2 shows the measured phase-margin of the output at 10 Mb/s (100 ns bit-period). The first inset is the measured sensitivity of BER to applied RF power. The second inset is representative of the optical output eye-diagram obtained for a 10 Mb/s NRZ 2^7-1 PRBS. The optical output power for all of these measurements is between 14 to 18 μ W. Fig. 3 shows eye-diagrams for 50 and 100 Mb/s data rates.

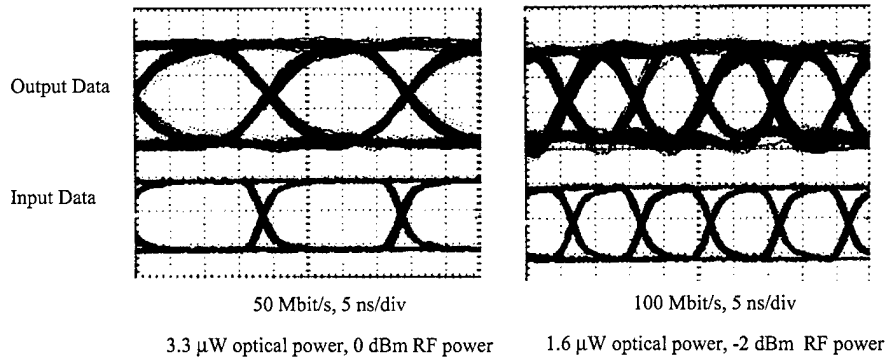


Fig.3. Measured optical eye diagrams for 50 and 100 Mb/s NRZ 2^7-1 PRBS.

4. Conclusion

High quality data transmission at Mb/s data rates over an RF-optical link using a new microdisk optical modulator has been demonstrated. The modulator is able to efficiently modulate an optical carrier ($\lambda = 1550$ nm) by a data modulated RF carrier ($f = 7.6$ GHz).

5. References

- 1 D. A. Cohen, A. F. J. Levi, "Microphotonic millimetre-wave receiver architecture", *Electronic Letters* **37**, 37-39 (2001)
- 2 D. A. Cohen, A. F. J. Levi, "Microphotonic components for a mm-wave receiver", *Solid-State Electronics* **45**, 495-505 (2001)
- 3 D. A. Cohen, M. Hossein-Zadeh, A. F. J. Levi, "Microphotonic modulator for microwave receiver", *Electronic Letters* **37**, 300 - 301 (2001)
- 4 D. A. Cohen, M. Hossein-Zadeh, A. F. J. Levi, "High-Q microphotonic electro-optic modulator", *Solid-State Electronics* **45**, 1577-1589 (2001)

14.6 GHz LiNbO₃ microdisk photonic self-homodyne RF receiver

M. Hossein-Zadeh and A. F. J. Levi

Department of Electrical Engineering

University of Southern California

Los Angeles, California, 90089-2533

Abstract

Nonlinear optical modulation combined with simultaneous photonic and RF resonance in a LiNbO₃ microdisk modulator is used to create a self-homodyne photonic RF receiver. Carrier and sidebands are mixed in the optical domain and the down-converted signal is detected using a photodetector with a bandwidth matched to the baseband signal. Receiver operation is demonstrated by demodulating up to 100 Mb/s digital data from a 14.6 GHz carrier frequency without any high-speed electronic components. A BER of 10^{-9} is measured for 10 Mb/s down-converted digital data at -15 dBm received RF power.

Index Terms

Photonic RF-receiver, Self-homodyning, Nonlinear modulation,

LiNbO₃ microdisk modulator

I. Introduction

Processing microwave and mm-wave signals in the optical domain has been the subject of intensive research for the past few years [1-3]. Placing a RF signal on an optical carrier enables a wide variety of photonic signal processing techniques and, at the same time, avoids the use of lossy transmission lines and high-speed electronic devices.

One of the key operations in microwave communication is frequency mixing. Several techniques have been proposed for RF mixing in the optical domain such as nonlinear modulation in a Mach-Zehnder modulator [4] and nonlinear detection in a photodiode [5]. Here we introduce a new photonic RF mixing technique that exploits simultaneous RF and optical resonance in an electro-optic microdisk resonator. This is used to realize a photonic RF receiver without any high-speed electronic components.

In a conventional super-heterodyne RF receiver architecture a local oscillator (LO) and mixer are used to down-convert the signal to IF frequencies. Baseband information is subsequently extracted from the IF signal in a detector/demodulator. Alternatively, in a direct-conversion (homodyne) radio receiver, baseband information is obtained by mixing the received signal and the LO without using an IF frequency [6]. In addition to such approaches, self-heterodyne techniques have been proposed to reduce the number of components as well as size, weight, and power consumption in high-carrier frequency (mm-wave), short distance, applications [7]. In a self-heterodyne transmission system the transmitter broadcasts a RF modulated signal *and* the local carrier so the IF signal can be down-converted by mixing the received carrier and modulated signal in a nonlinear device called a self-mixer. The receiver power consumption, phase noise, and complexity are reduced as a result of eliminating the conventional LO and mixer.

Although such an approach suffers from reduced power efficiency, it has been shown that it can lower overall cost and complexity in mm-wave local area networks and indoor wireless transmission systems.

Our photonic self-homodyne architecture combines direct-conversion, self-heterodyning, and microdisk modulator technology, to directly extract baseband information from the received signal by self-mixing of the transmitted carrier and the sidebands in the optical domain. We show that the second-order nonlinearity in the transfer function of a LiNbO₃ microdisk optical modulator when biased at its minimum transmission point may be used to realize the self-mixing process. Receiver operation is demonstrated experimentally by demodulating digital data from a 14.6 GHz RF carrier frequency.

II. Self-homodyne photonic RF receiver

A photonic self-homodyne RF-receiver replaces the function of a single-ended diode or FET mixer in a transmitted carrier wireless link with a sensitive optical modulator that performs down-conversion in the optical domain. In this approach the nonlinear dependence of the modulator's transmitted optical power (P_{ot}) on applied RF voltage (V_{RF}) is the source of nonlinearity in the system. Fig. 1 illustrates the photonic self-homodyne RF receiver architecture. The received RF signal contains both sidebands and the center frequency (transmitted-carrier double-sideband modulation format) and is fed to an optical modulator biased at its nonlinear operating point. The carrier and sidebands are mixed through the second-order nonlinearity ($P_{ot} \propto V_{RF}^2$), hence the optical output

intensity spectrum contains the baseband and high-frequency products around the second-harmonic of the carrier frequency. A photoreceiver with a bandwidth matched to the baseband signal generates the baseband photocurrent (i_p) and automatically filters out the high-frequency components. The bandwidth of all electronic circuitry used in the system is no greater than that of the baseband signal.

The electro-optic transfer function of an optical intensity modulator $P_{ot}(V_{RF})$ can be expanded around $V_{RF} = 0$ to give

$$P_{ot} = P_o^{(0)} + P_o^{(1)} + P_o^{(2)} + \dots = N_0 + N_1 V_{RF} + \frac{N_2}{2} V_{RF}^2 + \dots \quad (1)$$

Here, N_i ($i > 0$) is the i th Taylor expansion coefficient of $P_{ot}(V_{RF})$ at $V_{RF} = 0$ and N_0 is the transmitted optical power at $V_{RF} = 0$. At a fixed wavelength the magnitude of N_i depends on modulator properties and the chosen bias point. The first-order term in equation (1) generates linear optical intensity modulation ($P_{ot} \propto V_{RF}$) while other terms contribute nonlinear frequency components. Usually, such nonlinearities are minimized in conventional direct detection (DD) optical communication links. If the RF voltage amplitude is small enough and the modulator is biased at its extreme transmission point (where $dP_{ot}/dV_{RF} = 0$) the second-order term $P_o^{(2)}$ dominates the behavior of the modulator and the transmitted optical power (P_{ot}) dependence on voltage around $V_{RF} = 0$ will be similar to an ideal square-law mixer with

$$P_{ot} \approx N_0 + \frac{N_2}{2} V_{RF}^2 \quad (2)$$

If the baseband is a pure sinusoidal signal, the received RF voltage can be written as:

$$V_{RF} = V_0 (1 + m \cos(\omega_b t)) \cos(\omega_{RF} t) \quad (3)$$

where m is the RF modulation index, ω_b is the baseband frequency and $\omega_{RF}=2\pi f_{RF}$ is the RF carrier frequency. The second-order term can be written as

$$P_o^{(2)} = \frac{N_2}{2} \times V_{RF}^2 = \frac{N_2}{2} V_0^2 (1 + m \cos(\omega_b t))^2 \cos^2(\omega_{RF} t) \quad (4)$$

Expanding the right-hand-side of (4) one obtains a DC term equal to $(N_2 V_0^2 / 4)(1 + m^2 / 2)$, high-frequency components centered around $2\omega_{RF}$ given by

$$\frac{N_2 V_0^2}{4} ((1 + m^2 / 2) \cos(2\omega_{RF} t) + (m^2 / 4) \cos^2(2\omega_b t) \cos(2\omega_{RF} t) + m \cos(\omega_b t) \cos(2\omega_{RF} t)) \quad (5)$$

and the two down-converted low-frequency terms at ω_b and $2\omega_b$ are given by

$$\frac{N_2 V_0^2 m^2}{8} \cos(2\omega_b t) + \frac{N_2 V_0^2}{2} m \cos(\omega_b t) \quad (6)$$

The total second-order modulated optical power is

$$P_{o,max}^{(2)} = (1 + m^2 + 2m) \frac{N_2}{2} V_0^2 \quad (7)$$

which is just the maximum amplitude in (4). The efficiency of this down-conversion process may be defined as the ratio between the amplitude of the optical power modulated at ω_b and $P_{o,max}^{(2)}$. This efficiency is limited by the generation of undesired frequency components at $2\omega_b$, $2\omega_{RF} \pm 2\omega_b$, and $2\omega_{RF} \pm \omega_b$ as well as the DC component. The linearity of the down-conversion is also an important parameter in receiver operation and is defined as the ratio of optical power modulated at ω_b and $2\omega_b$. Here we assume that the strength of the second-order nonlinearity dominates higher order terms in (1) so the generation of higher harmonics of the baseband ($3\omega_b$, $4\omega_b$, etc.) can be ignored. The down-conversion efficiency and its linearity are determined by the RF modulation index (m).

In Fig. 2 the down-conversion efficiency (a) and second-harmonic suppression ratio (b) are calculated against m . The second-harmonic baseband term ($2\omega_b$) can be suppressed relative to the baseband (ω_b) by employing a transmitted carrier RF modulation format ($m < 2$) and the down-conversion efficiency reaches its maximum value of 25% around $m = 1$. By choosing $m = 0.8$ an efficiency of about 25% and second-harmonic suppression of 7 dB optical (14 dB electrical, $P_e \propto i_p^2 \propto P_{ot}^{(2)}$) can be achieved. The sensitivity of a photonic RF receiver strongly depends on the magnitude of the second-order nonlinearity (N_2) in (1) and so is determined by the modulator sensitivity and the transfer function P_{ot} . Given that most wireless links only require a limited bandwidth around a high frequency carrier, a microdisk resonant optical modulator [8] is a suitable choice for this application since it has a large N_2 coefficient when biased at a maximum or minimum optical transmission of a high- Q whispering gallery (WG) resonance.

III. LiNbO₃ microdisk modulator

A. Optical resonator

The optical resonator is a z-cut LiNbO₃ microdisk that supports high $Q \geq 10^6$ traveling-wave WG resonances. A microprism is used to evanescently couple optical power into and out of the microdisk. Fig. 3(a) illustrates single and double prism optical coupling. In the single prism coupling method, one prism is used to couple light into and out of the microdisk so transmission dips at resonant wavelengths are generated as a result of interference between the WG resonance and the output. In the double prism

coupling method dips are replaced by peaks. For optical mixing applications, single prism coupling is preferred because at resonance (where N_2 is maximized) the noise generated by DC optical power (N_0) is minimized.

The optical transfer function of a single prism coupled microdisk modulator can be calculated using a general relation for coupling between an optical microresonator and a dielectric waveguide [11]. The transmitted optical power ratio ($T = P_{ot}/P_{o,in}$) is written as:

$$T = \frac{a^2 + |t|^2 - 2a|t|\cos(\pi kD)}{1 + a^2|t|^2 - 2a|t|\cos(\pi kD)} \quad (8)$$

where D is the microdisk diameter, k is the wave vector of the WG optical resonance, $a = \exp(-\alpha\pi D)$ is the inner circulation factor (α is the distributed internal loss factor) and t is the transmission coefficient. The optical coupling factor (κ) may be expressed as $(1 - |t|^2)^{1/2}$. It is important to notice that all these parameters except D are different for different WG resonances. Each resonance has a Lorentzian shape with full-width-half-maximum wavelength $\Delta\lambda_{FWHM}$ around its resonant wavelength λ_{res} and a loaded optical $Q = \lambda_{res}/\Delta\lambda_{FWHM}$ limited by κ and α . Loaded Q is estimated as [12]:

$$Q = \frac{\pi^2 n_{eo} D \sqrt{ta}}{(1 - ta)\lambda_{res}} \quad (9)$$

where $n_{eo} = 2.14$ is the unperturbed extraordinary refractive index of LiNbO₃. The resonant frequencies associated with each set of optical modes are equally spaced from each other by the optical free spectral range of the micodisk resonator ($\Delta\nu_{FSR} = c/\pi n_{eo}D$). Fig. 3(b) shows the typical transmission spectrum of a LiNbO₃ microdisk with single prism coupler. As may be seen, one resonance is critically coupled so the transmitted optical power goes to zero on resonance. Critical coupling is equivalent to $N_0 = 0$ (at

$\lambda_{laser} = \lambda_{res}$) and is an ideal condition for self-homodyne photonic mixing because the DC optical noise is limited by the DC component generated by the mixing process, $(N_2 V_0^2/4)(1 + m^2/2)$.

B. RF ring resonator

We use a metal ring RF resonator with the same diameter as the microdisk to control the electric field in the LiNbO₃. The RF resonator is placed on top of the LiNbO₃ microdisk and is side coupled to a microstripline that is used to feed electromagnetic energy to the resonator. The fundamental RF resonant frequency (f_{RF}) of the loaded metal ring is designed to be equal to the optical free spectral range ($\Delta\nu_{FSR}$) [8,9]. Fig. 4(a) shows a photograph of the LiNbO₃ microdisk modulator with diameter $D = 3$ mm, thickness $h = 0.4$ mm, and $\Delta\nu_{FSR} = 14.6$ GHz. Fig. 4(b) is a photograph of the modulator arrangement showing the microdisk, the microprism, metal ring RF resonator, and the microstripline. The RF coupling coefficient is tuned by adjusting the distance, g , between the microring and the microstripline to maximize the E -field intensity at $f_{RF} = \Delta\nu_{FSR}$. The RF voltage amplitude seen by the optical mode is larger than the input voltage amplitude by a factor of G_v (the voltage gain factor) at resonance [10]. The ring resonator provides a standing wave E -field along the full photon path length around the disk and therefore may double the electro-optic interaction for each round trip compared to a semi-ring resonator that was previously used in a microdisk modulator [8].

C. Linear and nonlinear modulation

Typically, a microdisk modulator has a very high sensitivity within a limited bandwidth centered at frequencies equal to integral multiples of the $\Delta\nu_{FSR}$ [8]. The high

sensitivity of the modulator is a result of simultaneous RF and optical resonance. Typically, the modulation bandwidth is limited by the optical Q . Using a microdisk modulator with $\Delta\nu_{FSR} = 14.6$ GHz (Fig. 4) we have measured a signal-to-noise ratio of 12 dB at -67 dBm RF input power (corresponding to a sensitivity of -80 dBm).

We can use (5) to estimate the modulated optical power at any RF input voltage (V_{RF}) and optical input wavelength (λ_{laser}) knowing the relation between V_{RF} and k :

$$k(V_{RF}) = \frac{2\pi n_e(V_{RF})}{\lambda_{laser}} = \frac{2\pi[n_{eo} + \delta n_e(V_{RF})]}{\lambda_{laser}} \quad (10)$$

Here, $\delta n_e(V_{RF})$ is the electro-optically induced refractive index change given by

$$\delta n_e(V_{RF}) = \frac{1}{2} n_{eo}^3 r_{33} \frac{\beta_{EO} \beta_S G_V}{h} \times V_{RF} \quad (11)$$

where $\beta_S \sim 0.5$ is a correction factor that accounts for the sinusoidal spatial E -field distribution around the ring when its fundamental mode is excited, β_{EO} is an optical-mode-electric-field overlap correction factor, $r_{33} = 30.8 \times 10^{-12}$ m/V is the linear electro-optic coefficient of LiNbO₃ along the c -axis. By measuring the resonant wavelength shift $\Delta\lambda_{DC}$ (called DC shift) when 1 V is directly applied to the metal ring one may estimate β_{EO} .

In Fig. 5 the transmitted optical power (P_{ot}) for the modulator shown in Fig. 4 is simulated as a function of wavelength and input RF voltage amplitude. In our simulation the modulator parameters are chosen to be representative of the experimental values with $Q = 3.5 \times 10^6$ (corresponding to $\alpha = 0.0075$ cm⁻¹ and $\kappa_0 = 0.095$), $h = 400$ μ m, and $G_V = 6$. The optical input power is 50 μ W and $\lambda_{laser} \sim 1550$ nm. Fig. 5(a) shows P_{ot} as a function of wavelength at 0 V and 1 V DC applied to the ring resonator. For this modulator, the measured value of $\Delta\lambda_{DC} = 0.13$ pm/V corresponds to $\beta_{EO} = 0.53$. Fig. 5(b) shows P_{ot}

calculated as a function of input RF voltage (V_{RF}). The laser wavelength (λ_{laser}) is tuned to $\lambda_{res} + (\Delta\lambda_{FWHM}/4)$ where N_1 is maximized at $V_{RF} = 0$. This is the condition for optimized linear optical intensity modulation using a microdisk modulator. The dashed and dotted lines are generated as the first (N_1) and second (N_2) Taylor coefficients in an expansion of the optical transfer function (solid line). In Fig. 5(c) the laser wavelength is tuned to an optical resonance of the microdisk ($\lambda_{res} = \lambda_{laser}$) so in the absence of an external voltage ($V_{RF} = 0$) the transmitted optical power is minimized. At this bias point N_1 is zero and N_2 is maximized so the modulator is operating in the extreme nonlinear regime. The sensitivity of the modulator can be quantified by a voltage amplitude V_{HMM} that modulates half of the optical mode power ($P_{o,mod} = P_{o,in} - P_{o,min}$). V_{HMM} is determined by the optical Q , h , r_{33} , and G_v . If $V_{RF} < 0.25V_{HMM}$ (small signal operating regime) the microdisk modulator is effectively operating as a square law optical intensity modulator ($N_i \sim 0$, $i > 2$) as explained in section II. As may be seen in (6), the baseband modulated optical power is equal to $mN_2V_0^2/2$. N_2 is the critical parameter for down-conversion and can be calculated using (5), (7) and (8) (N_2 is directly proportional to V_{HMM} and optical input power). Fig. 5(c) shows that $V_{HMM} = 0.48$ V and optical input power of 50 μ W results in $N_2 = 0.037$ mW/V².

IV. DOWN-CONVERSION IN MICRODISK MODULATOR

A. Single tone down-conversion

In our initial experiments we use a single tone baseband signal to study the effect of RF modulation index (m) and RF power on down-conversion efficiency and its linearity. Fig. 6 is a schematic diagram of the experimental arrangement. The modulator uses a 400 μm thick LiNbO₃ microdisk of 3 mm diameter and a free spectral range of $\Delta\nu_{\text{FSR}} = 14.6$ GHz. The laser source is a tunable single mode laser with 0.05 pm wavelength resolution and a linewidth of less than 0.5 MHz. The laser wavelength is always tuned to the minimum of the chosen transmission dip to maximize the second-order nonlinear modulation strength (N_2). The RF signal is a 10 MHz single tone baseband signal mixed with a 14.6 GHz RF-carrier in a double-balanced RF-mixer. By DC-biasing the IF port of the mixer we can control the modulation index (m) and magnitude of the transmitted power at the carrier frequency. The RF signal is fed to the microdisk modulator through a bandpass RF filter with 1 GHz bandwidth around 14.5 GHz, to make sure that all of the nonlinear products generated in the RF components are filtered out. The optical output is detected in an amplified photodetector with a bandwidth of 150 MHz and responsivity of 3 mV/ μW .

Fig. 7(a) shows the variation of the down-converted optical power at 10 MHz as a function of the modulation m and for three resonances with different quality factors. The modulation index is tuned to the desired values by changing the DC bias applied to the mixer. The total received RF power is about -15 dBm that corresponds to $V_0 = 0.05$ V (3). The V_{HMM} is around 0.8 V for the optical resonance used, so $V_0 < 0.25 V_{\text{HMM}}$ guarantees device operation in the small-signal regime (section III). As may be seen in Fig. 7(a), down-conversion efficiency is maximized around $m = 0.8$, in very good

agreement with the simulated curve for an ideal square law mixer (Fig. 2(a)). Also, as anticipated, the amount of down-converted power increases as we increase the optical Q (a larger Q results in a larger V_{HMM} and therefore a larger N_2). Fig. 7(b) shows the down-converted optical power against the total RF input power when $m = 0.8$. The black circles are the experimental data and the white circles and dashed line are the simulated data. The inset shows the optical resonance selected for nonlinear modulation. The black arrow indicates the location of the laser wavelength, λ_{laser} . The optical resonance has $Q = 2.7 \times 10^6$ and a N_2 coefficient of 0.023 mW/V^2 ($V_{HMM} = 0.7 \text{ V}$). The simulated data in Fig. 7(b) are calculated using $mN_2V_0^2/2$ and knowing that the total average RF power of a single tone modulated RF carrier (3) is given by $P_{RF} = V_0^2(1+m^2/2)/100$ (this can be easily calculated by integrating the average power of the RF signal in (3)). To evaluate the linearity of the down-conversion process we have measured the detected power at the second and third harmonic of the baseband signal (20 MHz and 30 MHz respectively). In a perfect square law modulator the third harmonic should be absent but the chosen optical resonance doesn't have an ideal symmetric shape and so generates odd harmonics. Fig. 7(c) shows the harmonic suppression ratio against m . As predicted (Fig. 2(b)) the suppression ratio decreases when we increase m . At $m = 0.8$ the second-harmonic suppression ratio is about 17 dB (electrical).

B. Down-conversion of digital data

We have simulated the signal flow in the photonic RF receiver to show the details of the down-conversion process in both the frequency and time domain. Fig. 8(a) shows the

modulated transfer function when the laser emission wavelength (λ_{laser}) is centered at one of the microdisk optical resonant wavelengths and the modulator is fed by the data modulated RF carrier. $\Delta\lambda_{RF}$ is the amplitude of the resonant wavelength oscillation due to the applied RF voltage (the oscillation amplitude is exaggerated to show the down-conversion mechanism). In the simulation, the RF carrier frequency $f_{RF} = 10$ GHz is modulated by a 62.5 Mb/s non-return-to-zero (NRZ) data stream with a modulation index of $m = 0.8$. Fig 8(b) shows the RF spectrum of the transmitted-carrier input signal and the inset shows the original data stream in a 640 ns time interval. Fig 8(c) shows the calculated spectrum of the optical output intensity. Nonlinear modulation generates the baseband signal and high-frequency components around 20 GHz. The photodetector bandwidth of 150 MHz (dashed line) filters out the high-frequency components and only the baseband is converted to an electric signal. The inset shows the detected data stream again in a 640 ns time interval.

For experimental demonstration of data transmission we use the arrangement in Fig. 6 but replace the signal generator with a NRZ pattern generator and the photodetector with a digital photoreceiver. The photoreceiver has a -3 dB frequency bandwidth of 120 MHz and a sensitivity of -34.5 dBm. Fig. 9(a) shows the measured frequency spectrum of the input RF signal and the down-converted signal after detection. The carrier frequency is 14.62 GHz and the baseband data is a 10 Mb/s NRZ 2^7-1 pseudo-random bit stream (PRBS). Fig. 9(b) shows the measured bit error ratio (BER) against the total RF input power. The received RF power is defined as the measured RF power within 10 MHz bandwidth centered around 14.6 GHz. The left inset shows the spectrum of the optical

resonance with $Q = 2 \times 10^6$. The inset on the right shows the input and down-converted data in the time domain. In Fig. 9(c) the measured eye diagrams at 10 Mb/s, 50 Mb/s and 100 Mb/s at -15 dBm received RF power are shown. In this particular case the maximum data rate is limited by the optical Q to approximately 100 Mb/s.

We note that the detected down-converted signal can be increased by reducing the disk thickness (h) and employing a high- Q RF ring resonator (both these factors lead to a larger N_2 coefficient). We can also reduce the signal-to-noise in the photonic receiver by employing a bandpass optical filter after the microdisk modulator. A filter with a bandwidth less than $4f_{RF}$ can eliminate high frequency optical components around $2f_{RF}$ given by (5) and therefore reduce the noise generated by the optical power at these frequencies in the slow-speed photoreceiver.

The microdisk modulator and the photonic self-homodyne architecture have the potential to be incorporated into a photonic integrated circuit by using alternative electro-optic materials (such as polymers and compound semiconductors). Reducing the disk diameter will extend the carrier frequency into mm-wave regime so that this receiver architecture has potential to be used in future indoor mm-wave wireless systems.

V. CONCLUSION

A novel self-homodyne photonic RF receiver based on a microdisk modulator has been described. Down-conversion occurs in the optical domain through *nonlinear*

modulation, thereby eliminating the need for an RF local oscillator and mixer. Experimental verification of the receiver architecture has been achieved by measuring BER and eye-diagrams using signals down-converted from a NRZ digital data modulated transmitted carrier RF signal with $f_{RF} = 14.6$ GHz carrier frequency.

Acknowledgement

This work is sponsored by *NASA* and *DARPA*.

References

- [1] B. Vidal, V. Polo, J. L. Corral, and J. Marti, "Efficient architecture for WDM photonic microwave filters," *IEEE Photon. Technol. Lett.*, vol. 16, pp. 257-259, Jan. 2004.
- [2] P. O. Hedekvist, B.-E. Olsson, and A. Wiberg, "Microwave harmonic frequency generation utilizing the properties of an optical phase modulator," *J. Lightwave Technol.*, vol. 22, pp. 882-886, March 2004.
- [3] A. Hirata, M. Harada, and T. Nagatsuma, "120-GHz wireless link using photonic techniques for generation, modulation, and emission of millimeter-wave signals," *J. Lightwave Technol.*, vol. 21, pp. 2145-2153, Oct. 2003.
- [4] G. K. Gopalakrishnan, W. K. Burns, and Catherine H. Bulmer, "Microwave-optical mixing in LiNbO₃ modulators," *IEEE Trans. Microwave Theory and Tech.*, vol. 41, pp. 2383-2391, Dec 1993.
- [5] M. Tsuchiya and T. Hoshida, "Nonlinear photodetection scheme and its system applications to fiber-optic millimeter-wave wireless down-links," *IEEE Trans. Microwave Theory and Tech.*, vol. 47, pp. 1342-1350, July 1999.
- [6] A. A. Abidi, "Direct-conversion radio transceivers for digital communications," *IEEE J. Solid-State Circuits*, vol. 30, pp 1399-1410, Dec 1995.
- [7] Y. Shoji, K. Hamaguchi, H. Ogawa, "Millimeter-wave remote self-heterodyne system for extremely stable and low cost broad-band signal transmission", *IEEE Trans. Microwave. Theory and Tech*, vol. 50, pp1458-1468, June 2002.
- [8] D. A. Cohen, M. Hossein-Zadeh, and A. F. J. Levi, "High-Q microphotonic electro-optic modulator," *Solid-State Electronics*, vol. 45, pp.1577-1589, 2001.
- [9] M. Hossein-Zadeh, A. F. J. Levi, "A new electrode design for microdisk optical modulator," *CLEO Technical digest 2003*, CTuW3, June 2003.
- [10] M. Hossein-Zadeh, A. F. J. Levi, "Mb/s data transmission over a RF fiber optic link using a LiNbO₃ microdisk optical modulator," *Solid-State Electronics*, vol. 46, pp. 2173-2178, 2002.
- [11] A. Yariv, "Universal relations for coupling of optical power between microresonators and dielectric wave guides," *Electronic letters*, vol 41, pp. 321-322, 2000.
- [12] "Laser Electronics", Joseph Verdeyen, third edition 1995.

Figure captions:

Fig. 1. Schematic diagram of the photonic self-homodyne RF receiver. The transmitted carrier RF signal is received by the antenna and is directly fed to a square-law optical intensity modulator. Through nonlinear optical modulation the optical output intensity spectrum contains the baseband and high frequency components that are filtered out by the response of the low-speed photodetector.

Fig. 2. (a) Calculated down-conversion $(P_{o,\omega_b}/P_{o,\max}^{(2)})$ efficiency versus RF modulation index (m). (b) Second-harmonic suppression ratio against m . The electrical and optical suppression ratios are related through $P_{e,\omega_b}/P_{e,2\omega_b} = (i_{\omega_b}/i_{2\omega_b})^2 \propto (P_{o,\omega_b}/P_{o,2\omega_b})^2$

Fig. 3. (a) Single prism optical coupling versus double prism coupling scheme. In single prism method dips are generated as a result of interference between the beam coupled out of the microdisk. (b) Typical optical output spectrum of the single prism coupled microdisk resonator. One of the modes is critically coupled (zero transmission).

Fig. 4. (a) Photograph of the LiNbO₃ microdisk modulator. (b) A close up view of the modulator showing the microstripline, LiNbO₃ microdisk, microprism, microring RF resonator and the output fiber.

Fig. 5. (a) Calculated transmitted optical power in the vicinity of a resonant mode at 0 and 1 V applied DC voltage for a 0.4 mm thick disk with a $\beta_{EO} = 1.9$, $\kappa = 0.095$, and $\alpha = 0.0075 \text{ cm}^{-1}$. (b) Calculated optical output intensity of the microdisk modulator as a function of RF input voltage ($G_v = 6$). The dashed and dotted lines are generated as the first (N_1) and second (N_2) Taylor coefficients in an expansion of the optical transfer function (solid line). The laser wavelength is biased to the linear operation regime where at $V_{RF} = 0$, N_1 is maximum and $N_2 = 0$. (c) Calculated optical output intensity of the microdisk modulator biased at the extreme nonlinear operation regime ($\lambda_{res} = \lambda_{laser}$) versus RF voltage.

Fig. 6. Schematic diagram of the experimental arrangement used for photonic RF down-conversion measurements. The RF modulation index (m) is tuned using the DC bias on the mixer. The laser is a tunable single mode laser with a resolution of 0.1 pm and linewidth of less than 0.5 MHz. The RF filter eliminates any low frequency component generated due to nonlinearities in RF devices. The local oscillator frequency is 14.6 GHz that is equal to the optical free spectral range of the microdisk modulator.

Fig. 7. (a) Measured baseband modulated (10 MHz) optical output power against m for three optical modes with different optical quality factors. (b) The measured and calculated baseband modulated optical power versus total RF input power. The inset shows the optical spectrum of the WG resonance chosen for down-conversion ($Q = 2.7 \times 10^6$, $N_2 = 2.23 \times 10^{-2} \text{ mW/V}^2$). (c) Measured second and third Harmonic suppression ratios (electrical) against m .

Fig. 8. Simulated signal flow in a self-homodyne RF receiver. (a) Modulated optical transfer function when the laser emission wavelength (λ_{laser}) is centered at one of the microdisk optical resonant wavelengths and the modulator is fed by the data modulated RF carrier. The RF carrier frequency is 10 GHz and is modulated by a 62.5 Mb/s data stream with a modulation index of $m = 0.8$. The modulation amplitude is exaggerated to show the down-conversion mechanism. (b) Spectrum of the transmitted-carrier RF input signal. The inset shows the original data stream in a short time interval (640 ns). (c) Calculated spectrum of the optical output intensity. Nonlinear modulation generates the baseband signal and high-frequency components around 20 GHz. The photodetector bandwidth of 0.1 GHz (dashed line) filters out the high-frequency components and only the baseband is converted to an electric signal. The inset shows the detected data stream again in a 640 ns time interval

Fig. 9. Measurement results of photonic data down-conversion in LiNbO₃ microdisk modulator. (a) The frequency spectrum of the input RF signal and down-converted signal. The RF carrier frequency is 14.6 GHz and it is modulated by a 10 Mb/s 2^7 -1 NRZ PRBS bit stream. (b) The BER sensitivity of the photonic RF receiver. The RF power is the measured RF power within 10 MHz bandwidth centered around 14.6 GHz. The right inset shows the input and detected data in time domain. The left inset shows the optical spectrum of the selected WG resonance. (c) Measured eye diagrams at 10 Mb/s, 50 Mb/s and 100 Mb/s at -15 dBm received RF power.

Figure 1

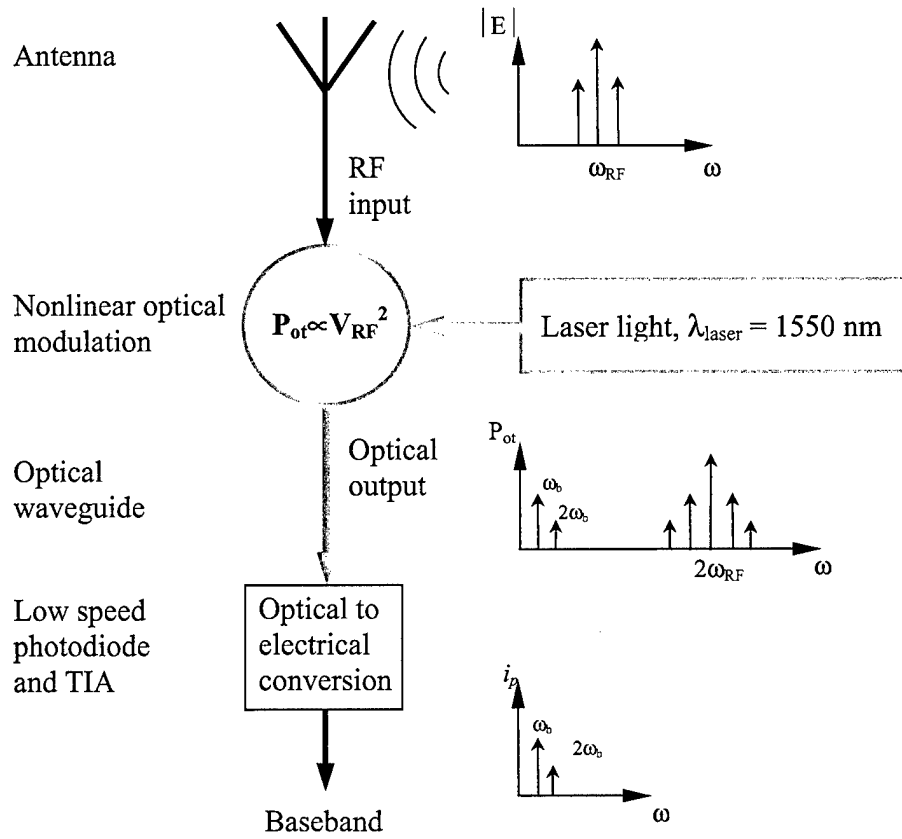


Figure 2

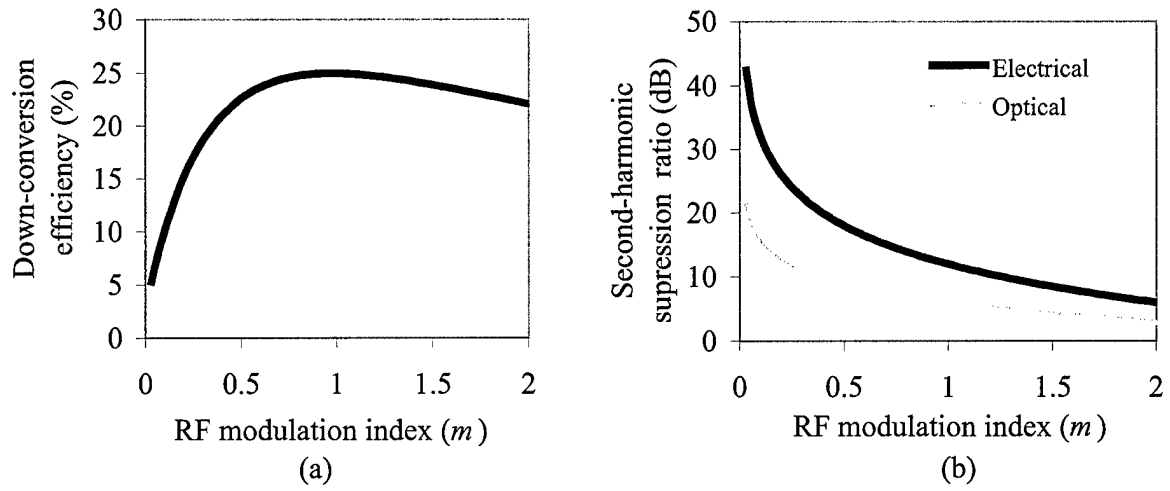


Figure 3

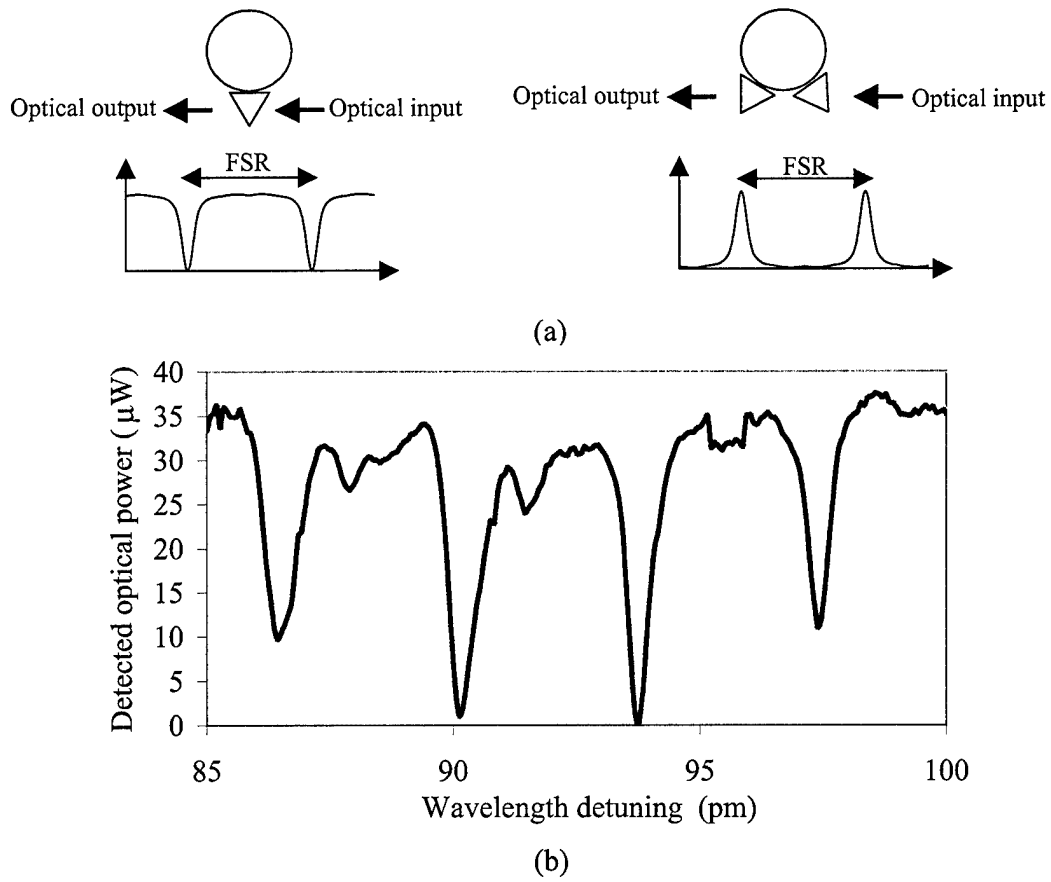


Figure 4

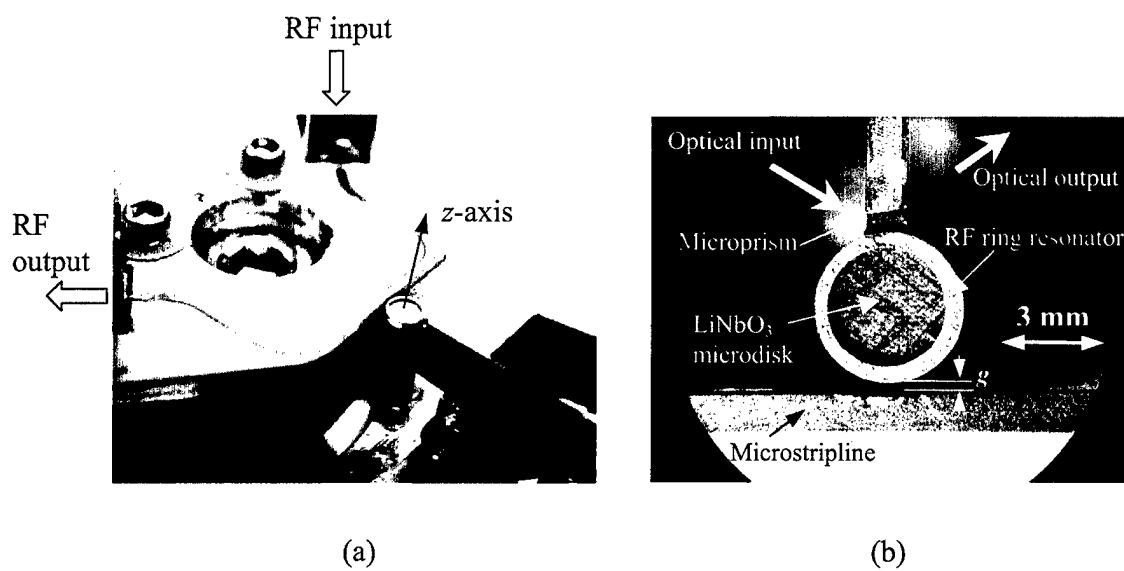


Figure 5

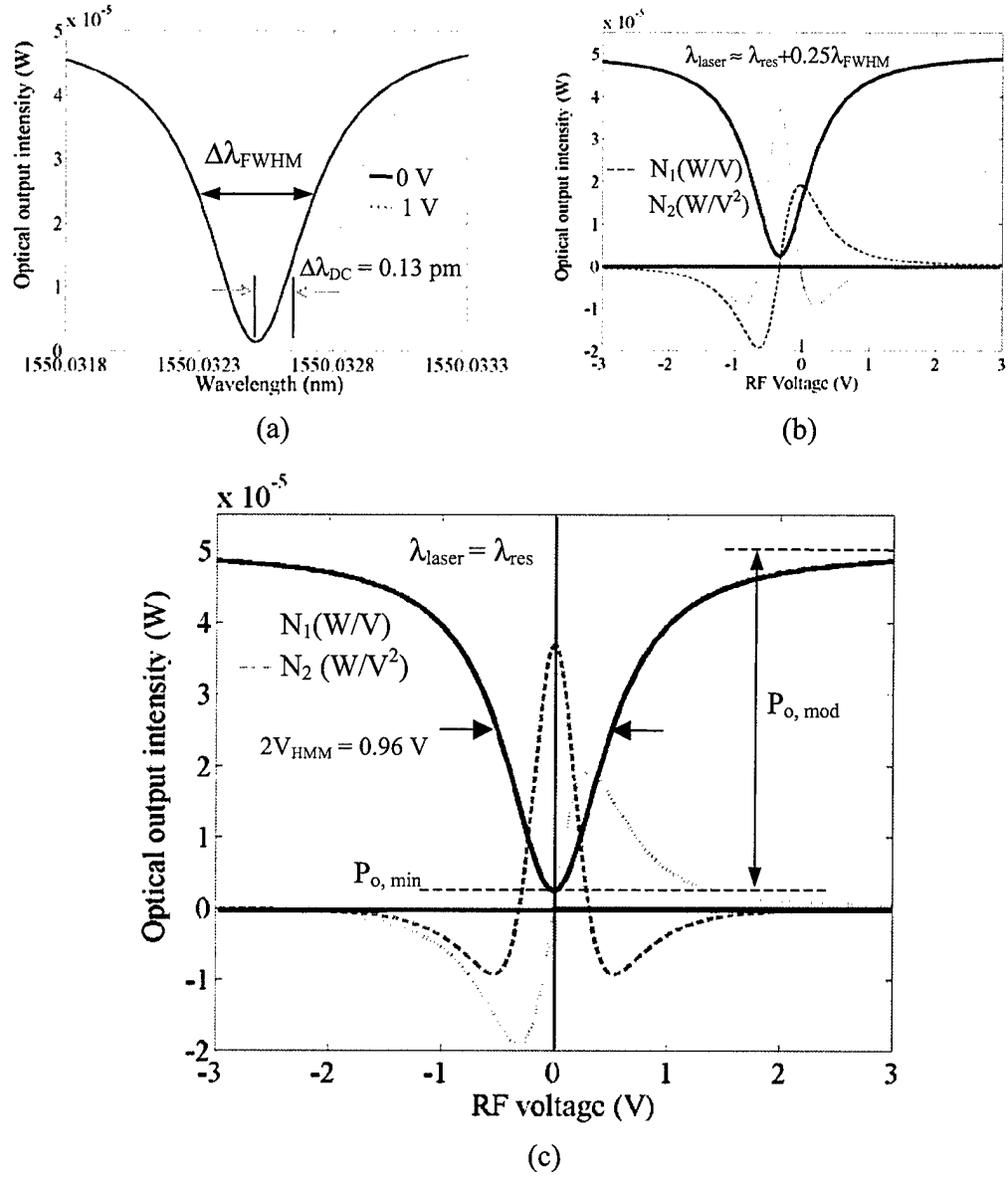


Figure 6

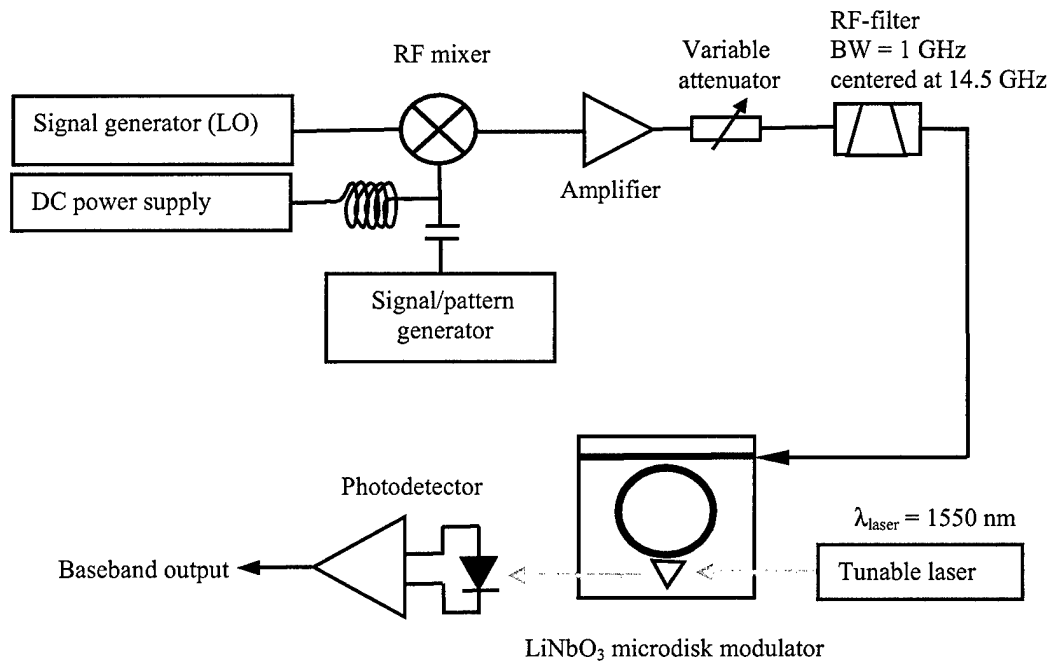


Figure 7

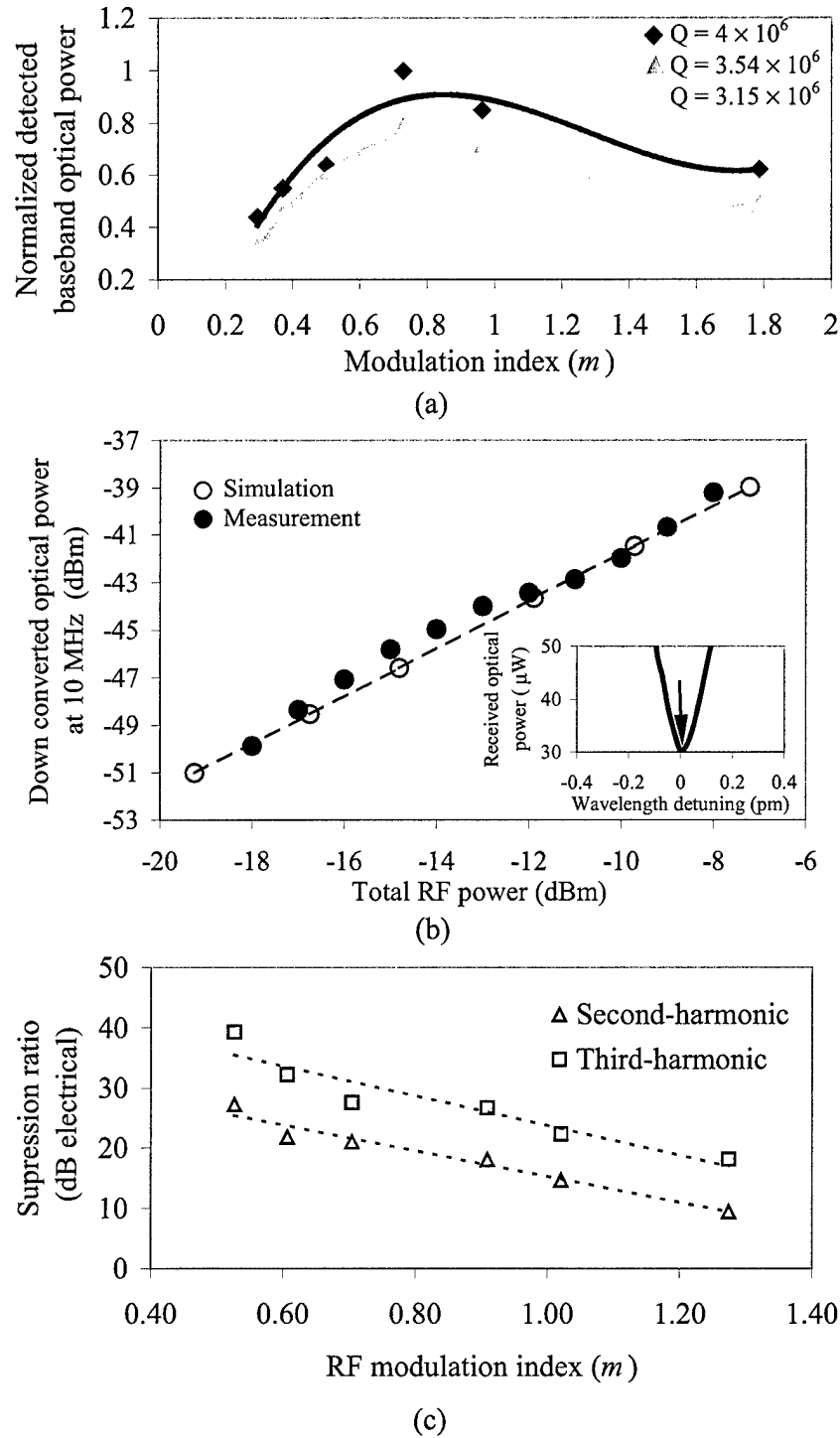
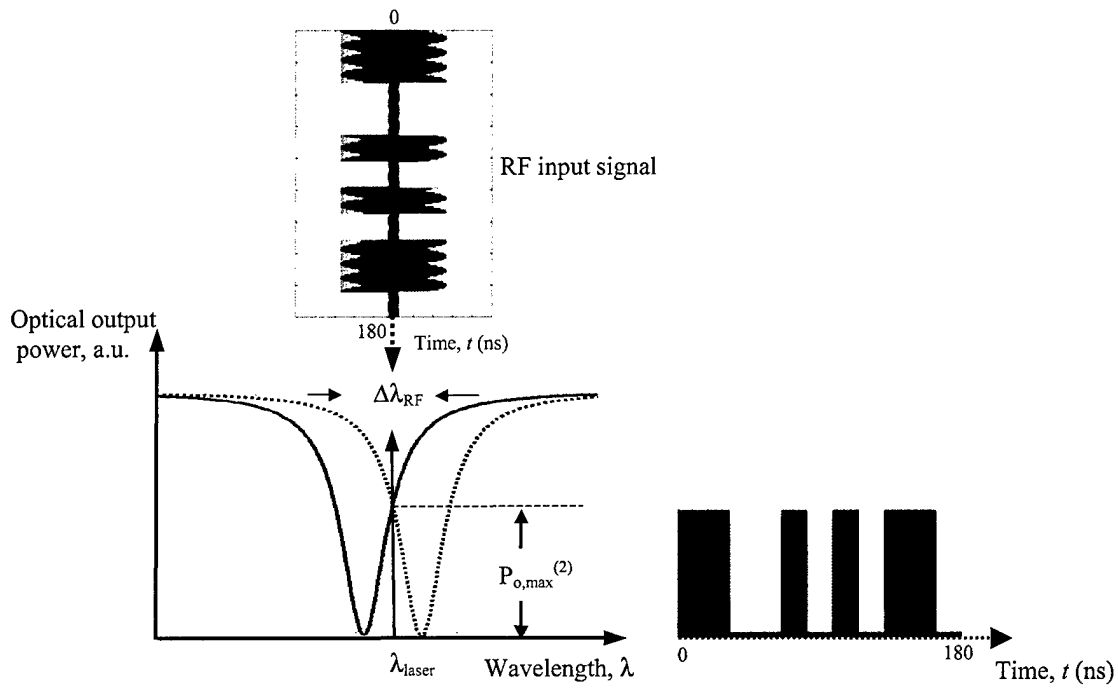
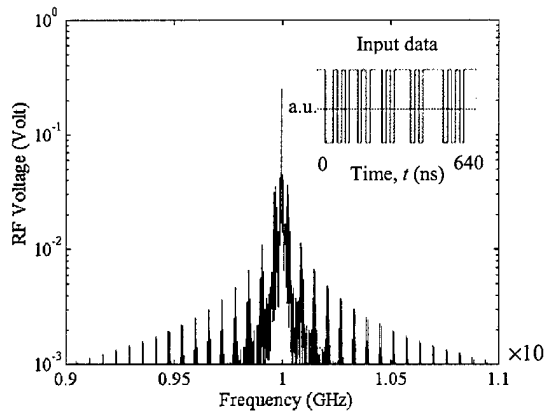


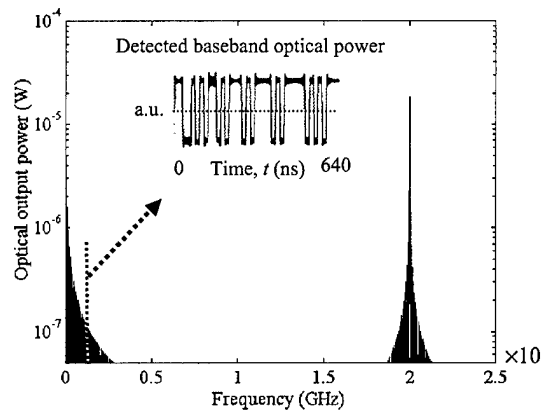
Figure 8



(a)

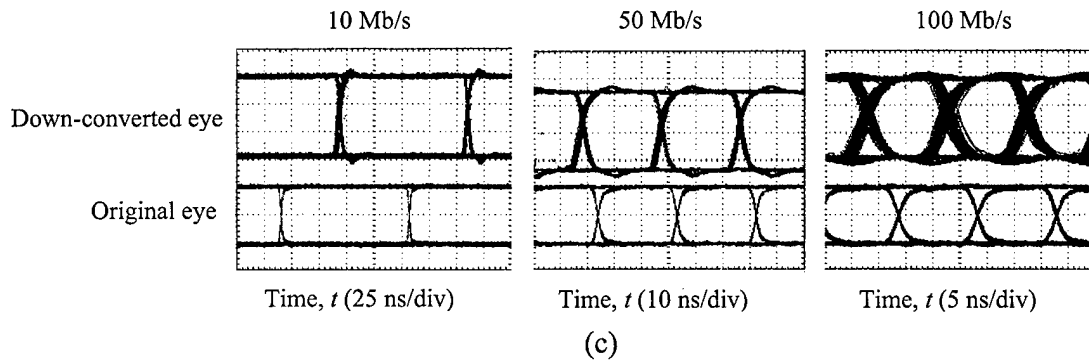
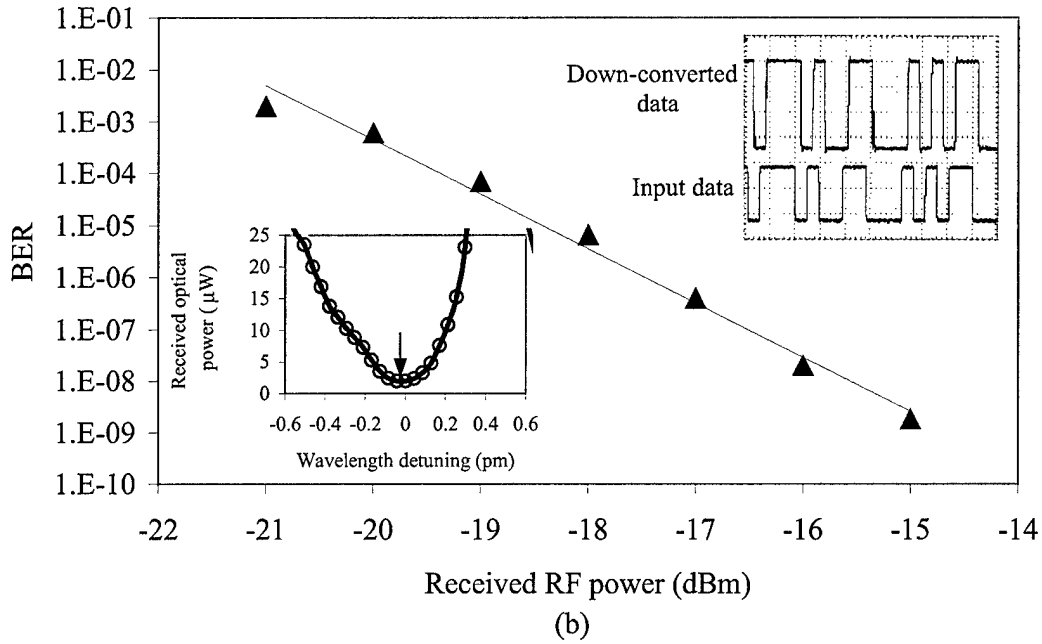
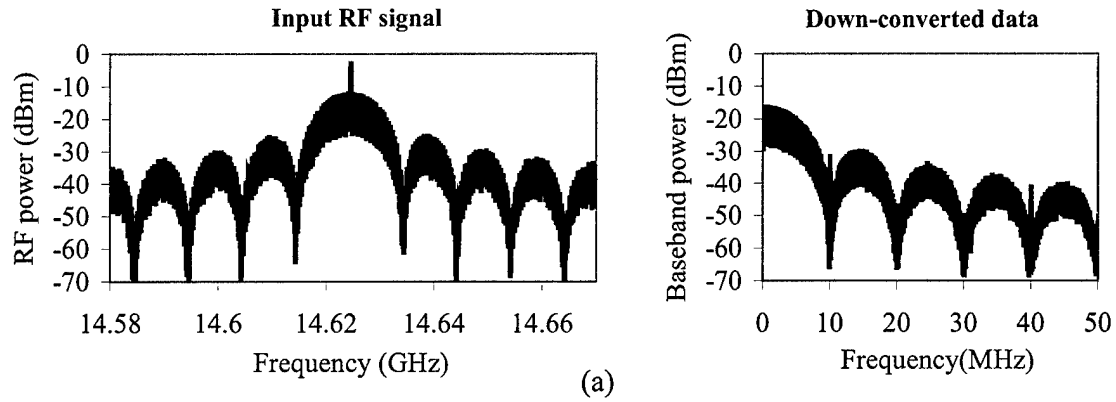


(b)



(c)

Figure 9





PERGAMON

Available online at www.sciencedirect.com

SCIENCE @ DIRECT®

Solid-State Electronics 46 (2002) 2173–2178

SOLID-STATE
ELECTRONICS

www.elsevier.com/locate/sse

Mb/s data transmission over a RF fiber-optic link using a LiNbO_3 microdisk modulator

M. Hossein-Zadeh, A.F.J. Levi *

Department of Electrical Engineering, University of Southern California, Denny Research, Building 118, Los Angeles, CA 90089-1111, USA

Received 17 February 2002; received in revised form 13 April 2002; accepted 16 April 2002

Abstract

For the first time, we demonstrate data transmission over a radio frequency (RF) fiber-optic link using a LiNbO_3 microdisk configured to modulate an optical carrier. Initial experimental results demonstrate high-quality data transmission up to 100 Mb/s on a 8.7 GHz RF carrier.

© 2002 Elsevier Science Ltd. All rights reserved.

Keywords: LiNbO_3 microdisk resonator; Optical modulator; Optical communication

1. Introduction

Recently a new microphotonic radio frequency (RF) receiver with direct electrical-to-optical conversion was proposed [1]. The receiver uses an electro-optic disk to modulate an optical carrier with the received RF signal. The modulator is configured as a traveling-wave resonator that can support very high- Q TE-polarized optical whispering-gallery modes (WGMs). The modulating electric field is provided by a separate RF-resonator whose frequency is tuned to the free-spectral-range (FSR) of the optical modes in such a way that it is in simultaneous resonance with the traveling optical waves inside the disk. It has been shown [2] that, unlike Mach-Zehnder designs, the microdisk can perform efficient optical modulation without use of a reference arm to convert phase to amplitude modulation. Spatial confinement of the photon field, long photon lifetime inside the optical-resonator, and voltage gain provided by the RF-resonator can dramatically enhance RF-photon in-

teraction (via the electro-optic effect) resulting in power-efficient RF-to-optical conversion in a small volume.

Previous work has focused on demonstration of single-frequency microwave and mm-wave modulation [2]. In this paper we report the first experimental results of Mb/s data transmission over a RF fiber-optic link using a microdisk modulator.

2. Experimental results

The disk employed is z-cut LiNbO_3 of radius $R = 2.56$ mm and thickness $t = 400$ μm . A microprism couples laser light into the microdisk and another prism is used to couple light out. A lens focuses light from a frequency stabilized tunable laser into the input-prism and a cleaved fiber at the output-prism collects and spatially filters the optical output. All components are mounted on a planar substrate. Fig. 1(a) shows a photograph of the experimental arrangement and Fig. 1(b) is a schematic diagram of the RF-optical link.

A half-ring metal electrode RF-resonator tuned to match the optical FSR = 8.68 GHz is placed on top of the disk to provide the resonant RF electric field. A RF carrier is modulated by a non-return-to-zero pseudo-random bit-stream (NRZ 2^7 -1 PRBS) using a RF mixer and the signal feed is side-coupled to the resonator

* Corresponding author. Tel.: +1-213-740-7318; fax: +1-213-740-9280.

E-mail address: alevi@usc.edu (A.F.J. Levi).

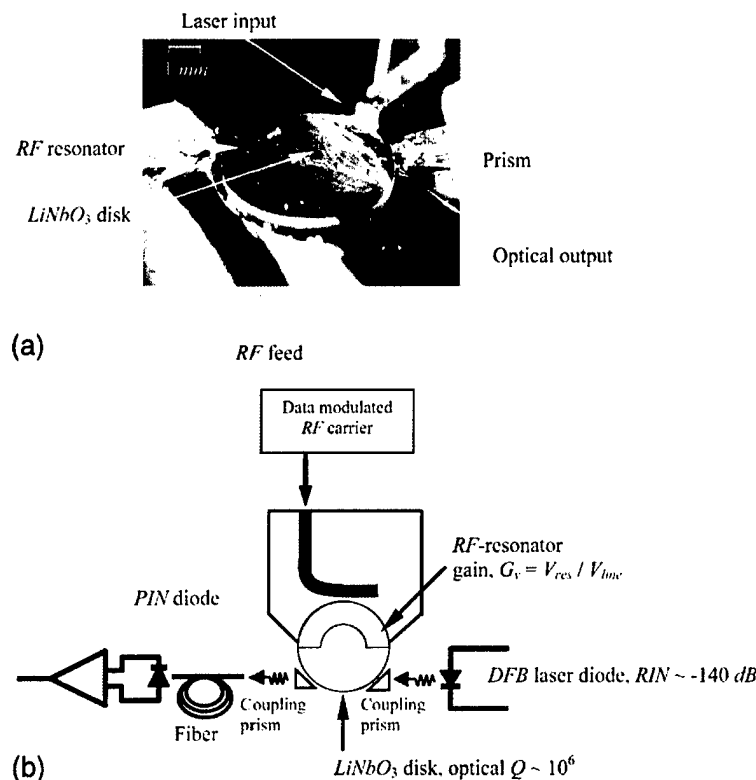


Fig. 1. (a) Photograph of the experimental arrangement. (b) Schematic diagram showing different parts of the RF optical-link.

electrode. The modulated optical carrier at frequency $f = 194$ THz (wavelength $\lambda = 1550$ nm) is transmitted through several meters of fiber and a PIN diode is used to detect and mix the optical signal. The integrity of demodulated data is measured using a bit error ratio (BER) tester and a digital oscilloscope. The laser wavelength is tuned close to one of the high- Q TE-modes of the disk where optical modulation is maximized. The bandwidth of a typical optical-mode is about 150 MHz, corresponding to an optical $Q = 1.3 \times 10^6$, and this limits the data transmission rate to < 200 Mb/s.

Modulated RF power is measured within a 150 MHz bandwidth centered at 8.68 GHz RF-carrier frequency. Fig. 2(a) shows the measured phase-margin of the detected output at 10 Mb/s (NRZ 2⁷-1 PRBS) data rate for the indicated modulated RF-power. The inset is representative of the corresponding input and output eye-diagram. Fig. 2(b) shows the RF signal spectrum before (left) and after (right) optical modulation. Fig. 2(c) shows the measured sensitivity of BER as a function of RF power. The optical output power for all of these measurements is in the range 18–27 μ W and the laser wavelength is tuned close to the maximum slope of the optical mode.

Fig. 3 shows input and demodulated output eye-diagrams transmitted over the RF fiber-optic link at (a)

50 Mb/s and (b) 100 Mb/s NRZ 2⁷-1 PRBS data rates. The critical factors for high-quality data transmission are the purity and Q -factor of the optical mode, the magnitude of the rising or falling slope of the optical mode in the vicinity of the laser wavelength, and the optical output power from the disk. By tuning the laser wavelength and RF carrier frequency it is possible to optimize the modulation quality and efficiency. Due to the presence of high- Q ($1-3 \times 10^6$) optical modes, the sensitivity of modulation quality and efficiency to the mode slope, wavelength stability of the laser is also important. To ensure stable, high-quality, data transmission the wavelength stability should be < 0.1 pm.

3. Noise and BER performance

3.1. The model

To analyze performance of the microdisk modulator we use a model based on the fact that the transmissivity of a high- Q microdisk optical resonator in the frequency domain is a series of Lorentzian line-shapes, centered at the resonant frequencies (f_m) of the disk. For each mode the FWHM $= f_m/Q$ and $f_m = mc/2\pi Rn_c$ where R is the

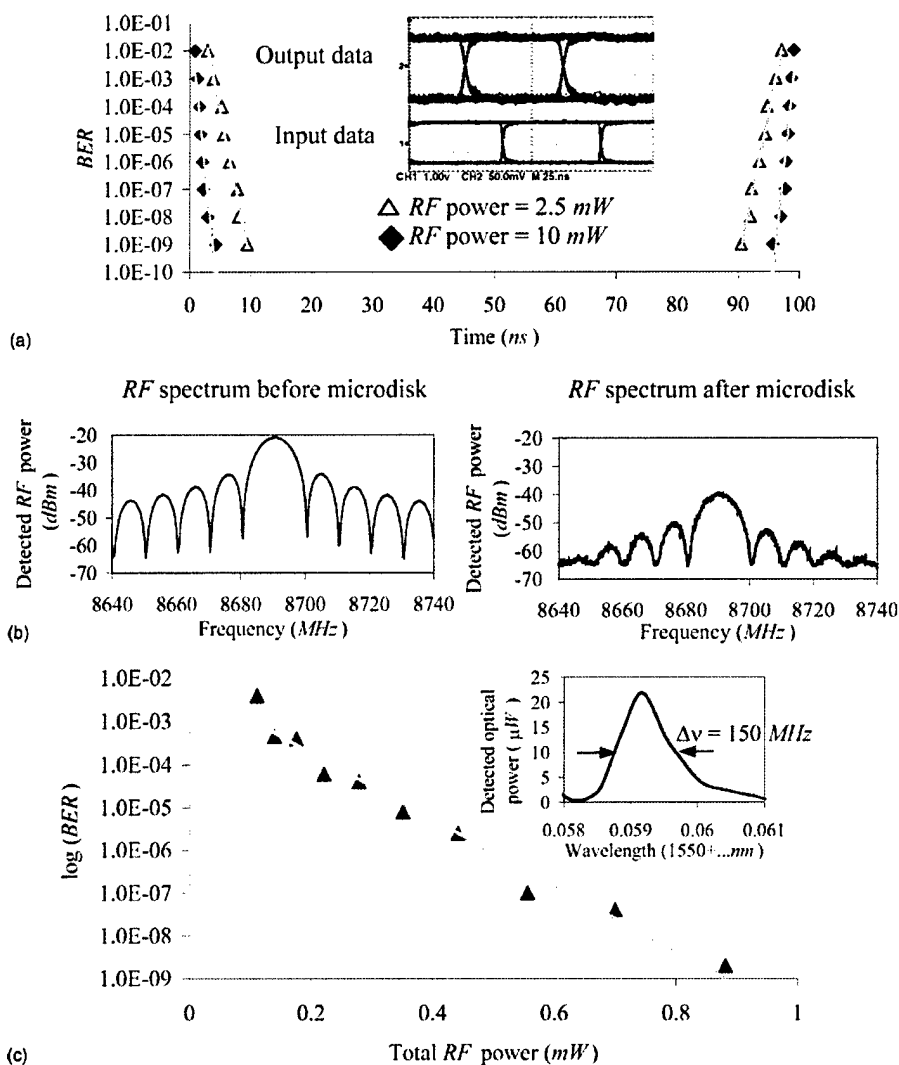


Fig. 2. (a) Measured phase margin of the output at 10 Mb/s (NRZ 2^7-1 PRBS) for 10 and 2.5 mW modulating RF power. The inset shows representative input and output eye-diagrams. (b) Measured RF signal spectrum before and after microdisk modulator using 2.5 mW RF power. (c) Measured sensitivity of BER to modulating RF power (measured RF power within 150 MHz bandwidth centered at 8.68 GHz). The inset is the detected optical output power against input laser wavelength.

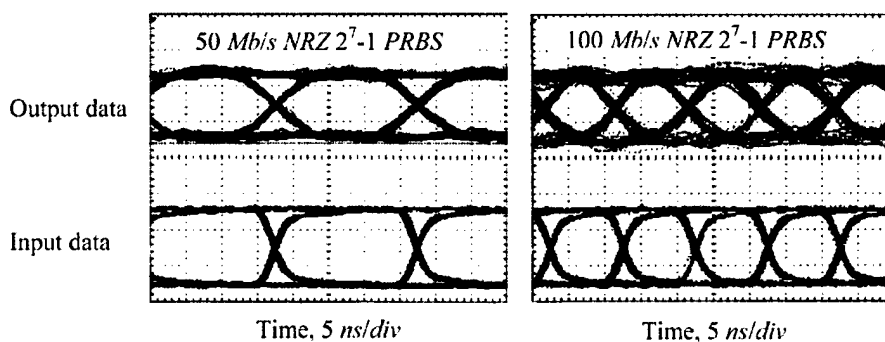


Fig. 3. Optical output eye-diagrams at 50 and 100 Mb/s (NRZ 2^7-1 PRBS). The modulating RF power is 40 and 60 mW respectively.

disk radius, n_e the extraordinary refractive index of LiNbO_3 , c is the speed of light in free-space, and m is the mode index. The electric field changes the refractive index of the disk via the electro-optic effect and therefore shifts the spectral position of the optical resonances. The efficiency of electro-optic interaction between optical WGMs and the applied electric field is proportional to the optical interaction time and electric field intensity. The photon life-time inside the disk τ_{phot} is simply related to the slope of the Lorentzian via optical $Q \approx f\tau_{\text{phot}}$. Using this approach it is obvious that for

constant RF-power modulation is maximum when the input optical wavelength is located at the slope maximum of the optical resonance. For a Lorentzian line-shape the slope maximum occurs at frequency f_0 when the optical output is about 75% of its peak value. Through the modulation process optical power is coupled out of frequency f_0 into optical side bands $f_0 \pm f_{\text{RF}}$. However, only RF frequencies within about $\Delta f_m = f_m/Q$ (near 100 MHz for an optical $Q = 1.5 \times 10^6$) and centered at integral multiples of the optical FSR ($f_{\text{FSR}} = c/2\pi R n_e$) are able to modulate the optical carrier.

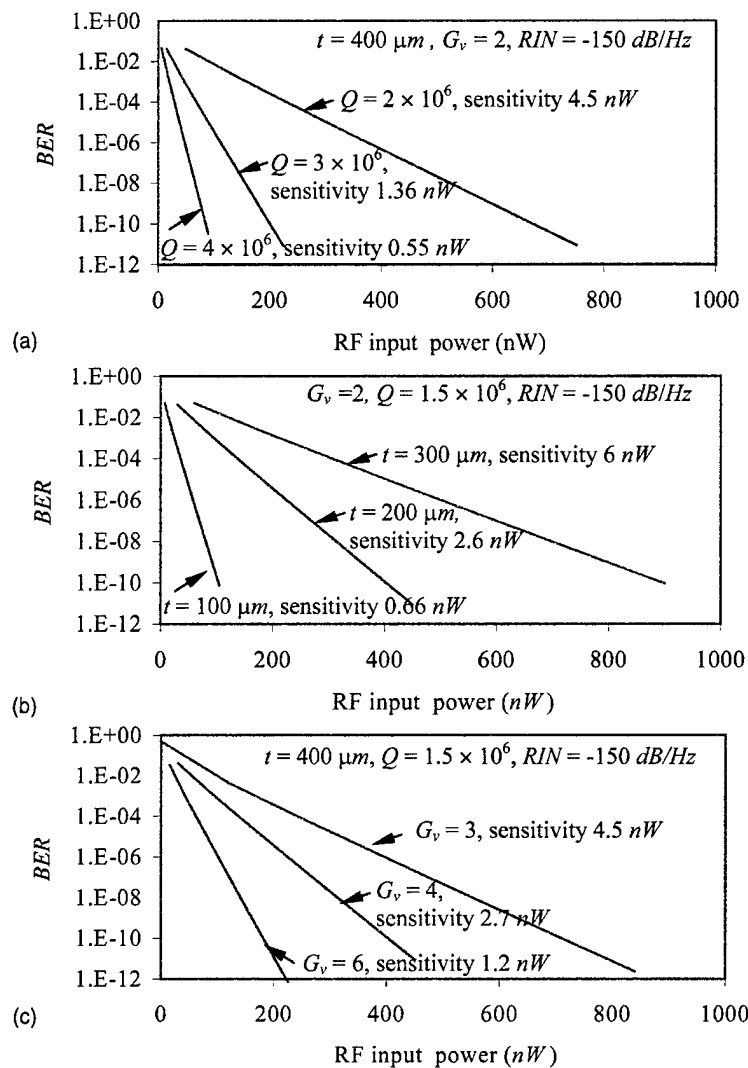


Fig. 4. BER calculations as a function of RF input power for different optical Q -factor, disk thickness, and voltage gain factor. In all cases optical coupling efficiency is 15%, RIN is -150 dB/Hz , optical input power is 5 mW, detector responsivity is 0.8 A/W, detector dark current is 10 nA, temperature is 300 K, detector impedance is 10 k Ω and detector amplifier noise-figure is 3 dB. The sensitivity is defined as the RF-power at which the SNR is unity. (a) Effect of optical Q -factor on BER performance. (b) Effect of disk thickness on BER performance. (c) Effect of RF resonator voltage gain factor on BER performance.

The voltage developed on the resonator, V_{res} , may be estimated as a function of RF input voltage, V_{line} , on the microstrip line. The RF-electrode, which is side-coupled to the line, has a voltage gain ($G_v = V_{\text{res}}/V_{\text{line}}$) proportional to its Q -factor. Knowing the physical specification of the disk (Q, t, R, n_c), RF-resonator gain G_v , optical coupling efficiency, optical input power and wavelength one may calculate the optical modulation amplitude as a function of RF input power.

3.2. Noise sources and critical parameters

Noise in the system is conveniently ascribed to either optical or electrical sources. The optical sources are laser relative intensity noise (RIN) and detector noise (thermal and shot noise). The electrical sources are the microstrip, RF-resonator, and amplification stages used after detection. A noise model may be used to estimate the performance of an ideal RF-optical link. We use BER and sensitivity as a measure of link performance. Our simulations show that critical parameters strongly influencing BER are optical Q -factor, disk thickness, RF resonator voltage gain, and optical input amplitude fluctuations (laser RIN).

3.3. Results

Fig. 4 shows simulation results for a RF-optical-link with direct detection. The BER is calculated as a function of RF input power for different optical Q -factors, disk thickness, and voltage gain, G_v . In all cases the assumptions are 5.13 mm disk diameter, $\text{RIN} = -150$ dB/Hz, 15% optical coupling efficiency, 5 mW optical input power, 0.8 A/W detector responsivity, 10 nA detector dark current, 300 K temperature, 10 k Ω detector impedance, and a 3 dB detector amplifier noise-figure. Sensitivity is defined as the RF-power at which the signal-to-noise ratio is unity ($\text{SNR} = 1$). In Fig. 4(a) the effect of optical Q -factor on BER performance is demonstrated for $t = 400$ μm and $G_v = 2$. As may be seen, increasing optical Q by a factor of two improves sensitivity by a factor of eight. Fig. 4(b) shows the effect of reducing the disk thickness for $G_v = 2$ and $Q = 1.5 \times 10^6$. Reducing the disk thickness increases the electric field intensity. In more advanced simulations G_v may be calculated as a function of RF coupling factor, the geometry of the resonator and input RF power. Fig. 4(c) shows the effect of increasing G_v on BER performance for $Q = 1.5 \times 10^6$ and $t = 400$ μm .

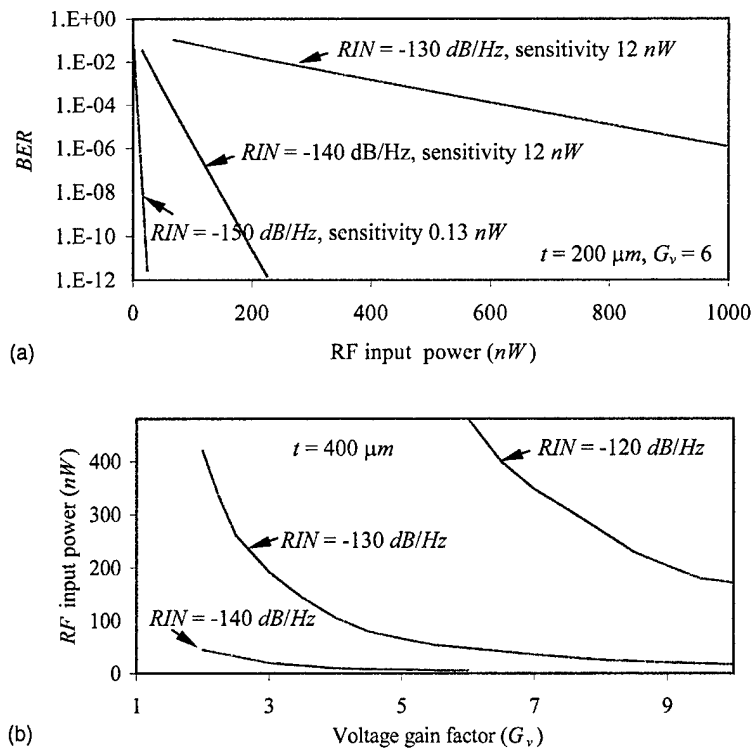


Fig. 5. Calculated influence of laser RIN on BER and sensitivity ($Q = 2 \times 10^6$ and other parameters are the same as Fig. 4). (a) BER performance with different values of RIN as a function of RF input power. (b) Sensitivity with different values of RIN as a function of G_v .

Fig. 5(a) illustrates how laser RIN can influence BER. In this case $G_v = 6$, $t = 200 \mu\text{m}$ and $Q = 2 \times 10^6$. With a value of $\text{RIN} = -140 \text{ dB/Hz}$ and $G_v = 6$ it is possible to achieve a BER around 10^{-10} with 200 nW RF input power. Fig. 5(b) shows it is possible to reduce the impact on sensitivity of noise generated due to laser RIN by increasing voltage gain G_v in the system. The results shown in Fig. 5(b) are obtained using $t = 400 \mu\text{m}$ and $Q = 2 \times 10^6$. Increasing voltage gain by a factor of five can be equivalent to reducing RIN by 10 dB/Hz.

4. Conclusion

In conclusion, we have demonstrated high-quality data transmission at Mb/s data rates over a RF-optical link using a new microdisk optical modulator. The modulator is able to efficiently modulate an optical carrier at $\lambda = 1550 \text{ nm}$ wavelength with a data modulated RF signal. By tuning the laser wavelength to a

high- Q optical mode 10 Mb/s NRZ 2⁷-1 PRBS data was successfully transmitted through a RF fiber-optic link with a measured BER of $<10^{-9}$. We have also demonstrated clean eye-diagrams may be achieved at 50 and 100 Mb/s rates. Calculations show nW sensitivity may be achieved by simply reducing disk thickness, increasing RF-resonator voltage gain, and reducing laser RIN.

Acknowledgements

This work is sponsored by NSF, NASA and DARPA.

References

- [1] Cohen DA, Levi AFJ. *Electron Lett* 2001;37:37.
- [2] Cohen DA, Hossein-Zadeh M, Levi AFJ. *Solid-State Electron* 2001;45:1577.



PERGAMON

Solid-State Electronics 45 (2001) 1577–1589

SOLID-STATE ELECTRONICS

High- Q microphotonic electro-optic modulator

D.A. Cohen, M. Hossein-Zadeh, A.F.J. Levi *

Department of Electrical Engineering, University of Southern California, Denny Research Building 118, Los Angeles, CA 90089-1111, USA

Received 28 January 2001; accepted 29 March 2001

Abstract

A microphotonic mm-wave modulator using simultaneous RF and optical resonance in an electro-optic medium is presented. Theory and simulation of modulator operation is discussed, and experimental results demonstrating modulation using simultaneous resonance in the mm-wave range are reported. © 2001 Elsevier Science Ltd. All rights reserved.

Keywords: mm-wave receiver; LiNbO₃ modulator; Resonant detection; Microphotonic; Microdisk; Microsphere; Resonator

1. Introduction

The wide-scale implementation of microwave cellular telephone networks, and continued need for personal data assistants (PDAs) is driving development of indoor wireless and microcell wireless systems [1]. Recently, a microphotonic modulator for a novel wireless and front-end RF receiver architecture operating at mm-wave frequencies was proposed [2]. Previous work has focused on modulator development and demonstration of efficient modulation at microwave frequencies [3,4]. In this paper, we present initial experimental results demonstrating modulation at mm-wave frequencies by achieving simultaneous resonance of RF and microphotonic electro-optic resonators. In addition, results of simulations describing optical modulation within the microphotonic resonator are presented.

2. LiNbO₃ microphotonic resonator

A microphotonic optical resonator is fabricated from an electro-optic material. In the work presented here, we use a z-cut LiNbO₃ disk-shaped resonator with optically polished curved side walls. The index of refraction along the extraordinary axis (z-axis) is $n_{\text{opt}} = 2.14$ at an optical

wavelength $\lambda = 1.5 \mu\text{m}$, and greater than 5.1 at RF frequencies in the mm-wave regime [5]. Simultaneous resonance between optical and RF fields is possible inside the disk. The optical field is resonant within the microphotonic modulator by confining a TE-polarized optical-field in a high quality-factor (Q) whispering-gallery mode (WGM) along the periphery of the disk, while metal electrodes feed RF power from a resonant electrical circuit. The optical resonator's large Q increases the effective interaction length of photons in the electro-optic material. In addition, a simultaneously resonant RF electrical feed for voltage enhancement and a patterned electrode structure provides high-sensitivity at mm-wave frequencies.

Fig. 1(a) shows the basic geometry of the LiNbO₃ resonator. These devices are disks of radius R , where $1 \leq R \leq 3$ mm, and thickness d , where $0.2 \leq d \leq 1$ mm. The side wall of the disk is optically polished with a radius of curvature, R' . In this work $R = R'$. The equator of the disk's curved side wall should be accurately maintained at height $d/2$. A photograph of a larger device is shown in Fig. 1(b) to illustrate the optically polished curved sidewalls of the resonator.

2.1. Solving for optical resonances in the microphotonic resonator

WGMs in disk-shaped dielectric resonators arise from solution of Maxwell's equations. The large dielectric

* Corresponding author. Tel.: +1-213-740-7318; fax: +1-213-740-9280.

E-mail address: alevi@usc.edu (A.F.J. Levi).

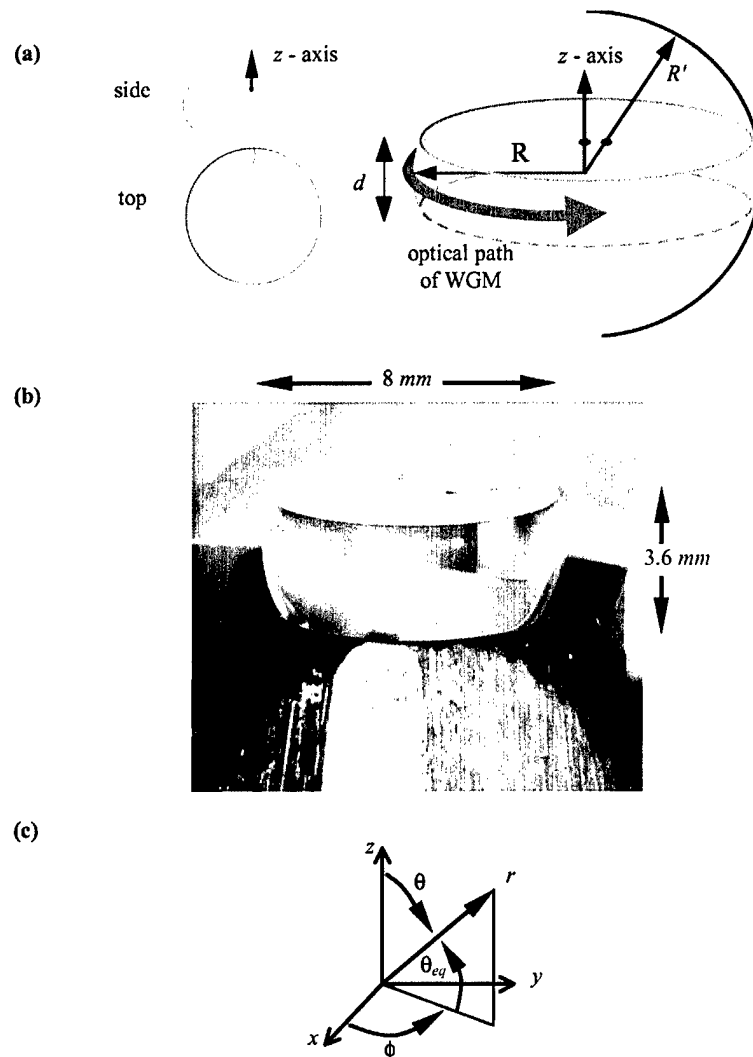


Fig. 1. (a) Geometry of a microdisk indicating disk radius R , disk thickness d and curved side walls with radius of curvature R' . (b) Photograph of a large z -cut LiNbO_3 disk-shaped resonator with solid-gold top and bottom flat-electrodes and optically polished curved side walls mounted on a ground plane. (c) The coordinate system used to solve the electromagnetic modes of a spherical resonator.

discontinuity between air and resonator result in electromagnetic resonances which in the ray-tracing approximation are explained by total internal reflection. When the disk radius R is equal to R' , the electromagnetic solutions to the disk resonator are found by defining the disk to be a sphere with part of the top and bottom hemispheres removed. Therefore, the nature of the WGMs propagating within the disk is, essentially the same as modes that propagate within passive dielectric microspheres. The only exception is that some higher-order modes are spatially filtered by losses introduced at the top and bottom disk interfaces. Whispering gallery resonances are characterized by high electric-field inten-

sity close to the air–dielectric interface and very high- Q . Loss due to finite curvature becomes small when the resonator dimension is significantly greater than the optical resonance wavelength. Hence, for optical wavelengths near $\lambda = 1.55 \mu\text{m}$, the Q of optical dielectric resonators greater than $\sim 10 \text{ m}$ in diameter is typically limited by attenuation due to scattering from surface imperfections.

The problem of electromagnetic oscillation in a dielectric sphere has been solved explicitly for a lossless, linear medium with no sources [6]. Assuming monochromatic solutions of the form $\mathbf{E}(\mathbf{r}, t) = \mathbf{E}(\mathbf{r})e^{-i\omega t}$ the vector Helmholtz equation is

$$\nabla^2 \mathbf{E}(\mathbf{r}) + \mu\epsilon \frac{\omega^2}{c^2} \mathbf{E}(\mathbf{r}) = 0$$

where ϵ and μ are the relative permittivity and permeability, and $\omega = 2\pi f$, where f is the frequency of the electric-field oscillation. We would like to express the vector \mathbf{E} in terms of radial (E_r), meridional (E_θ), and azimuthal (E_ϕ) components. However, the Laplacian of the vector \mathbf{E} results in three partial differential equations each involving E_r , E_θ , and E_ϕ . Hence, the simple separation of the Helmholtz equation in the rectangular coordinate system does not occur in the spherical coordinate system. It can be shown that three solutions in terms of the field ψ are

$$\mathbf{E} = (\nabla\psi)$$

$$\mathbf{E}_{\text{TE}} = (\mathbf{r} \times \nabla\psi)$$

$$\mathbf{E}_{\text{TM}} = \frac{ic}{\omega} \nabla \times (\mathbf{r} \times \nabla\psi)$$

These are also independent vector solutions which result in three separable partial differential equations. Using these solutions, the scalar Helmholtz equation is solved for ψ , where the scalar equation is given by

$$\nabla^2 \psi + \mu\epsilon \frac{\omega^2}{c^2} \psi = 0$$

The solutions \mathbf{E}_{TE} and \mathbf{E}_{TM} are those of interest for electromagnetic WGM solutions excited by evanescent coupling along the equator of the sphere. The first is named the transverse electric (TE) solution because \mathbf{E}_{TE} is tangent to the spherical surface, while the second is the transverse magnetic (TM) solution because the magnetic field \mathbf{H}_{TM} is tangent to the spherical surface [7]. This notation is opposite to that used with microdisk lasers [8] where TE polarization is along the radial unit vector. The microdisk laser definition comes from multiple quantum well slab-waveguide geometries.

Although the Helmholtz equation can be solved explicitly for the dielectric sphere, a simplification is achieved by assuming the electromagnetic field polarization may be approximated as constant along one coordinate axis [9]. In this case, the TE and TM modes are redefined as those with vector electric-field components

$$\mathbf{E}_{\text{TM}} = \hat{\theta} E_\theta \equiv \hat{\theta} \psi$$

$E_r = E_\phi = 0$, and TM modes defined as those with vector magnetic field components

$$\mathbf{H}_{\text{TM}} = \hat{\theta} H_\theta \equiv \hat{\theta} \psi$$

$H_r = H_\phi = 0$. The validity of this approximation has been confirmed numerically by Little et al. [9].

Such an approximation permits separation of the vector Helmholtz equation as seen with rectangular coordinates. Again starting with the vector Helmholtz equation, and using the definitions for \mathbf{E}_{TE} (\mathbf{H}_{TM}) above, the resulting scalar equation

$$\nabla^2 \psi + \mu\epsilon \frac{\omega^2}{c^2} \psi = 0$$

is easily solved in the spherical coordinate system. Boundary conditions are then applied to obtain the characteristic equations and normalization constants.

By imposing boundary conditions at the disk radius R_0 and restricting the spherical Bessel function from diverging at the origin, one obtains

$$\mathbf{E}_{\text{TE}}(\mathbf{H}_{\text{TM}}) = \sum \psi(r, \theta, \phi) = \sum_{lm} \psi'_l(r) Y_{lm}(\theta, \phi)$$

$$\psi'_l(r) \propto j_l(kr), \quad r \leq R_0$$

$$\psi'_l(r) \propto e^{-\alpha_s(r-R_0)}, \quad r > R_0$$

where $j_l(kr)$ are spherical Bessel function, Y_{lm} are spherical harmonics, and l and m are eigenvalues solved from boundary conditions. The exponential decay defines only the bound portion of the field outside the sphere. Radiation modes are ignored. In the equations above $k = 2n_s/\lambda$, where n_s is the refractive index of the sphere, and λ is the electromagnetic wavelength in free space. The third eigenvalue n is found from the characteristic equations resulting from the boundary condition that the interior and exterior tangential fields at the surface of sphere must be equal.

From these solutions, we find the eigenmodes of the microresonator are characterized by polarization (TE or TM), and the three eigenvalues n , l , and m . The radial eigenvalue $n \gg 1$ is the number of field maxima in the direction of the sphere radius, l is approximately the number of wavelengths that fit into the optical length of the resonator, and m is the number of field maxima in the equatorial plane. We will show later that the number of polar intensity maxima is $l - m + 1$.

We see that as $l = m$ increases, the optical power begins to concentrate closer to the equator. The longitudinal cross-section of the x - z plane displays the concentration of field toward both the equator and disk edge as l and m increase. A cross-section of the mode in the x - y plane demonstrates the increase in number of field maxima, and a trend in which the mode becomes increasingly confined to the disk edge.

A significant approximation can be made with the angular distribution of the mode along the polar axis [10]. We define a new coordinate $\theta_{\text{eq}} = \theta - \pi/2$, such that $\theta_{\text{eq}} = 0$ along the equator as shown in Fig. 1(c). Making the approximations $\theta_{\text{eq}} \ll 2\pi$ and $m \gg 1$, and

including this in the polar differential equation, $\psi_\theta(\theta_{eq})$ becomes

$$\psi_\theta(\theta_{eq}) \propto e^{-m/2\theta_{eq}^2} H_N(\sqrt{m}\theta_{eq})$$

$$N = l - m$$

where $H_N(x)$ are the Hermite polynomials, with $H_0(x) = 1$, $H_1(x) = 2x$, $H_2(x) = 4x^2 - 2$, etc. For case of large m , and $l \approx m$ the resulting WGM is Gaussian in nature. From this approximation, and the nature of Hermite polynomials, we see that there are $l - m + 1$ polar intensity maxima. At $l - m = 0$, the mode is Gaussian and centered about the equator. As $l - m$ increases, the energy distribution spreads further from the equator. Because input laser light typically has a Gaussian beam profile, we expect that the $l = m$ Gaussian modes are those that are most strongly coupled [10]. In addition, in a perfect sphere, WGM frequencies depend only on n and l , and hence are $2m + 1$ degenerate in frequency. However, in any sphere with finite ellipticity this degeneracy is broken [11].

Fig. 2 shows the simulated WGM power distribution for disks typical of that used in experimentation. Fig. 2(a) shows the normalized radial profile of the spherical

Bessel function with $n = 1$ for a 2.0 mm ($l = 8690$), 3.5 mm ($l = 15120$), and 5.84 mm ($l = 25260$) disk. By approximating the boundary condition at the disk radius to be $E_{TE}(R) = 0$, the full width half maximum (FWHM) of the modes along the radius are 2.6, 3.7, and 4.8 μm for the 2.0, 3.5, and 5.84 mm disks, respectively. Normalized profile along the z -axis for $N = l - m = 0, 1, 2$, and 3 for a 2.0, 3.5, and 5.84 mm disk are plotted in Fig. 2(b). These figures demonstrate that the relative angular distribution of the mode increases with decreasing disk radius, but the actual mode height along the z -axis decreases.

Fig. 3(a) shows the two-prism evanescent coupling scheme used to couple light into and out of the disk. When TE-polarized WGM modes are excited within the LiNbO₃ microphotonic resonator the detected optical spectrum shows peaks corresponding to the free spectral range (FSR) of the resonant cavity. This FSR is defined as $\Delta f_{FSR} \approx c/(n_{opt}2\pi R)$, where n_{opt} is the optical refractive index, and R is the radius of the disk. It should be noted that $1/\Delta f_{FSR}$ is equal to the round trip time of the cavity $\tau_{disk} = (n2\pi R)/c$. Results using a tunable DFB laser to scan the entire FSR of the disk are shown in Fig. 3(b) for a disk of diameter $2R = 5.85$ mm, and thickness

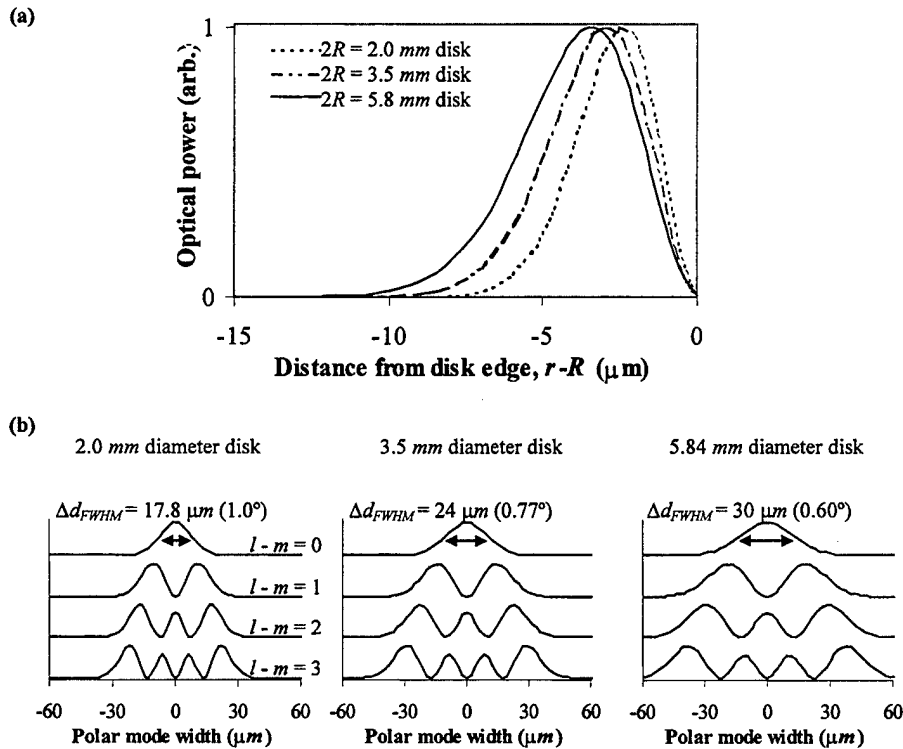


Fig. 2. WGM power distribution for disks of large $l = m$. (a) Normalized profile of spherical Bessel functions with $\eta = 1$ for a 2.0 mm ($l = 8690$), 3.5 mm ($l = 15120$), and 5.84 mm ($l = 25260$) disk. The FWHM of the modes are 2.6, 3.7 and 4.8 μm for the 2.0, 3.5 and 5.84 mm disks, respectively. (b) Normalized profile of spherical harmonics using Hermite polynomial approximation for $N = l - m = 0, 1, 2$, and 3 for a 2.0, 3.5, and 5.84 mm disk.

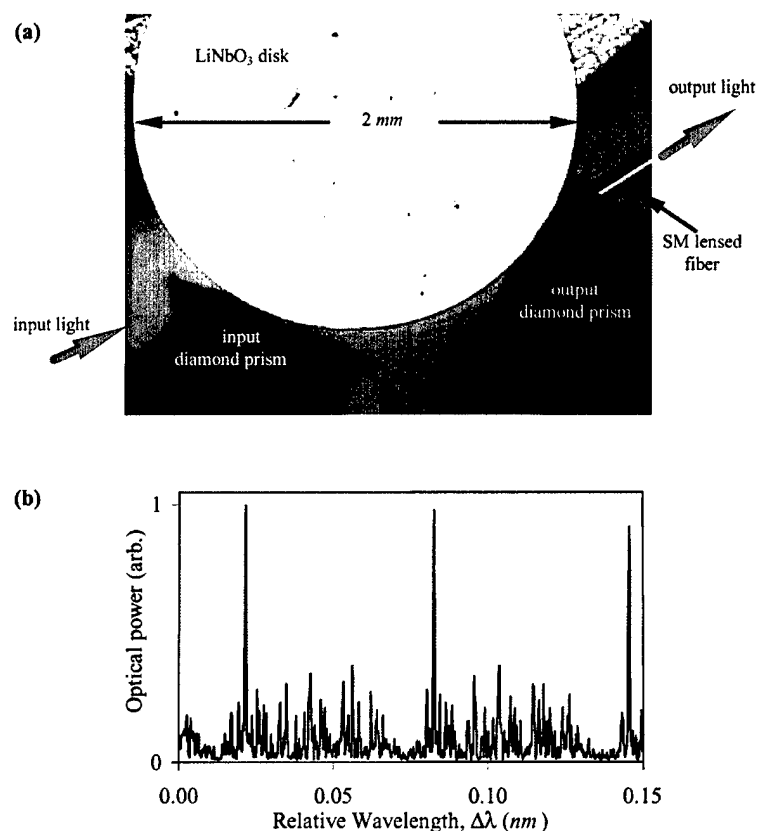


Fig. 3. (a) Top view of two prism coupling using diamond prisms. Input light is coupled into the prism on the right. Light output from the disk is collected at the single mode fiber output coupler. (b) Optical spectrum for TE polarized light when alignment is optimized for single optical mode excitation with FSR = 7.57 GHz, and $Q > 4 \times 10^6$. The disk used has a diameter 5.85 mm and thickness of 0.7 mm. Wavelength of lasing light is 1.55 μm .

$d = 0.74$ mm. This disk exhibited a FSR of 7.57 GHz (60.6 pm) for TE optical modes with WGM optical Q greater than 4.1×10^6 .

2.2. Electro-optic modulation configuration and theory

Fig. 4(a) shows the schematic diagram of the experimental approach. An RF input signal is incident on the modulator electrodes. This mm-wave signal feeds the electrodes of the microphotonic resonator where the RF signal is directly converted via the electro-optic response of the modulator to an optical signal with a 200 THz optical carrier frequency supplied by a DFB laser. By patterning metal electrodes periodically about the disk circumference, it is possible to obtain a resonant optoelectronic modulation response at large RF frequencies. Photons make a number of round trips in the resonator, thereby interacting with the RF field on multiple passes which increase the total phase shift seen by any individual photon. This results in improved sensitivity to the applied RF field. The resulting phase-modulated

optical signal may be converted to amplitude modulation through use of a standard Mach–Zehnder configuration. The intensity of the amplitude-modulated optical carrier is detected using an optical receiver whose response is sensitive only to base-band frequencies.

Basic principles regarding the coupling of photons into and out of the microphotonic resonator can be understood through a directional coupler approach. Fig. 5 shows the generic approach to model the coupling of light from any evanescent coupler (e.g. prism) into a disk or ring structure. Input light is incident on coupling region 1 with an electric-field coupling coefficient $i\kappa_1$ and output from coupling regions 1 and 2 with electric-field coupling coefficients $i\kappa_1^*$ and $i\kappa_2^*$, respectively. Single prism coupling is defined when monitoring output 1 with $\kappa_2 = 0$, and two prism coupling when monitoring output 2 with $\kappa_2 \neq 0$.

Using the steady-state loop approach [11], A_1 is defined as the steady state electric-field amplitude for input light entering coupling region 1, B_1 is the field exiting coupling region 1, and A_2 and B_2 are the fields inside the

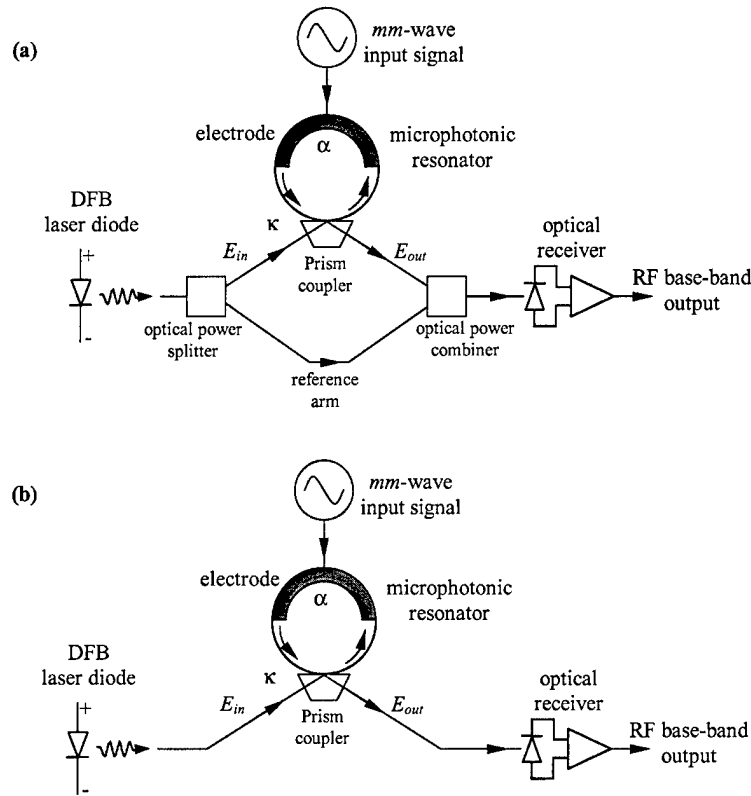


Fig. 4. (a) Schematic showing the receiver proposed for mm-wave RF detection. An electromagnetic wave received at a RF antenna feeds electrodes of the microphotonic modulator. The modulator directly converts the RF signal to an optical carrier via the electro-optic effect. The resulting phase-modulated optical signal is converted to amplitude modulation through the use of a standard Mach-Zehnder configuration. (b) Schematic showing the receiver proposed for mm-wave RF detection without the need of a Mach-Zehnder reference arm. The phase-modulated optical signal is internally converted to amplitude modulation through interference with previous optical round trips.

resonator before and after coupling region 1. Similarly, D_1 is the field exiting coupling region 2, and C_2 and D_2 are the fields inside the resonator before and after coupling region 2. For simplicity, a lossless symmetric coupler is assumed, with field coupling constant $ik_1 = -ik_1^*$ in region 1, and ik_2 in region 2. The transmission coefficient $T_{A_1 B_1}$ from A_1 to B_1 is $T_{A_1 B_1} = (1 - \kappa_1^2)^{1/2}$. In the case of the prism coupler, the coupling coefficient κ is a function of gap spacing, coupler geometry, and disk size.

The round-trip disk electric optical field transmission coefficient $\alpha = \alpha_1 \alpha_2$, where $\alpha_1 = \exp(-\alpha_{01} L_1/2)$ is the electric-field transmission coefficient for the length L_1 between coupling regions 1 and 2, and $\alpha_2 = \exp(-\alpha_{02} L_2/2)$ is the electric-field transmission coefficient for the length L_2 between coupling region 2 and before region 1. The constants α_{01} and α_{02} are the optical power loss per unit length for the regions L_1 and L_2 , respectively. The refractive index of the resonator is n_d . Finally, the round-trip time of the disk is $\tau = \tau_1 + \tau_2$, where $\tau_1 = n_d L_1/c$,

and $\tau_2 = n_d L_2/c$. The self-consistent relations between field amplitudes at a time t for the two coupling regions are

$$B_1(t) = (1 - \kappa_1^2)^{1/2} A_1(t) + i\kappa_1 A_2(t)$$

$$B_2(t) = i\kappa_1 A_1(t) + (1 - \kappa_1^2)^{1/2} A_2(t)$$

$$D_1(t) = i\kappa_2 C_2(t)$$

$$D_2(t) = (1 - \kappa_2^2)^{1/2} C_2(t)$$

while optical propagation between coupling regions give

$$C_2(t) = \alpha_1 e^{-i\phi_1(t)} B_2(t - \tau_1)$$

$$A_2(t) = \alpha_2 e^{-i\phi_2(t)} D_2(t - \tau_2)$$

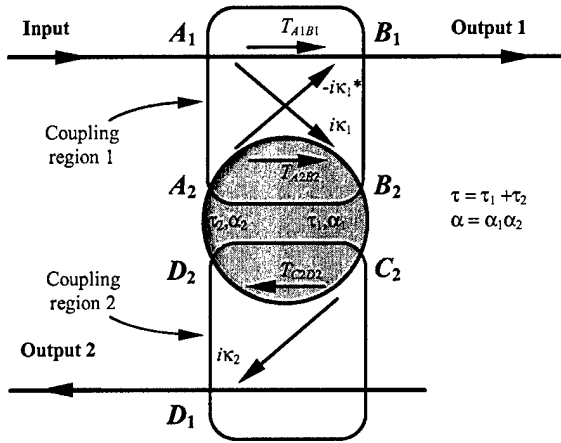


Fig. 5. Directional coupler model used to understand coupling principles of a microphotonic modulator. Photons incident on the input directional coupler are evanescently transferred into a ring or disk. After traveling around the disk, light is evanescently coupled out of the resonator at either output 1 or output 2. T_{ij} is the electric-field transmission coefficient of the coupling region, κ_i is the electric-field coupling coefficient of the coupling region, and α_i is the electric field transmission coefficient between coupling regions. Coupler losses are ignored.

Where $\phi_1(t)$, and $\phi_2(t)$ are the electrically induced optical phase shift along lengths L_1 and L_2 . Using recursion and assuming a monochromatic input, the total output field from coupling region 1, $E_{out1}(t) \equiv B_1(t)$ as a func-

tion of the field input to coupling region 1, $E_{in}(t) \equiv A_1(t)$ then $E_{in}(t - p\tau) = E_{in}(t) e^{-i\omega p\tau}$, and

$$E_{out1}(t) = \left[\sqrt{1 - \kappa_1^2} - \frac{\kappa_1^2}{\sqrt{1 - \kappa_1^2}} \sum_{p=1}^{\infty} \rho_1^p \exp \left(i \sum_{q=0}^{p-1} [\phi_1(t - \tau_2 - q\tau) + \phi_2(t - q\tau)] \right) \right] E_{in}(t)$$

$$\rho_1 \equiv \alpha \sqrt{1 - \kappa_1^2} \sqrt{1 - \kappa_2^2} e^{i\omega\tau}$$

where ω is the optical frequency. Similar to the above method, recursion is used to find the total electric-field output from coupling region 2, $E_{out2}(t) \equiv D_1(t)$ as a function of $E_{in}(t)$. This gives

$$E_{out2}(t) = \left[-\kappa_1 \kappa_2 \alpha_1 e^{i(\omega\tau_1 + \phi_1(t))} \left(1 + \sum_{p=1}^{\infty} \rho_2^p \exp \left(i \sum_{q=0}^{p-1} [\phi_1(t - (q+1)\tau) + \phi_2(t - \tau_1 - q\tau)] \right) \right) \right] E_{in}(t)$$

$$\rho_2 \equiv \alpha \sqrt{1 - \kappa_1^2} \sqrt{1 - \kappa_2^2} e^{i\omega\tau}$$

RF modulation frequency of the microphotonic resonator is determined by the FSR of the optical resonator

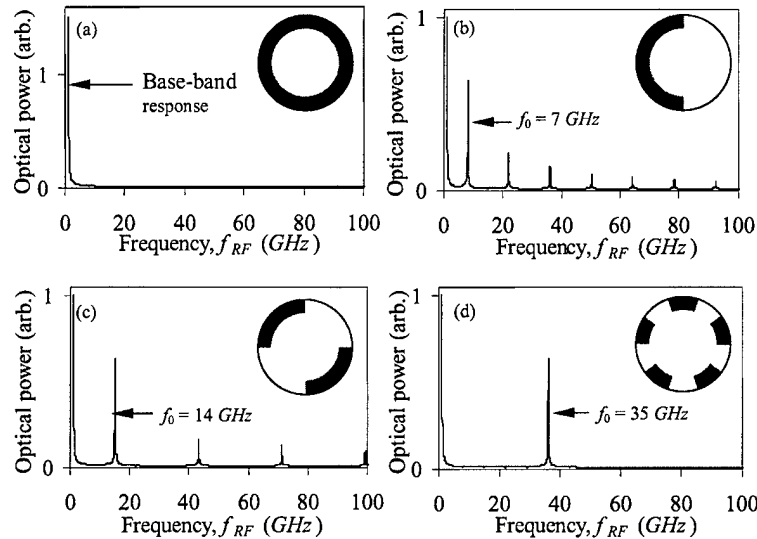


Fig. 6. Calculated response of a microphotonic-based opto-electronic modulator with the indicated periodic metal electrode structures. (a) A $R = 3.18$ mm LiNbO₃ disk modulator with $\kappa = 0.05$ and a continuous ring electrode. (b) $\kappa = 0.05$ with a split 2-segment ring-electrode showing resonant opto-electronic response at 7 GHz. (c) $\kappa = 0.05$ with 4 segments and response at 14 GHz. (d) $\kappa = 0.05$ with 10 segments showing response at 35 GHz.

and the spatial pattern of the metal electrode structure. The frequency of the RF carrier f_{RF} should be an integral multiple m of the optical FSR, f_{FSR} , where $f_{FSR} = 1/\tau_{disk} = c/(n_{opt}2\pi R)$, τ_{disk} is the optical round-trip time of the disk, and R is the disk radius [12]. A periodic metal electrode structure permits operation of the modulator well beyond a typically 20 GHz –3 dB roll-off of conventional commercial LiNbO₃ modulators.

As shown in Fig. 6(a) for a resonant solid-ring electrode, high optical- Q results in a summation of multiple round trips that further suppresses modulation efficiency at finite frequency. Fig. 6(b)–(d) illustrates how a change in the metal electrode pattern shifts the resonant response to higher frequencies with little decrease in efficiency.

The relative response at the resonant frequency compared to base band is 0.63 indicating the potential for efficient modulation. A larger modulation response at base-band results because a photon will encounter a larger average electric field during a single round trip. This is because the time constant determining this response is the round trip time $\tau_{disk} = 1/f_{FSR}$ of the disk.

Fig. 7(a) plots the optical power for the split 2-segment electrode case shown in Fig. 6(b) on a logarithmic scale. RF detected power would be two times optical power on this log scale. Fig. 7(b) and (c) shows expanded views of the optical modulation response at base band and fundamental disk frequency. Qualitatively, the presence of modulation dips result from spectral filtering

by the optical resonance of the optical modulation side bands.

Fig. 8 qualitatively explains the presence of the dips. At base band for a fixed RF power and frequency f_{RF} , modulated optical power will be coupled out of the optical carrier frequency $f_{opt} = c/\lambda_{opt}$ and into optical side bands $f_{opt} \pm f_{RF}$. All three optical frequencies, f_{opt} and $f_{opt} \pm f_{RF}$, must be resonant within the disk to propagate.

Both experiment and simulation have verified that maximum modulation occurs near the maximum slope of the CW optical resonance, labeled in Fig. 7(a) as λ_{opt} . The base-band modulated response for the $\kappa = 0.05$ split 2-segment ring-electrode of Fig. 6(b) is shown in Fig. 7(b).

As f_{RF} increases, the optical side bands are modified according to the optical resonance peak. The approximate condition for maximum modulation occurs when one optical side band is aligned with the resonance peak ($f_{RF} = f_2$ in the figure). In the simulation, the optical input wavelength λ_{opt} was centered above the resonant wavelength such that $\Delta f = f_{peak} - f_{opt} = 50$ MHz.

In agreement with this qualitative description, simulated maximum modulation occurs at 54 MHz. The dip at 7 GHz is understood through a similar argument, where side bands are shifted by plus and minus one FSR into adjacent resonances. The peaks at 7 GHz occur ± 4 MHz from the 7 GHz dip. Fig. 7(d) demonstrates the null in modulation when excited at the second harmonic

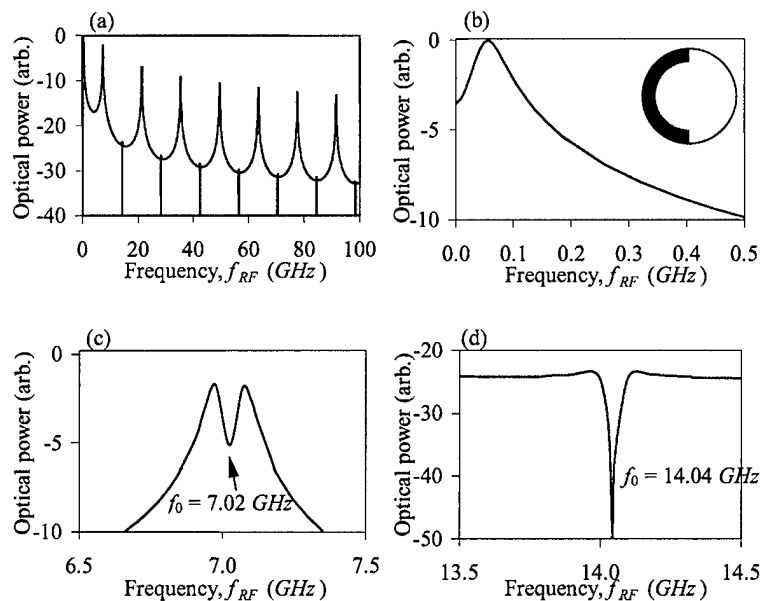


Fig. 7. (a) Calculated response of the $\kappa = 0.05$ with split 2-segment ring-electrode of Fig. 6(b) shown using a log scale. (b) Expanded view of the base-band response. (c) Expanded view of the fundamental 7 GHz modulation response showing a modulation dip at the center of the modulation peak. (d) Expanded view at 14 GHz showing a null in modulation at the second harmonic.

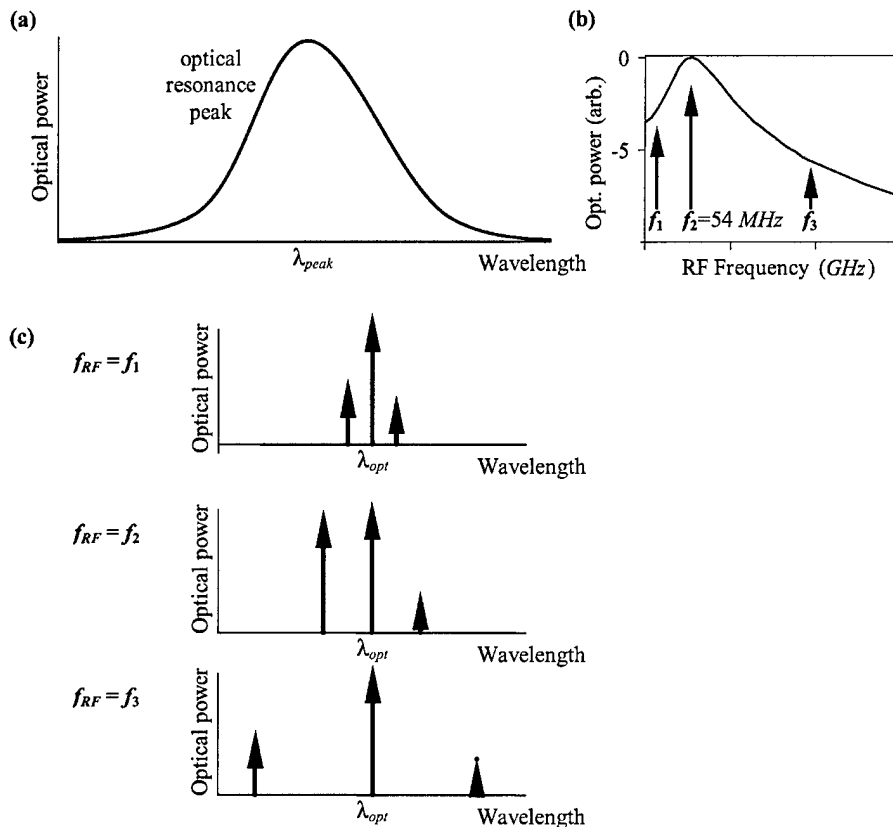


Fig. 8. (a) CW optical resonance peak centered at wavelength λ_{peak} . (b) Optical modulation response as a function of applied RF frequency for the two-section electrode in Fig. 6(b). (c) Optical carrier and side-band wavelengths for the three indicated RF frequencies shown in part (b). The amplitude of each wavelength is optically filtered by the resonance peak. Therefore $f_{RF} = f_2$ will have the maximum modulation as shown in (b).

frequency. This results when light passing between the electrode is modulated at the second harmonic of the total round trip frequency. In this case, the total phase shift from the electrode is zero, and there is no modulation.

2.3. The role of the reference arm

Both experiment and simulation have shown that the reference arm in Fig. 4(a) is not always necessary, and the configuration shown in Fig. 4(b) can be used to achieve efficient modulation. For a single coupler configuration ($\kappa_2 = 0$), Fig. 9 shows as the coupling coefficient decreases, a point is passed where the Mach-Zehnder geometry is no longer needed.

Amplitude modulation is achieved through a combination of two mechanisms. In the first, phase-shifted light exiting the active arm of the Mach-Zehnder interferes with light in the reference arm, thereby converting phase information to amplitude modulation. In the second mechanism, because light of increasing

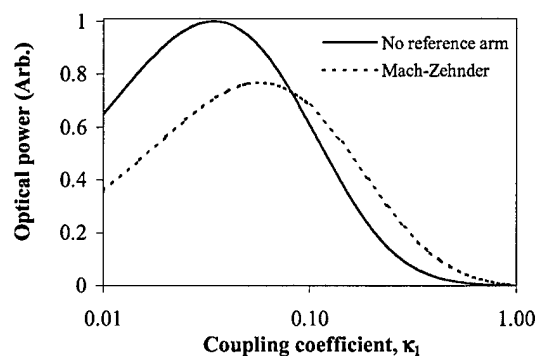


Fig. 9. Simulated comparison of modulation with and without use of a Mach-Zehnder geometry using the single-coupler geometry. Amplitude modulation without the Mach-Zehnder is shown to result in larger modulation at coupling coefficients $\kappa_1 < 0.085$. Values used in the simulation are the same as those in Fig. 6(b).

round-trip number has a larger accumulated phase shift, amplitude modulation will result due to interference

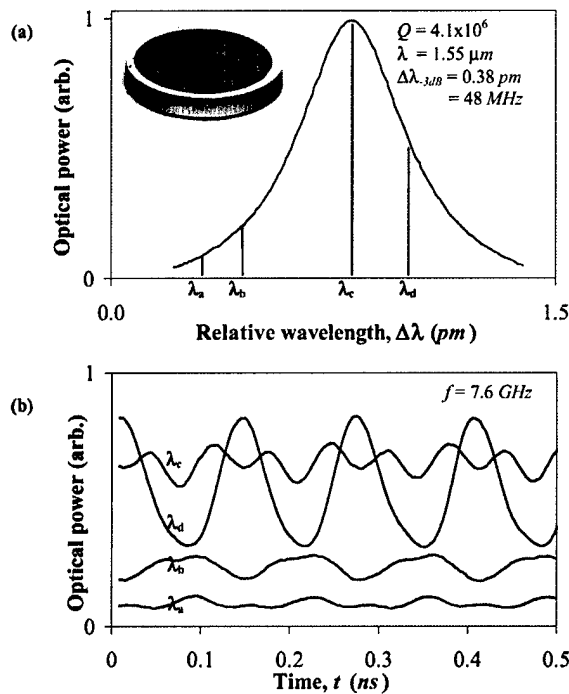


Fig. 10. (a) Measured optical resonance of the LiNbO₃ microphotonic disk modulator near wavelength $\lambda = 1.55 \mu\text{m}$. The measured Q of this device is more than 4×10^6 . Inset shows a photograph of a z-cut LiNbO₃ disk-shaped resonator with optically polished curved side walls. Gold electrodes are placed in an annulus around the disk to increase the overlap of electrical bias and optical fields. The dimensions of the disk are radius $R = 2.92 \text{ mm}$ and thickness $d = 0.74 \text{ mm}$. (b) Detected optical time-domain signal showing 7.56 GHz modulation. Modulation is shown at four wavelengths referenced in (a), and is maximum at a wavelength corresponding to the maximum slope of the optical resonance.

between individual round trips. Because each round-trip optical path length is an integral multiple of the optical wavelength, this “self-modulation” is inherently phase matched.

Fig. 9 shows a comparison of modulation with and without the Mach–Zehnder geometry. In a single pass limiting case $\kappa_1 = 1$ and $\kappa_2 = 0$, light passing along the active arm is phase modulated. It is then amplitude modulated via interference with light from the reference arm. Because there is only one round trip, there is no self-modulation. As κ_1 decreases from 1, self-modulation becomes a larger fraction of the total modulation, and amplitude modulation via the Mach–Zehnder mechanism becomes less important. Below a value of $\kappa_1 = 0.085$ in the simulation, the Mach–Zehnder geometry is disadvantageous, and a modulation geometry without the reference arm is more efficient. Hence, microphotonic modulators with small values of κ_1 are best

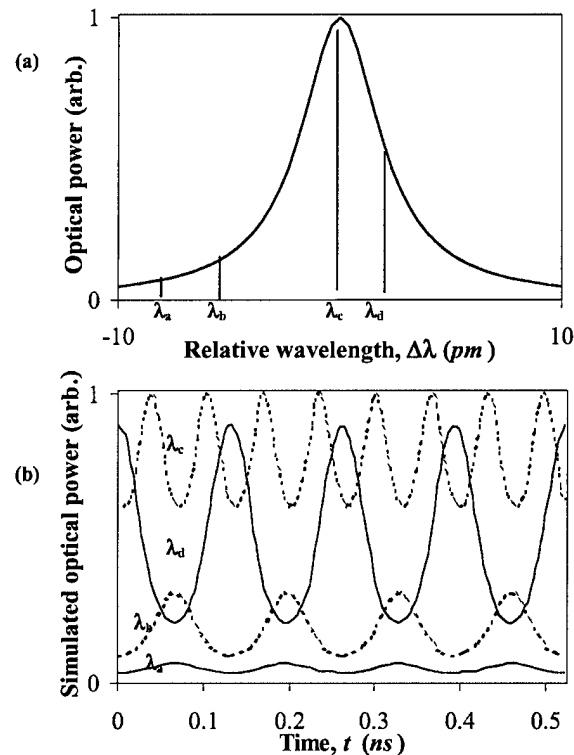


Fig. 11. (a) Simulated optical resonance of the LiNbO₃ microphotonic disk modulator near wavelength $\lambda = 1.55 \mu\text{m}$. The radius of the disk is $R = 2.92 \text{ mm}$. (b) Simulated optical time-domain signals showing 7.6 GHz modulation. Modulation is shown at four wavelengths referenced in (a), and is maximum at a wavelength corresponding to the maximum slope of the optical resonance.

implemented without use of a reference arm (see Fig. 4(b)).

Comparison of experiment and simulation shows the typical coupling coefficients are $\kappa_1 < 0.05$, and therefore using a single-arm non-Mach–Zehnder configuration results in a more efficient modulation geometry. This more efficient and less complex experimental configuration is used for all experimental results presented here.

2.4. Comparison of calculated and measured modulation response

Fig. 10(a) shows the measured optical spectrum of the WGM resonance in the absence of RF modulation, with a resulting optical $Q = 4 \times 10^6$. As shown in Fig. 10(b), measured optical modulation in the time domain is maximized for a fixed RF input power when the optical wavelength λ_d is located at the maximum slope of the WGM spectral shape. Frequency doubling is shown to occur at the wavelength λ_c at the center of the optical resonance. In addition, because the slopes are opposite

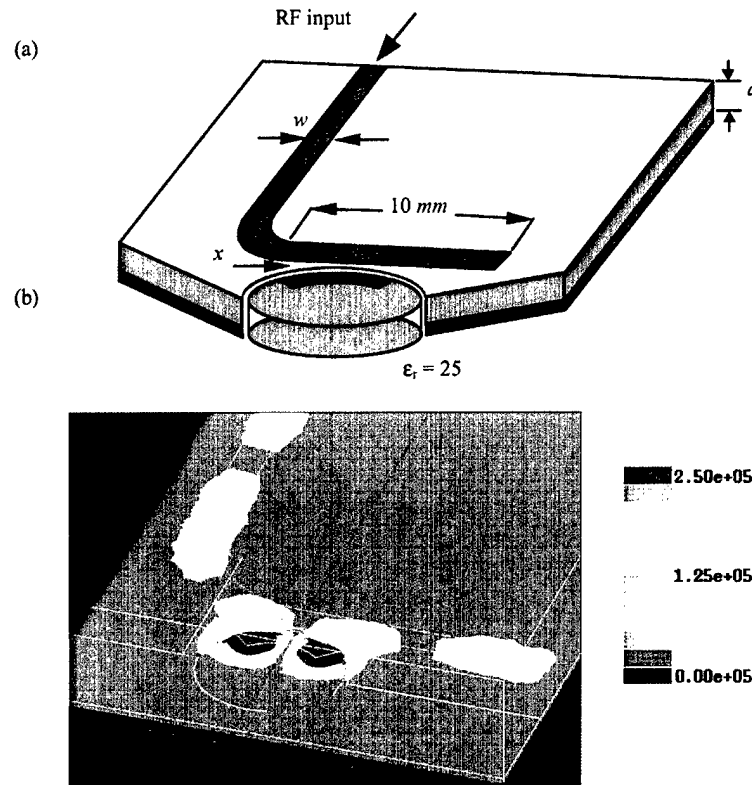


Fig. 12. (a) Side-coupled resonator geometry used to achieve simultaneous resonance with RF voltage gain. (b) Simulation results showing the RF intensity at the fundamental frequency of the RF resonator. The simulation assumed a dielectric thickness, $d = 0.508$ mm, relative dielectric constant, $\epsilon_r = 2.94$, line width, $w = 1.2$ mm, disk thickness, $t = 0.7$ mm, resonator width = 1.2 mm, resonator angle = 90° , and gap spacing, $x = 0.3$ mm. Scale is in arbitrary linear units.

on either side of the optical resonance, the modulation response at λ_c and λ_d are π out of phase.

As additional confirmation of the microphotonic resonator modulation model, time domain simulation is compared to the experimental data shown in

Fig. 11. Fig. 11 shows very good agreement with the experimental data in Fig. 10, including frequency doubling, the π phase change, and maximum modulation occurring near the maximum slope of the optical resonance.

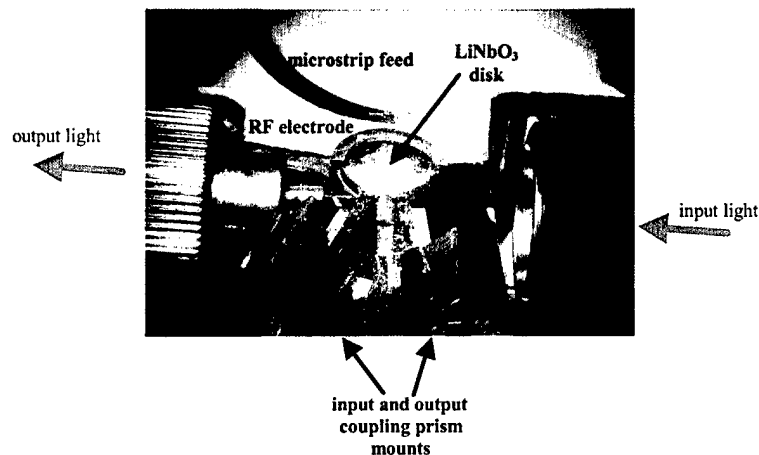


Fig. 13. Photograph showing the experimental setup used for the side-coupled electrode coupling scheme.

3. RF modulation experiments at mm-wave frequencies

3.1. Side-coupled electrode coupling

A side-coupled microstripline resonator is used to achieve both voltage amplification and efficient RF coupling to the microphotonic resonator electrode. Fig. 12(a) shows the geometry of the side-coupled electrode. A SMA launch is used to couple power from the RF source to a microstrip line of $50\ \Omega$ impedance patterned on a RT-Duroid 6002 substrate with $\epsilon_r = 2.94$. Simulation shows that RF power reflects from the open end of the microstrip line generating the standing wave pattern seen in Fig. 12(b). However, part of the RF power evanescently couples to a microstrip resonator of length L that is either patterned or placed on the LiNbO₃ disk. This coupled power generates standing waves at RF frequencies $f_{RF} = mc/(2n_{eff}L)$, where n_{eff} is the effective RF index of refraction seen by the RF mode, and m is an integer. Fig. 12(b) shows RF intensity of a simulated resonant standing wave.

Fig. 13 shows the RF and optical experimental configuration. Prisms are used to couple laser light of approximate wavelength $\lambda = 1.55\ \mu\text{m}$ into and out of the WGM optical mode of the microphotonic resonator. The optical wavelength is tuned to a resonant wave-

length of the optical resonator. A RF electric field propagating on a $50\ \Omega$ impedance metal microstrip line evanescently side couples to a metal electrode resonator on the LiNbO₃ disk. The fundamental resonant frequency of the electrode resonator is tuned to match the optical FSR of 7.56 GHz.

3.2. Experimental results of mm-wave modulation

Demonstration of mm-wave modulation in the LiNbO₃ microphotonic resonator using simultaneous RF and optical resonance with voltage gain on the RF electrode is shown in Fig. 14(a). Optical modulation is demonstrated in the Ka band at 30.3 GHz. By side coupling a 30.3 GHz RF signal into the third harmonic of a 10.1 GHz RF microstrip resonator, optical modulation at 30.3 GHz is achieved. Fig. 14(b) shows only residual modulation when the optical wavelength is tuned-off resonance, while the RF frequency is still set to resonance. Fig. 14(c) shows the optical wavelength on resonance, with the RF frequency tuned-off resonance.

Using a similar experimental arrangement, optical modulation at 37.9 GHz has also been demonstrated as shown in Fig. 15. This modulation used the third harmonic of a 12.6 GHz microstrip resonator for RF coupling to the metal electrode.

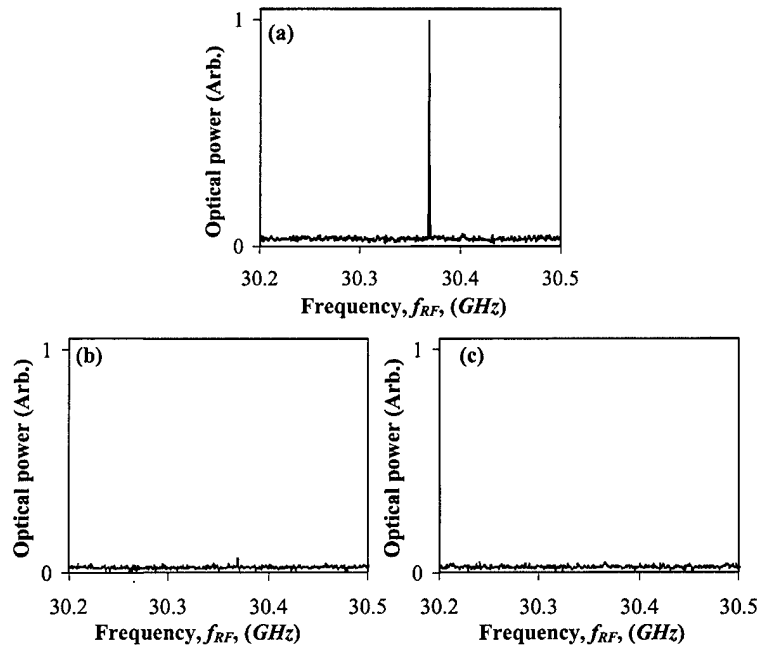


Fig. 14. (a) Demonstration of mm-wave modulation at 30.37 GHz using a LiNbO₃ microphotonic resonator with both the RF frequency and optical wavelength tuned to resonance. (b) When the optical wavelength is tuned-off resonance, while the RF frequency stays in resonance, no modulation is measured. (c) No modulation is observed if the optical wavelength is kept tuned on resonance while the RF frequency is tuned-off resonance.

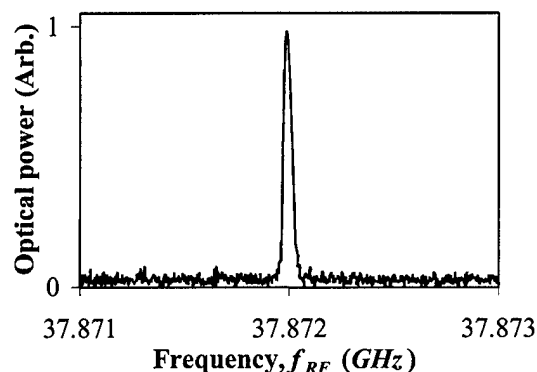


Fig. 15. Measured modulation response of a LiNbO₃ microphotonic resonator at 37.9 GHz. RF resonance was achieved using the third harmonic of a 12.6 GHz microstrip resonator.

4. Conclusion

Theory and simulation for a new type of mm-wave RF modulator with direct electrical-to-optical conversion has been discussed. Simulation shows very close agreement with experimental results at GHz frequencies and confirms our model. In addition, experimental modulation of a RF carrier using a side-coupled RF coupling scheme has demonstrated modulation at frequencies approaching 40 GHz.

Acknowledgements

This work is supported in part by NSF under contract ECS-9979331 and the DARPA RFLICs program.

References

- [1] Ohata K, Inoue T, Funabashi M, Inoue A, Takimoto Y, Kuwabara T, Shinozaki S, Maruhashi K, Hosaya K, Nagai H. *IEEE Trans Microwave Theory Technol* 1996;44:2354.
- [2] Cohen DA, Levi AFJ. *Electron Lett* 2001;37:37.
- [3] Cohen DA, Levi AFJ. *Solid-State Electron* 2001;45:495.
- [4] Cohen DA, Hossein-Zadeh M, Levi AF. *J Electron Lett* 2001;37:300.
- [5] Robertson WM, Arjavalingam G, Kopcsay GV. *Electron Lett* 1991;27:175.
- [6] Stratton JA. *Electromagnetic theory*. New York: McGraw-Hill; 1941.
- [7] Reitz JR, Milford FJ, Christy RW. *Foundations of electromagnetic theory*, third edition. New York: Addison-Wesley, 1980.
- [8] Frateschi NC, Levi AFJ. *J Appl Phys* 1996;80:644.
- [9] Little BE, Laine JP, Haus HA. *J Lightwave Technol* 1999; 17:704.
- [10] Kight JC, Dubreuil N, Sandoghdar V, Hare J, Lefevre-Seguin V, Raimond JM, Haroche S. *Opt Lett* 1995;20: 1515.
- [11] Gorodetsky ML, Ilchenko VS. *Opt Commun* 1994;113: 133.
- [12] Kourogi M, Nakagawa K, Ohtsu M. *IEEE J Quantum Electron* 1993;29:2693.

a result, the bandwidth was reduced to ~ 40 GHz. This reduction is caused by the larger microwave and optical velocity mismatch. This result reveals that the electrode works, at least in major aspects, in a travelling-wave manner.

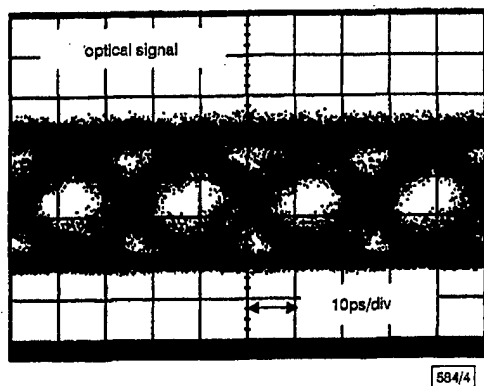


Fig. 4 40 Gbit/s eye-diagram

Fig. 4 shows the eye-diagram of the 40 Gbit/s modulated light from the TW-EADFB. The injection current of the DFB laser was set to 110 mA, and the modulating-amplitude to the TW-EA modulator was 1.5 V. As shown in Fig. 4, the eye opening was successfully observed.

Conclusion: The first-ever EA-DFB with a travelling-wave electrode has been developed. It exhibits a very wide bandwidth of over 50 GHz. A 40 Gbit/s eye-diagram was successfully observed.

© IEE 2001

13 October 2000

Electronics Letters Online No: 20010168

DOI: 10.1049/el:20010168

Y. Akage, K. Kawano, S. Oku, R. Iga, H. Okamoto and H. Takeuchi (NTT Photonics Laboratories, 3-1, Morinosato Wakamiya, Atsugi-shi, Kanagawa, 243-0198, Japan)

Y. Miyamoto (NTT Network Innovation Laboratories, 1-1, Hikarinooka, Yokosuka-shi, Kanagawa, 239-0847, Japan)

References

- 1 TAKEUCHI, H., TSUZUKI, K., SATO, K., YAMAMOTO, M., LTAYA, Y., SANO, A., YONEYAMA, M., and OTSUJI, T.: 'NRZ operation at 40 Gbit/s of a compact module containing an MQW electroabsorption modulator integrated with a DFB laser', *IEEE Photonics Technol. Lett.*, 1997, 9, (5), pp. 572-574
- 2 KAWANO, K., KOHTOKU, M., UEKI, M., ITO, T., KONDOH, S., NOGUCHI, Y., and HASUMI, Y.: 'Polarisation-insensitive travelling-wave electrode electroabsorption (TW-EA) modulator with bandwidth over 50 GHz and driving voltage less than 2 V', *Electron. Lett.*, 1997, 33, (18), pp. 1580-1581
- 3 ZHANG, S.Z., KAMAN, V., KEATING, A., CHIU, Y.J., ABRAHAM, R., and BOWERS, J.E.: '30 Gbit/s operation of a travelling-wave electroabsorption modulator'. Tech. Dig. OFC'99, 1999, Vol. 3, pp. 290-292

Microphotonic modulator for microwave receiver

D.A. Cohen, M. Hossein-Zadeh and A.F.J. Levi

Experimental results from a new microphotonic modulator with direct electrical-to-optical conversion are presented. The modulator consists of high- Q RF and microphotonic electro-optic resonators that are operated in simultaneous resonance. RF, optical, and time-domain results approach 100% optical modulation at gigahertz frequencies.

Recently a new microphotonic radio frequency (RF) receiver architecture with direct electrical-to-optical conversion was pro-

posed [1] for use at microwave frequencies and with potential applications for indoor wireless and micro-cell wireless systems [2]. This receiver uses high quality factor (Q) RF and microphotonic electro-optic resonators that are operated in simultaneous resonance. Central to such an architecture is the microphotonic optical modulator. This component directly converts the received RF carrier frequency to an optical carrier frequency by interaction of optical and RF electric fields via the electro-optic effect.

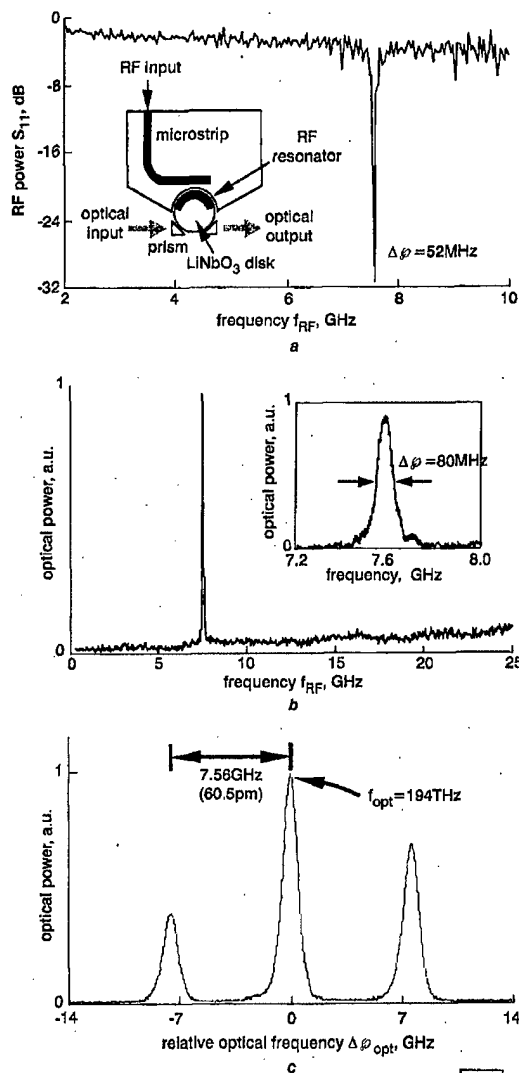


Fig. 1 Measured reflected RF power S_{11} , detected output optical power against input RF frequency and detected output optical power against optical frequency

- a Measured reflected RF power. Absorption $Q = 144$
 Inset: Geometry of side-coupled microstrip resonator
 b Detected output optical power against input frequency
 c Detected output optical power against optical frequency

An initial approach to develop a microphotonic optical modulator uses a z-cut LiNbO₃ disk-shaped resonator with optically-polished curved side-walls [3]. Standard evanescent prism-coupling [4] is used to couple laser light into and out of a resonant TE-polarised high- Q optical whispering-gallery mode (WGM) which exists at the periphery of the disk. A metal electrode structure fed by an RF signal is designed to overlap and be in simultaneous resonance with the optical field. The resonator's high optical Q is used to increase the effective interaction length of photons with an applied RF electric field. When combined with a simultaneously resonant RF structure designed to provide voltage gain between the electrodes, a highly sensitive receiver at microwave frequencies is achievable.

The free spectral range (FSR) of the optical resonator and the spatial pattern of the metal-electrode structure determine the centre modulation frequency of the optical carrier [2]. The frequency of the RF carrier f_{RF} should be an integral multiple m of the optical FSR such that $f_0 = 1/\tau_{disk} = n_{opt}2\pi R/c$ where τ_{disk} is the optical round-trip time of the disk and R is the disk radius. For a z-cut LiNbO₃ with $R = 2.92\text{mm}$, a value of $f_0 = 7.56\text{GHz}$ is measured.

The inset to Fig. 1a shows the RF and optical configuration. Prisms are used to couple laser light of approximate wavelength $\lambda = 1.55\mu\text{m}$ into and out of the WGM optical mode of the microphotonic resonator. The optical wavelength is tuned to a resonant wavelength of the optical resonator. An RF electric field propagating on a 50Ω metal microstrip line evanescently side-couples to a metal-electrode resonator on the LiNbO₃ disk. The fundamental resonant frequency of the electrode resonator is tuned to match the optical FSR of 7.56GHz , as indicated by the dip in the reflected RF excitation response shown in Fig. 1a. The measured voltage gain provided by this resonator is greater than 4. Improved resonator designs should be capable of achieving voltage gains in excess of 100. Fig. 1b shows the detected optical signal as a function of the applied RF frequency f_{RF} . The resulting optical modulation is centred at 7.56GHz with a -3dB bandwidth $\Delta f = 80\text{MHz}$.

RF modulation of the optical carrier is observed directly by passing light exiting the microphotonic resonator through a Fabry Perot interferometer with an optical resolution of $f_{3\text{dB}} = 900\text{MHz}$. As indicated in Fig. 1c, the optical carrier at 194THz ($\lambda = 1.55\mu\text{m}$) is centred between two optical side-bands, each separated by 7.56GHz ($\Delta\lambda = 60.5\text{pm}$) from the optical carrier. The input light has an optical bandwidth of $< 0.5\text{MHz}$.

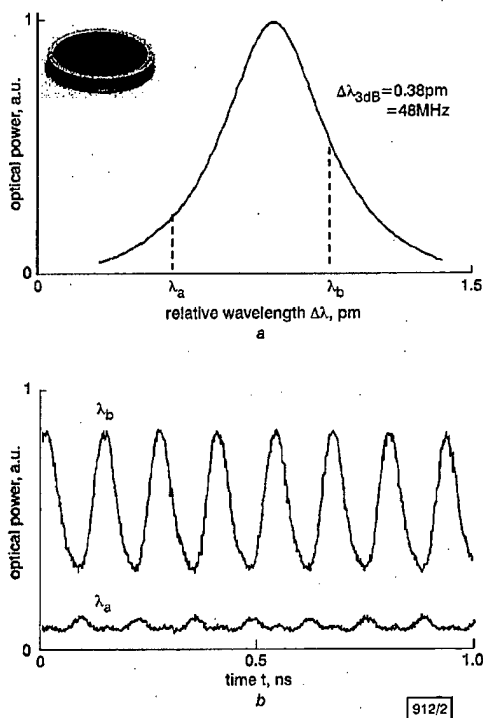


Fig. 2 Measured optical resonance and detected optical time-domain signal

a Measured optical resonance near $\lambda = 1.55\mu\text{m}$
Inset: z-cut LiNbO₃ resonator with optically polished curved side-walls. Gold electrodes are placed in an annulus around disk to increase overlap of electrical bias and optical field. $R = 2.92\text{mm}$, $d = 0.74\text{mm}$
b Detected optical time-domain signal

Fig. 2a shows the measured optical spectrum of the WGM resonance in the absence of RF modulation. Optical $Q = 4 \times 10^6$ results in an effective photon interaction length with an RF field of greater than 50cm . As shown in Fig. 2b, optical modulation is maximised for a fixed RF input power when the optical wavelength is located at the maximum slope of the WGM spectral shape.

Fig. 3 shows the modulated optical power at 7.6GHz for a fixed optical wavelength, where 1.0 equals 100% optical modulation. Small-signal modulation shows a linear increase with input RF voltage. At larger voltages, nearly 100% modulation is achieved. These voltages are found to be similar to values of V_π found in commercial LiNbO₃ Mach-Zehnder modulators. The minimum sensitivity in our initial experiments was found to be 90mV or $160\mu\text{W}$. A dramatic increase in RF sensitivity may be achieved by placing the metal electrodes closer to the optical WGM, improving the spatial overlap of the RF field with the optical mode, and increasing the Q of the RF resonator.

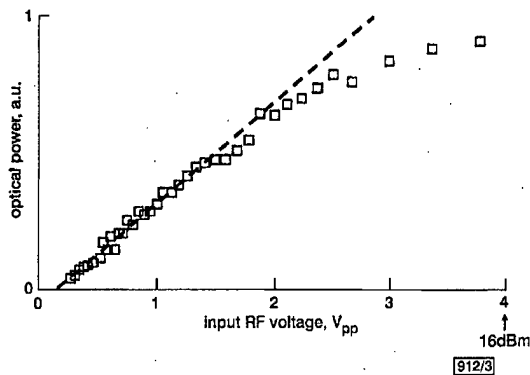


Fig. 3 Detected optical modulation against RF power launched onto RF microstrip resonator

Conclusion: A new type of electro-optic modulator using a z-cut LiNbO₃ disk-shaped resonator with optically-polished curved side-walls has been demonstrated. Initial experiments have achieved near 100% modulation at voltages comparable to Mach Zehnder modulators.

Acknowledgment: This work is supported in part by the National Science Foundation under contract ECS-9979331 and the DARPA RFLICs program.

© IEE 2001

18 December 2000

Electronics Letters Online No: 20010220

DOI: 10.1049/el:20010220

D.A. Cohen, M. Hossein-Zadeh and A.F.J. Levi (Department of Electrical Engineering, University of Southern California, Los Angeles, CA 90089-1111, USA)

References

- COHEN, D.A., and LEVI, A.F.J.: 'A microphotonic mm-wave receiver architecture', *Electron. Lett.*, 2001, **37**, (1), pp. 37-39
- OHATA, K., INOUE, T., FUNABASHI, M., INOUE, A., TAKIMOTO, Y., KUWABARA, T., SHINOZAKI, S., MARUHASHI, K., HOSAYA, K., and NAGAI, H.: 'Sixty-GHz-band ultra-miniature monolithic T/R modules for multimedia wireless communication systems', *IEEE Trans. Microw. Theory Tech.*, 1996, **44**, pp. 2354-2360
- COHEN, D.A., and LEVI, A.F.J.: 'Microphotonic components for a mm-wave receiver', accepted for publication in *Solid-State Electron.*
- TUEN, P.K., and ULRICH, R.: 'Theory of prism-film coupler and thin-film light guides', *J. Opt. Soc. Am.*, 1970, **60**, pp. 1325-1337

Fuzzy hyperline segment clustering neural network

U.V. Kulkarni, T.R. Sontakke and A.B. Kulkarni

A fuzzy hyperline segment clustering neural network (FHLSCNN) and its learning algorithm is proposed. This algorithm can learn ill-defined nonlinear cluster boundaries in a few passes and is suitable for on-line adaptation. The FHLSCNN is superior compared to the fuzzy min-max clustering neural network (FMN) proposed by Simpson.

been achieved by careful circuit design combined with recent advances in the SiGe bipolar technology.

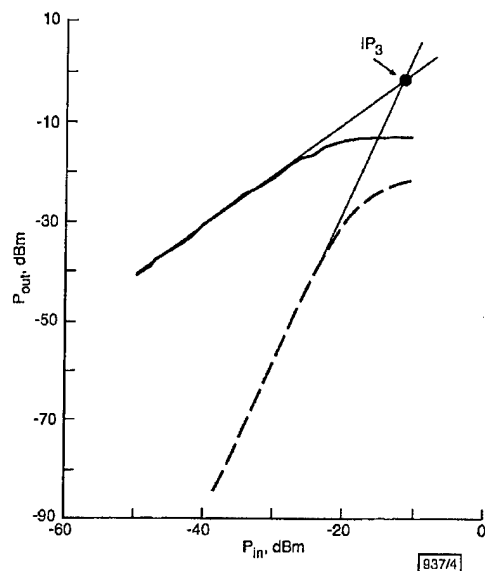


Fig. 4 Intermodulation performance at 20 GHz

$f_{RF1} = 20 \text{ GHz}$, $f_{RF2} = 20.001 \text{ GHz}$, $f_{LO} = 20.24 \text{ GHz}$, $P_{LO} = 0 \text{ dBm}$
 — P_1
 - - - P_3

Table 1: Summary of technical data

3dB bandwidth	20GHz
Conversion gain ($P_{LO} = 0 \text{ dBm}$)	13dB at 2GHz 10dB at 20GHz
Double-sideband noise figure	6dB at 20GHz
1dB compression point	-21dBm at 20GHz
Third-order intercept point	-11.3dBm at 20GHz
Supply voltage range	4.5–5.8V
Current (4.5V)	2mA
Power consumption (4.5V)	9mW
Chip size	$0.45 \times 0.45 \text{ mm}$
Technology	$0.5 \mu\text{m}/80 \text{ GHz } f_T \text{ SiGe}$

Conclusions: A monolithically integrated active broadband mixer for wireless communications in a $0.5 \mu\text{m}$ $80 \text{ GHz } f_T$ SiGe bipolar technology was presented. The mixer is optimised for a low-power and low-noise figure and operates with a conversion gain $> 10 \text{ dB}$ and up to 20 GHz . To our knowledge, this is the highest operating frequency for a monolithic mixer in a silicon-based technology.

© IEE 2001
 Electronics Letters Online No: 20010034
 DOI: 10.1049/el:20010034

S. Hackl, T.F. Meister, M. Wurzer, H. Knapp, K. Aufinger and L. Treitinger (Infineon Technologies AG, Corporate Research, Otto-Hahn-Ring 6, D-81730 Munich, Germany)

E-mail: sabine.hackl@infineon.com

A.L. Scholtz (Institute of Communications and Radio-Frequency Engineering, Vienna University of Technology, Gusshausstraße 25/389, A-1040 Vienna)

S. Hackl: Also with Institute of Communications and Radio-Frequency Engineering, Vienna University of Technology, Gusshausstraße 25/389, A-1040 Vienna

References

- DÖRR, W., ERBEN, U., SCHÖPPEN, A., DIETRICH, H., and SCHUMACHER, H.: 'Low-power low-noise active mixers for 5.7 and 11.2GHz using commercially available, SiGe HBT MMIC technology', *Electron. Lett.*, 1998, **34**, (21), pp. 1994–1996

- GLENN, J., CASE, M., HARAMI, D., MEYERSON, B., and POISSON, R.: '12-GHz Gilbert mixers using a manufacturable Si/SiGe epitaxial-base bipolar technology'. *IEEE Proc. Bipolar/BiCMOS Circuits Technol. Mtg.*, 1995, pp. 186–189
- OSAFUNE, K., and YAMAUCHI, Y.: '20GHz 5dB gain analog multipliers with Al-GaAs/GaAs HBTs'. *IEEE MTT Symp. Dig.*, 1991, pp. 1282–1285
- KOBAYASHI, K.W., GUTIERREZ-AITKEN, A., COWLES, J., TANG, B., DESROSIERS, R., MEDVEDEV, V., TRAN, L.T., BLOCK, T.R., OKI, A.K., and STREIT, D.C.: '15dB gain, DC-20GHz InP HBT balanced analog mixer and variable gain amplifier with 27dB of dynamic range'. *IEEE Radio Frequency Integrated Circuits Symp.*, 1999, pp. 105–108
- GILBERT, B.: 'The micromixer: a highly linear variant of the Gilbert mixer using a bisymmetric class-AB input stage', *IEEE J. Solid-State Circuits*, 1997, pp. 1412–1423
- MEISTER, T.F., SCHÄFER, H., FRANOSCH, M., MOIZER, W., AUFINGER, K., SCHULZ, U., WALZ, C., STOLZ, M., BOGUTH, S., and NÖCK, J.: 'SiGe base bipolar technology with 74GHz f_{max} and 11ps gate delay'. *IEEE IEDM Tech. Dig.*, 1995, pp. 739–742

Microphotonic millimetre-wave receiver architecture

D.A. Cohen and A.F.J. Levi

A new microphotonic millimetre-wave receiver architecture with direct electrical-to-optical conversion is presented. The receiver uses high-Q RF and microphotonic electro-optic resonators which are operated in simultaneous resonance. Numerical simulations indicate that efficient modulation of an optical carrier at RF in the millimetre-wave range can be realised.

Radio frequency (RF) receivers operating at millimetre-wave frequencies are of interest for indoor wireless and microcell wireless systems [1]. In this Letter, we propose a novel architecture for these wireless and front-end antenna applications. By exploiting the unique properties of a microphotonic modulator, efficient, low-power detection in a small volume can be achieved.

A microphotonic optical resonator is fabricated from an electro-optic material. The optical quality-factor (Q) of the resonator is high to increase the effective interaction length of photons with an applied RF electric field. When combined with a simultaneously resonant RF electrical feed for voltage gain and a patterned electrode structure, high-sensitivity at millimetre-wave frequencies is achievable.

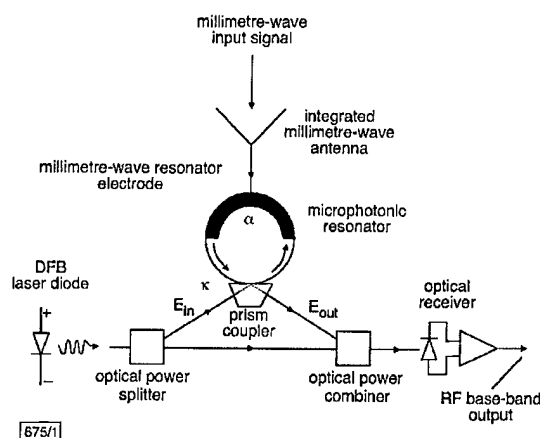


Fig. 1 Schematic diagram showing the receiver proposed for millimetre-wave RF detection

Fig. 1 is a schematic diagram showing the proposed receiver. An electromagnetic wave is received at a RF antenna integrated with the modulator. This millimetre-wave signal feeds the electrodes of the microphotonic resonator where the RF signal is directly converted via the electro-optic response of the modulator to a 200THz optical carrier frequency supplied by a distributed

feedback (DFB) laser. The resulting phase-modulated optical signal is converted to amplitude-modulation through the use of a standard Mach-Zehnder configuration. The intensity of the amplitude-modulated optical carrier is detected by the optical receiver which is sensitive only to baseband frequencies.

There are many practical configurations for the microphotonic modulator. One particular approach uses a z-cut LiNbO₃ disk-shaped resonator with optically polished curved sidewalls and optical refractive index $n_{opt} = 2.14$. Simultaneous resonance is achieved by confining a TE-polarised optical-field in a high-Q whispering-gallery mode along the periphery of the disk, while metal electrodes patterned above and below the disk ensure good overlap of the resonant RF and optical fields. Optical input and output may be achieved by means of standard evanescent prism-coupling with a power-coupling coefficient κ [2].

This optical resonator design can have Qs in excess of 4×10^6 , resulting in an effective photon interaction length with the RF field of $> 50\text{cm}$ for light of wavelength $1.5\mu\text{m}$. Although one sacrifices bandwidth with this resonant configuration, the effective photon interaction length is more than 25 times that of a conventional Mach-Zehnder LiNbO₃ modulator.

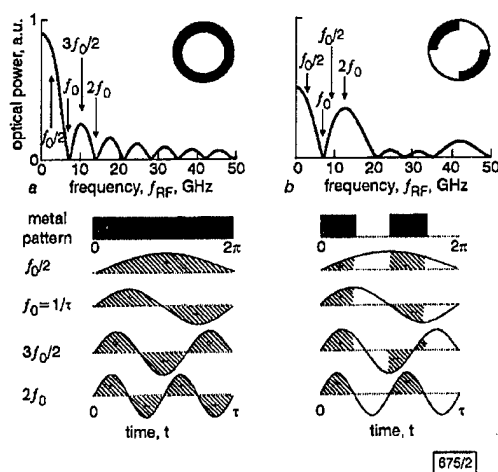


Fig. 2 Calculated response of microphotonic-based opto-electronic modulator with the indicated periodic metal-electrode structures, $f_0 = 7\text{GHz}$ and $\tau = 142\text{ps}$

a $R = 3.18\text{mm}$ LiNbO₃ disk modulator with $\kappa = 1$ and continuous ring-electrode
b $\kappa = 1$ optical-coupling with a split four-segment ring-electrode showing a peak in opto-electronic response at 14GHz

Frequency of operation is determined by the free spectral range (FSR) of the optical resonator and the spatial pattern of the metal-electrode structure. The frequency of the RF carrier f_{RF} should be an integral multiple m of the optical FSR such that $f_0 = 1/\tau_{disk} = n_{opt}2\pi R/c$ where τ_{disk} is the optical round-trip time of the disk and R is the disk radius. A periodic metal-electrode structure permits operation of the modulator well beyond a typically 20GHz -3dB roll-off of conventional commercial LiNbO₃ modulators. This is understood by first considering an ideal single optical-pass configuration ($\kappa = 1$). The modulation response of a solid-ring electrode is just that of a conventional Mach-Zehnder interferometer (Fig. 2a). We assume a radius $R = 3.18\text{mm}$ which gives a FSR of $f_0 = 7.03\text{GHz}$. As expected, the modulator has a sinc-function response with little efficiency at large values of f_{RF} . The first null in the frequency response is when the round-trip time of the optical wave τ_{disk} equals the period $T = 1/f_{RF}$. This occurs because during the positive part of the electric-field cycle of the RF, the optical field of the disk obtains a positive phase-shift ('+' in Fig. 2) which is exactly cancelled during the negative cycle ('-' in Fig. 2). Similarly, when the applied RF frequency is any integer multiple m of the optical round-trip frequency ($f_{RF} = m/\tau_{disk}$), a null in the frequency response results. Modulation can be enhanced at such a null if the electrode structure is modified as, for example, shown in Fig. 2b. In this case, while the RF electric-field at frequency $f_{RF} = 2f_0$ is positive, light passing through a region with an electrode receives a positive phase-shift. While the RF electric field is negative, the light passes through a region

without an electrode and receives no phase-shift. Results of calculations given in Fig. 2b show that the use of the patterned electrode enables efficient modulation near 14GHz . The loss in baseband efficiency, compared to the baseband response of the solid-ring electrode shown in Fig. 2a, is a result of only half the disk being patterned.

In its simplest form, the periodic electrode concept is designed for frequencies $f_{RF} = mf_0$, with a corresponding number of m equally spaced metal sections, each covering a fraction $1/2m$ of the circumference of the disk.

For the optically resonant case ($\kappa < 1$), the modulated optical electric field resulting from multiple round-trips is given by the expression

$$E_{out}(t) = \left[\sqrt{1-\kappa} E_{in}(t) - \frac{\kappa}{\sqrt{1-\kappa}} \sum_{j=1}^{\infty} r^j e^{-iF_n(t-j\tau_{disk})} E_{in}(t-j\tau_{disk}) \right] F_j(t-j\tau_{disk})$$

$$F_j(t-j\tau_{disk}) = \left[\sum_{k=0}^{j-1} \phi(t-k\tau_{disk}) \right]$$

where $E_{out}(t)$ is the electric field exiting the prism, $E_{in}(t)$ is the field entering the prism, n is the round-trip number, $r = \alpha^{1/2}(1-\kappa)^{1/2}$, α is the optical singlepass power transmission, and $\phi(t)$ is the optical singlepass phase-shift resulting from the applied RF field.

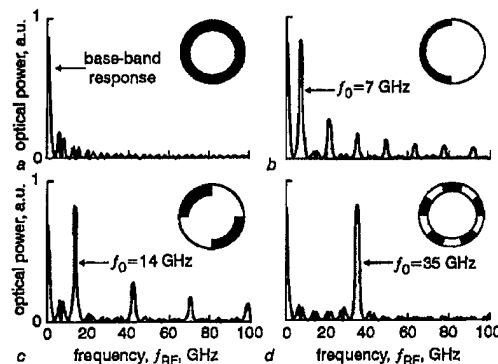


Fig. 3 Calculated response of microphotonic-based opto-electronic modulator with indicated periodic metal electrode structures

a $R = 3.18\text{mm}$ LiNbO₃ disk modulator with $\kappa = 0.5$ and continuous ring electrode
b $\kappa = 0.5$ with a split two-segment ring-electrode showing resonant opto-electronic response at 7GHz
c $\kappa = 0.5$ with four segments and response at 14GHz
d $\kappa = 0.5$ with 10 segments showing response at 35GHz

For the resonant solid-ring electrode, the high-Q results in a summation of multiple round-trips that further suppresses modulation efficiency. Figs. 3b and d show how a change in metal-electrode pattern shifts the resonant response to higher frequencies with little decrease in efficiency. This demonstrates that disk size, in itself, does not limit millimetre-wave operation.

The relative response at the resonant frequency compared to baseband is unity indicating the potential for efficient modulation. When integrated with a RF voltage resonator circuit attached to the antenna, the effective power gain of the receiver can be large.

In conclusion, a new type of millimetre-wave RF receiver architecture with direct electrical-to-optical conversion has been described. Numerical simulation of a microphotonic modulator which uses simultaneous resonance of optical and RF electric-fields has demonstrated that efficient modulation is achievable at millimetre-wave frequencies through the use of a periodic metal electrode.

Acknowledgment: This work is supported in part by the National Science Foundation under contract ECS-9979331 and the DARPA RFLICs program.

D.A. Cohen and A.F.J. Levi (Department of Electrical Engineering, University of Southern California, Los Angeles, California, 90089-1111, USA)

E-mail: alevi@usc.edu

References

- OHATA, K., INOUE, T., FUNABASHI, M., INOUE, A., TAKIMOTO, Y., KUWABARA, T., SHINOZAKI, S., MARUHASHI, K., HOSAYA, K., and NAGAI, H.: 'Sixty-GHz-band ultra-miniature monolithic T/R modules for multimedia wireless communication systems', *IEEE Trans. Microw. Theory Tech.*, 1996, **44**, pp. 2354-2360
- TIEN, P.K., and ULRICH, R.: 'Theory of prism-film coupler and thin-film light guides', *J. Opt. Soc. Am.*, 1970, **60**, pp. 1325-1337

Source-controlled channel decoding using nonbinary turbo codes

Zhaohui Cai, K.R. Subramanian and Liren Zhang

The residual redundancy contained in the source coding output symbols can be used by the channel decoder to provide extra error protection. A joint source/channel coding scheme which employs nonbinary turbo codes over rings to exploit the residual redundancy of source coding output is investigated. Simulation results on codebook-excited linear predictive coded speech and differential pulse code modulation coded image transmissions over noisy channels are presented.

Introduction: It has been shown that the residual redundancy contained in the output symbols of source coding can be used by (channel) turbo codes to provide further error protection in additive white Gaussian noise (AWGN) channels [1]. In [2] Sayood *et al.* suggest that the residual redundancy can be utilised more efficiently when source and channel encoder share an alphabet. In this Letter, we apply nonbinary turbo codes over ring Z_M to utilise the residual redundancy of source-coding outputs. Turbo codes are well known because they can achieve almost reliable communication at signal-to-noise ratios (SNR) very close to the Shannon-limit and there exists an iterative symbol-by-symbol maximum *a posteriori* probability (MAP) decoding scheme with moderate complexity [3]. The component codes of turbo codes, i.e. binary recursive systematic convolutional (RSC) codes, can be generalised to nonbinary codes over rings [4]. In this work we extend the source-controlled channel decoding to the nonbinary case and propose a modification of conventional MAP decoding schemes.

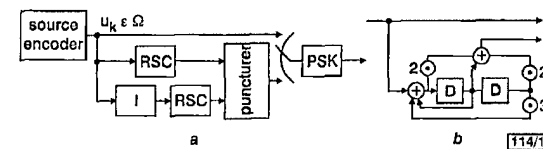


Fig. 1 Source/channel encoder and nonbinary RSC example

a Encoder
b Example

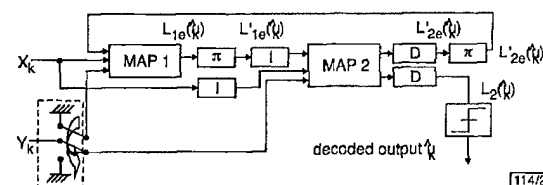


Fig. 2 MAP iterative decoding with knowledge of source statistics

System structure: The joint source/channel encoder is shown in Fig. 1. The source encoder delivers symbols from an alphabet $\Omega =$

$\{0, 1, \dots, M-1\}$, where M usually is a power of 2, i.e. $M = 2^m$. The source encoder is followed by a channel (turbo) encoder which consists of two parallel concatenated RSC component rings linked by a pseudorandom symbol interleaver. The source and channel encoders share the same alphabet. It has been shown in [4] that every rate $r = k/n$ convolutional code over ring $R = Z_M$ can be generated by some encoding matrix $G(D) \in R(D)^{k \times n}$, where $R(D)$ is the ring of rational functions over R . An example code over Z_4 is also shown in Fig. 1, which will be used in our simulation. The output of two RSC encoders are punctured alternatively to maintain the rate $r = 1/2$.

The simplest way to model the redundancy of source-coded symbols is the first-order Markov chain with symbol transition probability $P(u_k|u_{k-1})$. Usually we can get the transition probability statistics using some training sequence [2, 8]. The iterative MAP decoding algorithm was extended to nonbinary trellis codes in the appendix of [5]. To utilise the residual redundancy of source-coded symbols in the channel decoder, the conventional MAP decoding scheme must be modified. A simple modification is shown in Fig. 2. The structure of the decoder is similar to the conventional decoder proposed in [3], except for function modules π introduced between two MAP decoder modules. X_k and Y_k are AWGN corrupted information and parity check sequence, respectively. For every information symbol u_k , each MAP decoder i may deliver a soft output $L_i(u_k) := \ln(P_i(u_k|\text{observation}))$ as well as an extrinsic output $L_{ie}(u_k) := \ln(P_{ie}(u_k))$ which is used as *a priori* value in the subsequent iteration step [3]. For more information on notation here, and on how to decode binary/nonbinary turbo codes, refer to [3, 5]. In our scheme, $L_{ie}(u_k)$ is updated to $L_{ie}'(u_k)$ by module π in Fig. 2 before it is sent to the next MAP decoder as *a priori* estimation:

$$L_{ie}'(u_k) = \ln \left[\frac{1}{2} \left(P_{ie}(u_k) + \sum_{u_{k-1}} P(u_k|u_{k-1}) P_{ie}(u_{k-1}) \right) \right]$$

$k = 1, \dots, N-1 \quad i = 1, 2$

i.e. $P_{ie}'(u_k)$ is the source transition probability averaged version of $P_{ie}(u_k)$. N is the size of the 'average' interleaver. The input to the next MAP decoder is determined not only by $L_{ie}(u_k)$, the output of the current MAP decoder, but also by $P(u_k|u_{k-1})$, the first-order source characteristics. Simulation results show that quicker convergence of MAP decoding and higher fidelity of sources can be obtained through our proposed scheme.

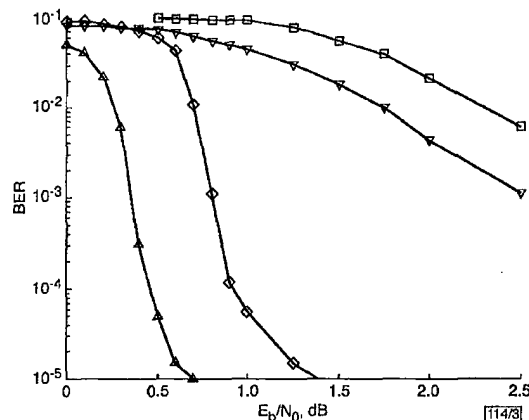


Fig. 3 BER performance of DPCM-coded image transmission over AWGN channel

□ — first iteration without source statistics
◇ — eighth iteration without source statistics
▽ — first iteration using proposed scheme
△ — sixth iteration using proposed scheme

Applications: First, we apply the proposed scheme to differential pulse code modulation (DPCM)-coded image transmission. The training and testing images are 512 × 512 GIRL and COUPLE, respectively. Lloyd-Max nonuniform quantiser with $M = 2^2$ levels is used in our simulation. The nonbinary RSC code is that with $G(D) = [1, (2 + D + 2D^2)/(1 + D + 3D^2)]$, which is shown in Fig. 1. The size of the interleaver is $N = 4096 \times 2 = 8192$ bits.



PERGAMON

Solid-State Electronics 45 (2001) 495–505

SOLID-STATE ELECTRONICS

Microphotonic components for a *mm*-wave receiver

D.A. Cohen, A.F.J. Levi *

Department of Electrical Engineering, University of Southern California, DRB 118, Los Angeles, California, CA 90089-1111, USA

Received 21 September 2000; accepted 3 November 2000

Abstract

A new microphotonic *mm*-wave receiver architecture with direct electrical-to-optical conversion is presented. The receiver uses high- Q RF and microphotonic electro-optic resonator components which are operated in simultaneous resonance. Initial results demonstrating modulation of an optical carrier at RF in the *mm*-wave range are reported. © 2001 Elsevier Science Ltd. All rights reserved.

Keywords: *mm*-wave receiver; LiNbO₃ modulator; Resonant detection; Microphotonic; Microdisk; Microsphere; Resonator

1. Introduction

RF receivers operating at *mm*-wave frequencies are of interest for indoor wireless and microcell wireless systems. Previous work has focused on the development and integration of all-electronic components to address these system needs [1]. Fig. 1 shows the basic building blocks of a conventional *mm*-wave electronic wireless receiver architecture consisting of an analog RF front-end and a digital signal-processing (DSP) module. Typically, most power is consumed in the analog monolithic microwave integrated circuit (MMIC). A state-of-the-art 60 GHz transmit/receive electronic analog RF front-end module developed by NEC consumes 1.2 W of which 0.4 W is used for the receiver [1]. Key components used by the NEC group are 0.15 μm gate-length AlGaAs/InGaAs heterojunction FETs with $f_{\text{max}} > 220$ GHz for electronic circuitry and a Ba-(Mg,Ta)O₃ dielectric resonator for a fixed-frequency, low-phase-noise, local oscillator (LO) used in the receiver module. Receiver functions include pass-band filtering, low-noise electronic amplification, down-conversion using an intermediate frequency oscillator, and low-pass filtering. The analog RF front-end of the re-

ceiver has a reported digital FSK data bandwidth of greater than 10 Mb/s (6 MHz equivalent analog bandwidth), sensitivity of 10 μW , and a volume of 900 mm³. This work represents the present state-of-the-art. Any improvement in performance which results in significantly reduced power consumption and size will probably require a completely new approach to system design.

2. A *mm*-wave microphotonic architecture

In this paper, we propose and present initial experimental results which use a novel, non-electronic, microphotonic architecture for these wireless applications. By exploiting the unique properties of a microphotonic modulator, efficient, low-power, all-optical detection in a small volume can be achieved. Fig. 2 is a schematic of the proposed architecture. An electromagnetic wave is received at a RF antenna integrated with the modulator. This *mm*-wave signal feeds the electrodes of the microphotonic resonator where the RF signal is directly converted via the electro-optic response of the modulator to a 200 THz optical carrier frequency supplied by a distributed feedback (DFB) laser. The resulting phase-modulated optical signal is converted to amplitude-modulation through the use of a standard Mach-Zehnder configuration. After all-optical-signal processing, which may include filtering to suppress the

* Corresponding author. Tel.: +1-213-740-7318; fax: +1-213-740-9280.

E-mail address: alevi@usc.edu (A.F.J. Levi).

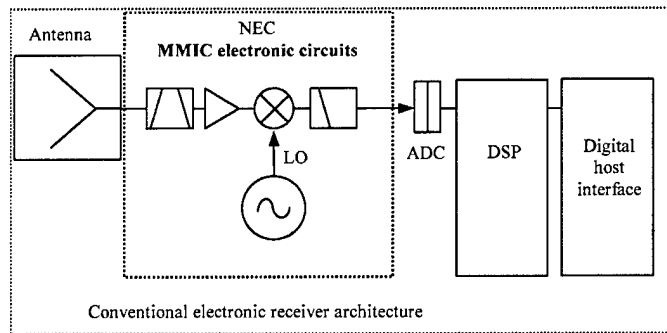


Fig. 1. Schematic of basic conventional wireless receiver architecture consisting of analog electronic circuitry in MMIC modules and a DSP module. An electromagnetic wave received at a RF antenna is pass-band filtered, amplified, and fed to a mixer. A LO also feeds the mixer whose output is filtered to obtain base-band.

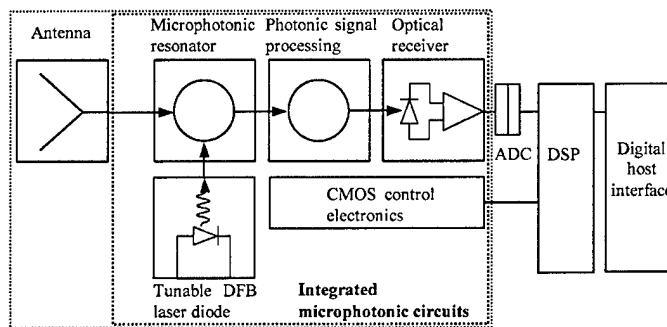


Fig. 2. Insertion of *mm*-wave microphotonic device technologies in future broad band heterodyne wireless architectures. An electromagnetic wave received at a RF antenna feeds electrodes of the microphotonic modulator. The modulator directly converts the RF signal to an optical carrier via the electro-optic effect. The resulting phase-modulated optical signal is converted to amplitude-modulation through the use of a standard Mach-Zehnder configuration. After conversion to the optical domain, the signal is processed using all-optical techniques before down-converting to base-band at the pin photodetector.

optical carrier, the intensity of the amplitude-modulated optical carrier is detected by the optical receiver which is sensitive only to base-band frequencies.

A microphotonic optical resonator is fabricated from an electro-optic material. The resonator's optical quality-factor, Q , is high to increase the effective interaction length of photons with an applied RF electric field. When combined with a simultaneously resonant RF electrical feed for voltage gain and a patterned electrode structure, high-sensitivity at *mm*-wave frequencies is achievable.

Fig. 3 illustrates the RF electric field spectrum as the signal progresses through the microphotonic architecture. The received RF electric field at the antenna is composed of a *mm*-wave carrier frequency, f_{RF} , with modulation side bands (shown in the figure using amplitude modulation (AM) as an example). The RF electric field modulates the optical field which is resonant within the electro-optic microphotonic resonator. As will be shown, if the RF carrier is a multiple of the

FSR of the optical cavity, the optical field in the cavity will be modulated efficiently at the RF carrier frequency. If the base-band modulation falls within the optical Q of the photonic resonator, the detected optical spectrum will consist of an optical carrier frequency, Ω_{opt} , optical sub-carrier frequencies $\Omega_{opt} \pm f_{RF}$, and optical base-band modulation about each sub-carrier frequency. The incident RF signal has thereby been converted from a RF carrier frequency to an optical carrier frequency. This modulated light may then be carrier suppressed by a passive optical filter and detected at the optical receiver. The low-pass frequency response of the optical receiver is used to detect and filter the base-band signal.

3. LiNbO₃ microphotonic resonator

There are many practical configurations for the microphotonic modulator. One particular approach uses a *z*-cut LiNbO₃ disk-shaped resonator with optically-

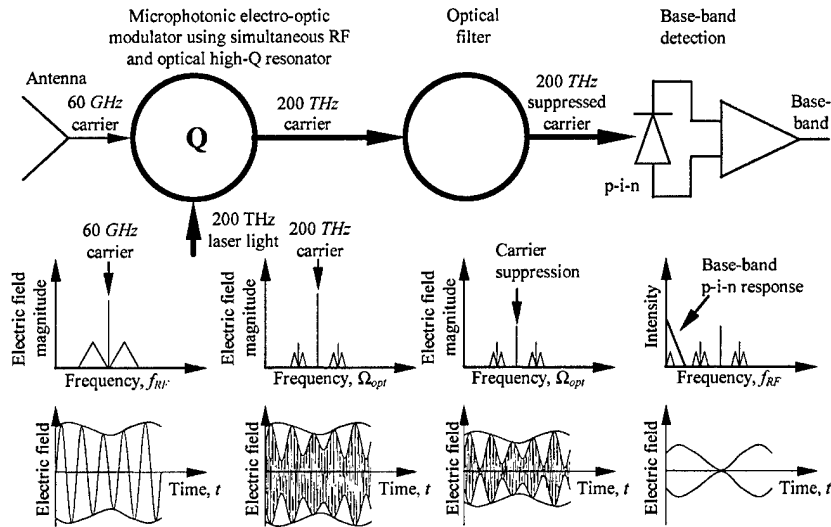


Fig. 3. A graphic showing the electric field spectrum as the signal progresses through the microphotonic architecture. A received *mm*-wave carrier frequency with AM side-bands modulates the optical field which is resonant within the electro-optic microphotonic resonator. The incident RF signal is converted from a RF carrier frequency to an optical carrier frequency. The detected optical spectrum consists of an optical carrier frequency, Ω_{opt} , optical sub-carrier frequencies $\Omega_{opt} \pm f_{RF}$, and optical base-band modulation about each sub-carrier frequency. This modulated light may then be carrier suppressed and detected at the optical receiver. The low-pass frequency response of the optical receiver is used to detect and filter the base-band signal.

polished curved side walls. The components are fabricated from the LiNbO_3 material system because of its high electro-optic coefficient, and its low loss at both optical and RF frequencies. LiNbO_3 is a negative uniaxial crystal with trigonal 3m crystal symmetry. The index of refraction along the extraordinary axis (*z*-axis) is $n_{opt} = 2.14$, at an optical wavelength $\lambda = 1.5 \mu\text{m}$, and greater than $5.1 \mu\text{m}$ at RF frequencies in the *mm*-wave regime [2,3].

Simultaneous resonance between optical and RF fields is possible inside the disk. Such resonance is achieved by confining a TE-polarized optical-field in a high-*Q* whispering-gallery mode (WGM) along the periphery of the disk, while metal electrodes feed RF power from a resonant electrical circuit. These metal electrodes are patterned above and below the equator of the disk to ensure good overlap of the resonant RF and optical fields. Optical input and output may be achieved by means of standard evanescent prism coupling with a power coupling coefficient κ [4]. Fig. 4 shows the schematic detail of this proposed receiver. An electromagnetic wave is received at a RF antenna integrated with the modulator. This *mm*-wave signal feeds the electrodes of the microphotonic resonator where the RF signal is directly converted via the electro-optic response of the modulator to a 200 THz optical carrier frequency supplied by a DFB laser. The resulting phase-modulated optical signal is converted to amplitude-modulation through use of a standard Mach-Zehnder configuration.

The intensity of the amplitude-modulated optical carrier is detected using an optical receiver whose response is sensitive only to base-band frequencies.

The microphotonic disk resonator can achieve optical *Q*s in excess of 4×10^6 resulting in an effective photon interaction length with the RF field of greater than 0.5 m for light of wavelength $1.5 \mu\text{m}$. Although one sacrifices bandwidth with this resonant configuration, the effective photon interaction length, and hence voltage sensitivity, is more than 25 times that of a conventional Mach-Zehnder LiNbO_3 modulator.

3.1. Microphotonic optical resonator fabrication

Disk resonator geometry and polishing technique play an important role in determining optical *Q* and optical coupling. As shown in Fig. 5(a), the basic geometry of the LiNbO_3 resonator is a disk of radius *R*, where $1 \text{ mm} \leq R \leq 3 \text{ mm}$, and thickness *d*, where $0.2 \text{ mm} \leq d \leq 1 \text{ mm}$ for devices presently under test. The side wall of the disk is optically polished with a radius of curvature, *R'*, typically equal to the radius of the disk. The equator of the disk's curved side wall should be accurately maintained at height $d/2$.

While polishing optically flat surfaces with LiNbO_3 is a routine industrial procedure, polishing curved side walls to an optical finish in LiNbO_3 is not a standard practice. Fig. 5(b) is a photograph of a $R = 2 \text{ mm}$,

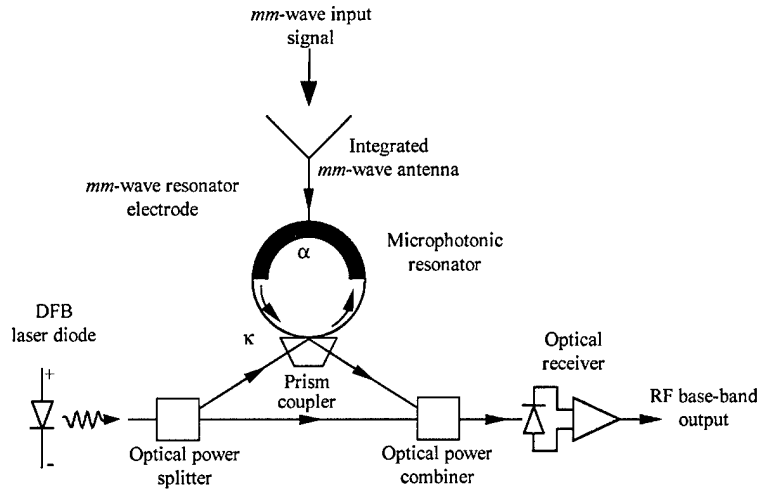


Fig. 4. Schematic detail of a microphotonic-based *mm*-wave RF detector. An electromagnetic wave received at a RF antenna feeds electrodes of the microphotonic modulator. The modulator directly converts the RF signal to an optical carrier via the electro-optic effect. The resulting phase-modulated optical signal is converted to amplitude-modulation through the use of a standard Mach-Zehnder configuration.

$d = 3.6$ mm disk which clearly shows the optically polished curved side walls of the disk. Fig 5(c) shows a smaller $R = 1$ mm, $d = 200$ μ m thick z-cut LiNbO₃ disk prior to metalization. As will be discussed later, optical Q in excess of 4×10^6 near $\lambda = 1550$ nm wavelength is measured in high quality disks.

3.2. Optical coupling to the resonator

A significant challenge in the development of an optical resonator based system is zero-loss coupling of optical power both into and out of the resonator. This must be achieved to reduce coupling losses that are inherent in other systems such as conventional Mach-Zehnder LiNbO₃ modulators. Optical WGMs cannot be excited directly by simple propagating beams. Instead, coupling is achieved through indirect excitation of the WGMs using evanescent fields. There are numerous methods for evanescent coupling of light into guided modes, however prism coupling is particularly convenient because of the large refractive index of LiNbO₃. Basic prism-coupled optical configurations are shown schematically in Fig. 6.

The mechanism for coupling between prisms of index n_{prism} and disks with index n_{opt} is that of frustrated total internal reflection. The prominent component of the propagation constant $\beta_{n/m}$ for WGMs lies along the annulus of the disk for the high- Q modes we are interested in exciting [5,6]. To phase match with these modes, the angle of incidence of light with respect to the normal of the coupling face should be at an angle greater than or equal to $\theta = \arcsin(n_{\text{opt}}/n_{\text{prism}})$. This is fundamentally a result of Snell's law and results in the requirement that

$n_{\text{prism}} \geq n_{\text{opt}}$. This may be satisfied using diamond prisms of refractive index 2.4. Use of such prisms initially provided a total 25% optical coupling efficiency in the two-prism coupling scheme shown schematically in Fig. 6(b). Fig. 7(a) is a photograph of a prism coupler placed next to a LiNbO₃ disk viewed from above. The side view in Fig. 7(b) shows scattered laser light on only the right side of the disk periphery (the bright spots on the left side are prism reflections) which is consistent with a traveling wave excitation of the disk.

3.3. Optical spectrum of the microphotonic resonator

When TE-polarized WGMs are excited within the LiNbO₃ microphotonic resonator the detected optical spectrum shows peaks corresponding to the free spectral range (FSR) of the resonant cavity. This FSR is defined as $\Delta f_{\text{FSR}} \approx c/(n_{\text{opt}} 2\pi R)$. It should be noted that $1/\Delta f_{\text{FSR}}$ is equal to the round trip time of the cavity $\tau_{\text{disk}} = (n 2\pi R)/c$. Fig. 8(a) shows a typical experimental result using the two-prism coupling scheme and a tunable DFB laser to scan the entire FSR of the disk. A disk of diameter $2R = 5.85$ mm, and thickness $d = 0.7$ mm exhibited a FSR of 7.57 GHz (60.6 pm) for TE optical modes. Within the uncertainty of the measured disk radius, these values agree with the equation for Δf_{FSR} .

3.4. Optical losses, and the quality factor, Q

Optical losses and photon lifetime of the resonator can be extrapolated from the quality factor Q . The quality factor is defined as $Q \equiv \Omega E/P = f/\Delta f_{\text{FWHM}} = \lambda/\Delta \lambda_{\text{FWHM}} = \Omega \tau_c$, where $\Omega = 2\pi f$, E is the energy stored

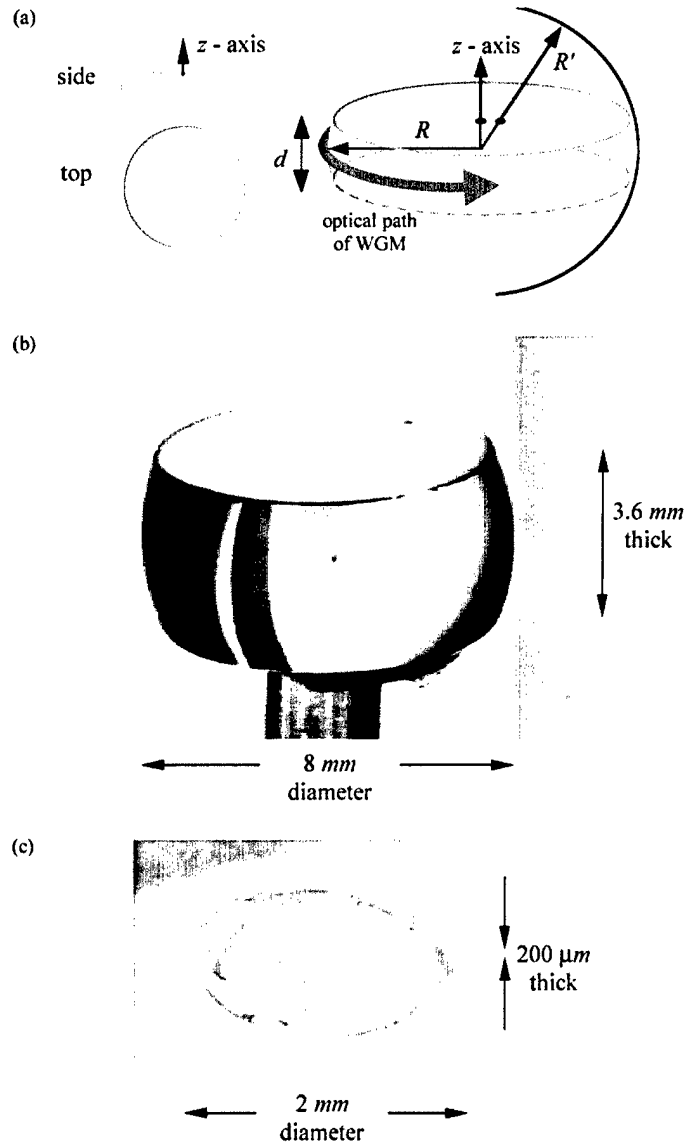


Fig. 5. (a) Sketch of the geometry of a microdisk indicating disk radius R , disk thickness d and curved side walls with radius of curvature R' . (b) Photograph of a small z-cut LiNbO_3 disk-shaped resonator. The size of the disk is indicated. (c) Photograph of a large z-cut LiNbO_3 disk-shaped resonator with solid-gold top and bottom flat electrodes and optically-polished curved side walls. The size of the disk is indicated.

in the resonant mode, P is the power dissipated in the cavity, Δf_{FWHM} is the full-width at half maximum of the spectral peak at optical frequency f , and τ_c is the $1/e$ photon lifetime. The measured optical Q of a LiNbO_3 disk with diameter 5.85 mm is shown in Fig. 8(b). This mode was measured using the two-prism coupling scheme and a wavelength tunable DFB laser input with linewidth < 0.5 MHz.

The total measured optical Q including the effects of coupler loading is greater than 4×10^6 near $\lambda = 1550$ nm

wavelength and $\lambda f_{\text{FWHM}} = 48$ MHz. We find for this Q , the photon cavity lifetime is $\tau_c = 3.4$ ns. The effective number of round trips per photon from $c\tau_c/n_{\text{opt}}2\pi R$ is approximately 26. Assuming the Q is dominated by optical scattering at the disk edge, we define a distributed loss constant α as the loss per unit length, where $\alpha = n_{\text{opt}}/(c\tau_c) = 0.02 \text{ cm}^{-1}$. This is 10–100 times better than typical waveguide scattering in semiconductors, and demonstrates an ability to obtain a high-quality, low-loss optical polish.

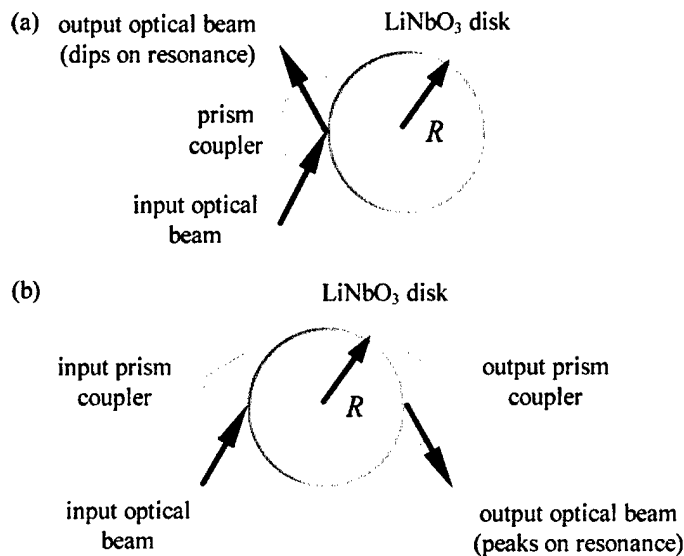


Fig. 6. Sketch showing (a) single prism coupling and (b) two prism coupling of the optical field to the microphotonic resonator.

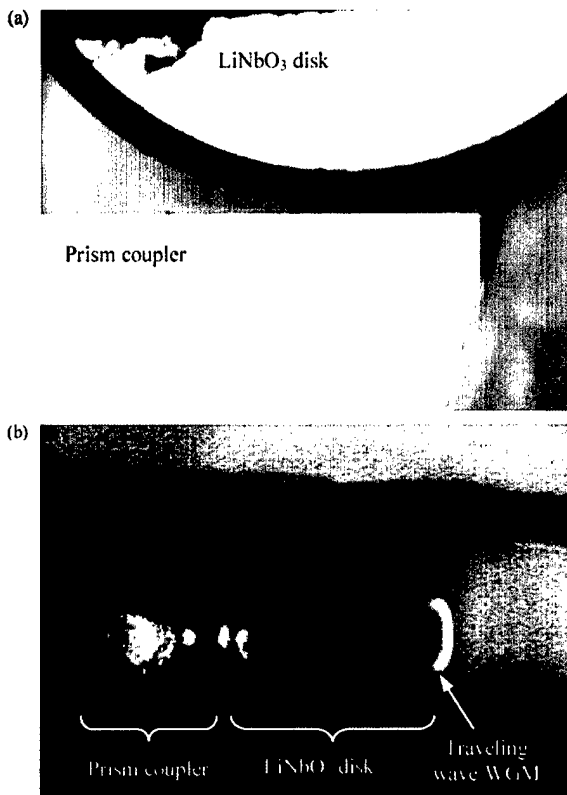


Fig. 7. (a) Photograph of LiNbO₃ disk and prism-coupler viewed from above. (b) Infrared side view of disk resonator and prism showing optical coupling at $\lambda = 1550$ nm wavelength. Coupled laser light on the disk periphery is indicated by the arrow.

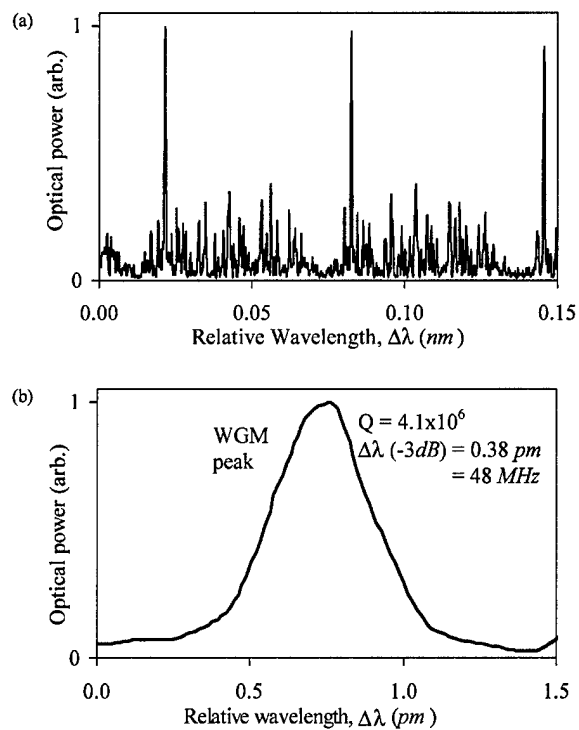


Fig. 8. (a) Measured optical spectrum of a z-cut LiNbO₃ disk-shaped resonator. The peaks in the spectrum correspond to WGM of the disk. (b) Measured optical resonance near wavelength $\lambda = 1550$ nm of a z-cut LiNbO₃ disk-shaped resonator with gold electrodes and optically polished curved side walls. The measured Q of this device is in excess of 4×10^6 .

4. Static electro-optic response of the LiNbO₃ microphotonic modulator

4.1. Electrical coupling to the microphotonic resonator using metal electrodes

One method to couple the electric field detected at the RF antenna to the microphotonic modulator is to pattern metal electrodes onto the LiNbO₃ disk. These electrodes may be part of a resonant RF circuit used to amplify the RF electric field, thereby increasing optical modulation. Since the WGM nature of the optical field strongly confines light to the edge of the disk, the electrodes can be patterned to significantly overlap the optical and electromagnetic fields inside the disk. Optimizing the overlap improves RF field sensitivity. Fig. 9(a) is a photograph of a thin z-cut LiNbO₃ disk-shaped resonator with optically polished curved side walls and gold electrodes placed in an annulus around the disk to increase the overlap of RF and optical fields. In addition, the RF electric field on the metal electrodes of the disk interacts with photons via the electro-optic effect and not a resistive electrical load. Consequently no damping of the RF Q due to a load resistor occurs for the LiNbO₃ disk. This is an inherent property of the

optical isolation provided by use of a LiNbO₃ resonator in the system.

4.2. DC voltage response

Ideally, the electro-optic effect in z-cut LiNbO₃ changes only the optical refractive index of the medium as a function of time, $n(t)$. For time $t > 0$ the resonant frequency of light in the cavity changes adiabatically as the index of refraction changes, $f(t) \sim f_0 n_0 / n(t)$, where f_0 is the unperturbed resonant frequency at time $t \leq 0$ and n_0 is the refractive index at time $t \leq 0$. Application of a DC voltage V_{DC} along the crystal's z-axis will shift the WGM resonant wavelength $\lambda_0 = 2\pi c / \Omega_0$ due to a change of refractive index Δn_{opt} . If the applied DC electric field is $E_{DC} = V_{DC} / d$, where d is the thickness of the disk, the electro-optic effect changes the refractive index along the z-axis by $\Delta n_{opt} = n_e^3 r(33) E_{DC} / 2$, where $r(33) \sim 30.8 \times 10^{-12}$ m/V s at an optical wavelength $\lambda = 1.55$ μ m. Given that m_{opt} is approximately the number of optical wavelengths along the disk circumference, from $m_{opt} \lambda = n_{opt} 2\pi R$, the shift of the WGM resonant wavelength by a DC electric field is $\Delta \lambda_{DC} = 2\pi R \Delta n_{opt} / m_{opt}$.

To demonstrate electrically controlled optical resonance tuning in a microphotonic disk, an electric field is applied perpendicular to the top disk face (parallel to the z-axis). This was accomplished by applying a DC voltage to a metal ring on a LiNbO₃ resonator similar to that shown in Fig. 9(a). As shown in Fig. 9(b), a TE-polarized mode may be tuned 70 MHz (0.56 pm) with an applied DC electric field of 10.8 V/mm.

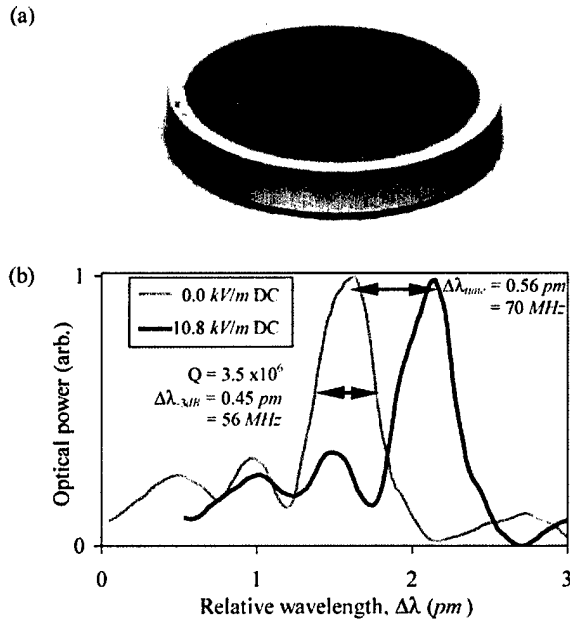


Fig. 9. (a) Photograph of a z-cut LiNbO₃ disk-shaped resonator with optically polished curved side walls. Gold electrodes are placed in an annulus around the disk to increase the overlap of electrical bias and optical fields. The dimensions of the disk are radius $R = 5.8$ mm and thickness $d = 0.74$ mm. (b) Measured shift in resonant wavelength due to application of 8 V DC bias between the top and bottom electrodes of the disk shown in (a). The change in resonant wavelength is 0.07 pm/V.

5. RF electro-optic modulation using a microphotonic resonator

5.1. The patterned metal electrode structure

RF modulation frequency of the microphotonic resonator is determined by the FSR of the optical resonator and the spatial pattern of the metal electrode structure. The frequency of the RF carrier f_{RF} should be an integral multiple m of the optical FSR, f_{FSR} , where $f_{FSR} = 1 / \tau_{disk} = c / n_{opt} 2\pi R$, τ_{disk} is the optical round-trip time of the disk, and R is the disk radius [7]. A periodic metal electrode structure permits operation of the modulator well beyond a typically 20 GHz –3 dB roll-off of conventional commercial LiNbO₃ modulators. This is understood by first considering an ideal single optical-pass configuration ($\kappa = 1$). The modulation response of a solid-ring electrode is just that of a conventional Mach–Zehnder interferometer (Fig. 10(a)). We assume a radius $R = 3.18$ mm which gives a FSR of $f_{FSR} = 7.03$ GHz. As expected, the modulator has a sinc function response with little efficiency at large values of f_{RF} . The

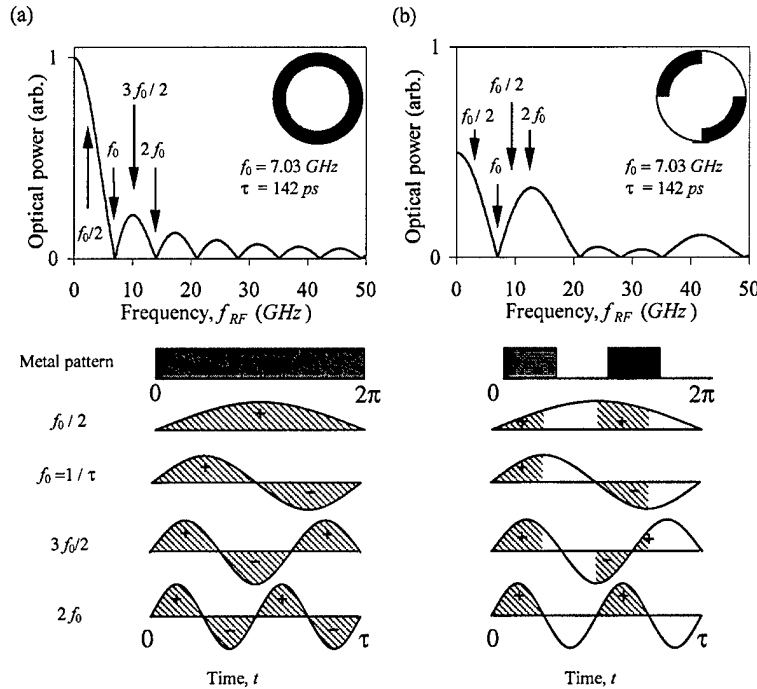


Fig. 10. Calculated response of a microphotonic-based opto-electronic modulator with the indicated periodic metal-electrode structures and $f_{\text{FSR}} = 7$ GHz. (a) A $R = 3.18$ mm LiNbO₃ disk modulator with $\kappa = 1$ and a continuous ring-electrode. (b) $\kappa = 1$ optical coupling with a split 4-segment ring-electrode showing a peak in opto-electronic response at 14 GHz.

first null in the frequency response is when the round-trip time of the optical wave τ_{disk} equals the period $T = 1/f_{\text{RF}}$. This occurs because during the positive part of the RF electric field's cycle, the disk's optical field obtains a positive phase-shift ("+" in Fig. 10(a)) which is exactly canceled during the negative cycle ("–" in Fig. 10(a)). Similarly, when the applied RF frequency is any integer multiple m of the optical round-trip frequency ($f_{\text{RF}} = m/\tau_{\text{disk}}$), a null in the frequency response results. Modulation may be enhanced at such a null if the electrode structure is modified as, for example, shown in Fig. 10(b). In this case, while the RF electric field at frequency $f_{\text{RF}} = 2f_{\text{FSR}}$ is positive, light passing through a region with an electrode receives a positive phase-shift. While the RF electric field is negative, the light passes through a region without an electrode and receives no phase-shift. Results of calculations given in Fig. 10(b) show that use of such a patterned two-electrode structure enables efficient modulation near 14 GHz. The loss in base-band efficiency in Fig. 10(b) compared to the ring electrode of Fig 10(a) is a result of only half the disk being patterned. In addition, the relative response at the resonant frequency compared to base-band is 0.63 indicating the potential for efficient modulation. A larger modulation response at base-band results because a photon will encounter a larger average electric field during a single round trip. This is because the time constant determining this response is the round trip time

$\tau_{\text{disk}} = 1/f_{\text{FSR}}$ of the disk. If the applied RF frequency, f_{RF} is much less than f_{FSR} , a photon will make many round trips within one frequency cycle time $1/f_{\text{RF}}$, and thereby encounters a relatively uniform RF field. At higher frequencies, a photon will encounter a varying RF field during a single round trip, reducing the average electric field seen.

For the optically resonant case ($\kappa < 1$), the modulated optical electric field resulting from multiple round-trips may be obtained from the expressions

$$E_{\text{out}}(t) = \left[\sqrt{(1-\kappa)} E_{\text{in}}(t) - \frac{\kappa}{\sqrt{(1-\kappa)}} \sum_{n=1}^{\infty} r^n e^{-jF_n(t-n\tau_{\text{disk}})} E_{\text{in}}(t-n\tau_{\text{disk}}) \right]$$

$$F_n(t-n\tau_{\text{disk}}) = \left[\sum_{i=0}^{n-1} \phi(t-i\tau_{\text{disk}}) \right]$$

where $E_{\text{out}}(t)$ is the electric field exiting the prism, $E_{\text{in}}(t)$ is the field entering the prism, n is the round trip number, $r = \alpha^{1/2}(1-\kappa)^{1/2}$, α is the optical single-pass power transmission, and $\phi(t)$ is the optical single-pass phase-shift resulting from the applied RF field. The above equation simplifies when the applied RF electric field

frequency is the same as the optical FSR of the disk ($f_{RF} = 1/\tau_{disk}$). In this case, the expression becomes

$$E_{out}(t) = \left[\sqrt{1-\kappa} - \frac{\kappa}{\sqrt{1-\kappa}} \frac{\rho e^{-j\phi(t)}}{1 - \rho e^{-j\phi(t)}} \right] E_i(t)$$

where $\rho = r \exp(\Omega_{opt} \tau_{disk})$, and Ω_{opt} is the optical frequency.

As shown in Fig. 11(a) for the resonant solid-ring electrode, high optical-Q results in a summation of multiple round-trips that further suppresses modulation

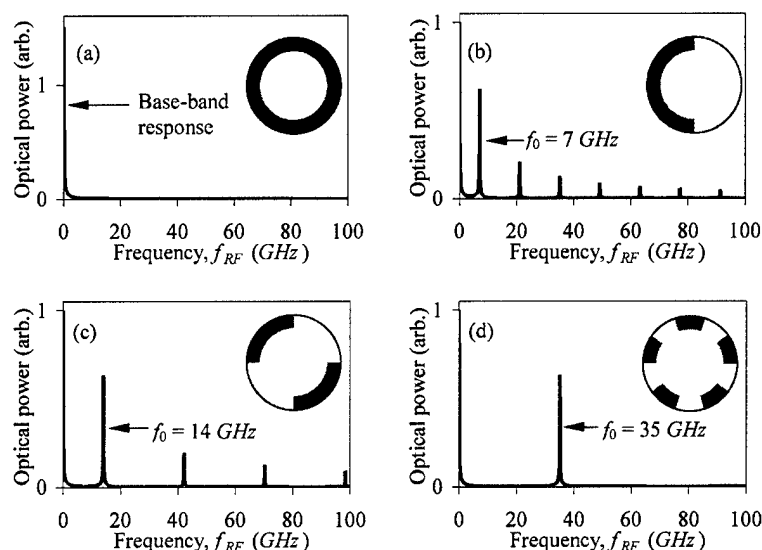


Fig. 11. Calculated response of a microphotonic-based opto-electronic modulator with the indicated periodic metal electrode structures. (a) $R = 3.18$ mm LiNbO₃ disk modulator with $\kappa = 0.05$ and a continuous ring electrode. (b) $\kappa = 0.05$ with a split 2-segment ring-electrode showing resonant opto-electronic response at 7 GHz. (c) $\kappa = 0.05$ with 4 segments and response at 14 GHz. (d) $\kappa = 0.05$ with 10 segments showing response at 35 GHz.

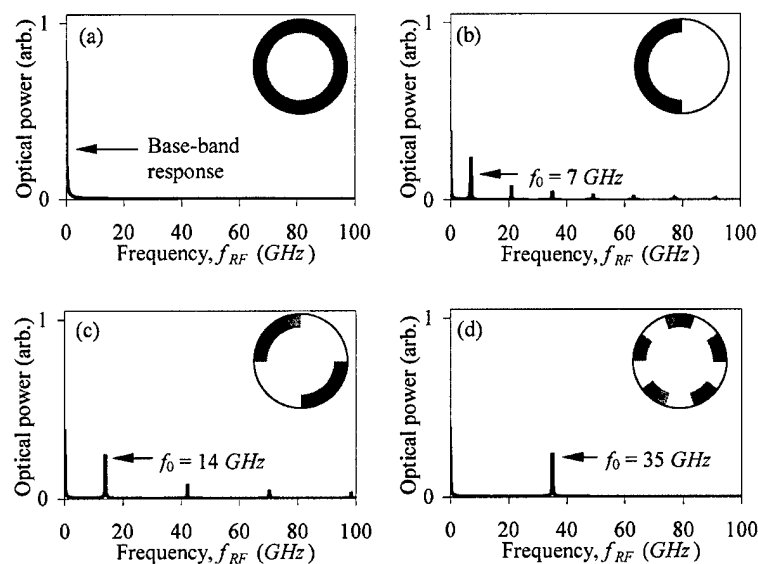


Fig. 12. Calculated response of a microphotonic-based opto-electronic modulator with the indicated periodic metal electrode structures and finite scattering coefficient $\alpha = 0.01$ cm⁻¹. (a) $R = 3.18$ mm LiNbO₃ disk modulator with $\kappa = 0.05$ and a continuous ring electrode. (b) $\kappa = 0.05$ with a split 2-segment ring-electrode showing resonant opto-electronic response at 7 GHz. (c) $\kappa = 0.05$ with 4 segments and response at 14 GHz. (d) $\kappa = 0.05$ with 10 segments showing response at 35 GHz.

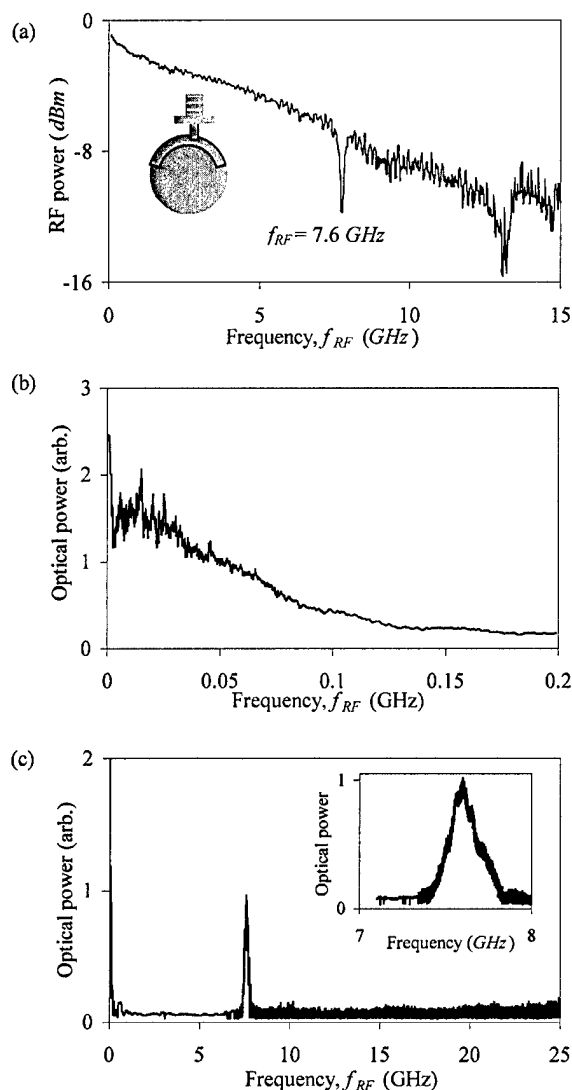


Fig. 13. Measured results showing optical modulation of a 5.8 mm diameter, 0.74 mm thick LiNbO₃ microphotonic modulator at 7 GHz. (a) The reflected swept RF excitation resonance of the resonant electrode structure show in the inset. (b) Detected optical response at base-band frequencies versus a swept RF input. (c) Detected optical response versus a swept RF input. The resulting modulation peak is at 7.6 GHz with a measured bandwidth of 150 MHz.

efficiency at finite frequency. Fig. 11(b)–(d) illustrate how a change in the metal electrode pattern shifts the resonant frequency to higher frequencies with little decrease in efficiency. This demonstrates that disk size, in itself, does not limit *mm*-wave operation.

Fig. 12 shows the simulated response for a finite-round trip electric field loss α of the disk. A distributed value of $\alpha = 0.01$ cm⁻¹ is typical for the experimental results presented in this paper. The modulation effi-

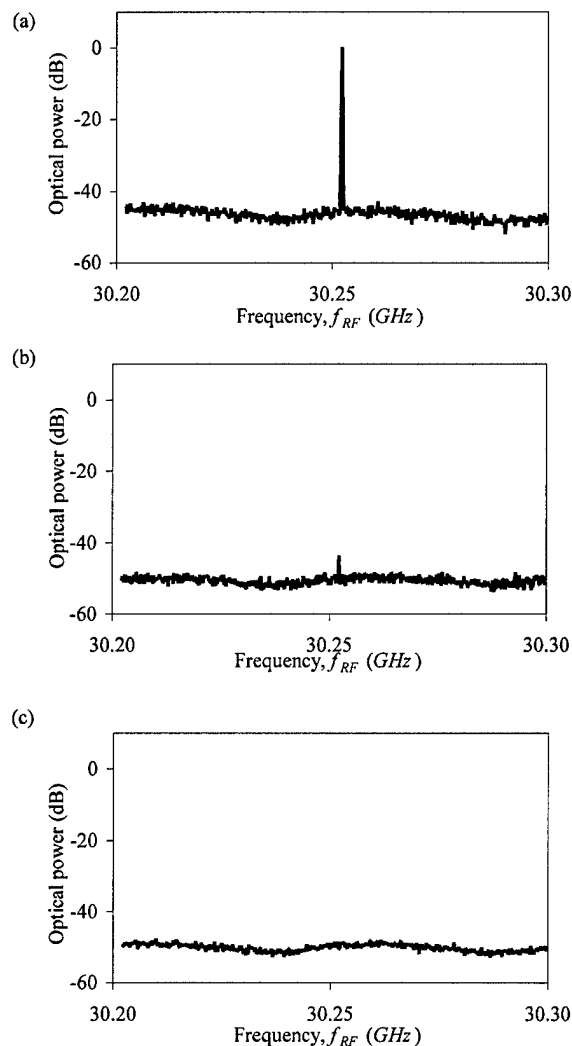


Fig. 14. (a) Measured results showing optical modulation of a 5.8 mm diameter, 0.74 mm thick LiNbO₃ microphotonic modulator at 30.25 GHz for a CW RF input. (b) Detected optical response when the optical wavelength is tuned off the optical resonance. (c) Detected optical response when the applied RF field is tuned off the RF resonant frequency.

ciency of the lossy resonant case at large RF frequency is found to be about 25% that of the zero-loss base-band modulation shown in Fig. 11. This is a combination of the 0.63 resonant frequency to base-band efficiency, and finite α loss. A factor of two improvement in modulation efficiency is achievable by patterning electrodes in a differential (push-pull) configuration. Unpatterned regions of the disks shown in Fig. 11 could be patterned and fed by a π phase-shifted RF field. This converts the negative phase-shift incurred during the negative cycle of the RF field to a positive phase shift, thereby doubling the optical modulation efficiency.

5.2. Experimental results of RF modulation

To confirm our simulations, we show experimental results in Fig. 13. Light of wavelength $1.55\ \mu\text{m}$ is coupled into a $2R = 5.8\ \text{mm}$ diameter LiNbO_3 disk with a resulting FSR of $7.6\ \text{GHz}$. A microstrip electrode is placed on top of the LiNbO_3 disk and excited with a RF field using a SMA microstrip launcher. Using a network analyzer, we tune the fundamental resonant frequency of the microstrip electrode to match the FSR of $7.6\ \text{GHz}$ by monitoring the dip in the reflected RF excitation response (Fig. 13(a)). Fig. 13(b) and (c) demonstrate the detected modulated optical power from the LiNbO_3 microphotonic modulator. We see that the $7.6\ \text{GHz}$ optical modulation is 60% that of base-band modulation as expected by simulation discussed in Section 5.1. In addition, the RF bandwidth of $150\ \text{MHz}$ matches closely with the measured optical Q of 1.3×10^6 .

5.3. Experimental results of mm-wave modulation

As indicated through simulation, modulation can be achieved at an integral number times the optical FSR of the disk by changing the period of the metal electrodes. This is demonstrated through experiment where we achieve *mm*-modulation as shown in Fig. 14(a). By modifying the resonant periodicity of the metal electrodes on a LiNbO_3 microphotonic modulator, *mm*-wave modulation at a frequency of $30.25\ \text{GHz}$ is obtained. This frequency is approximately four times the optical FSR of $7.6\ \text{GHz}$ as expected. Fig. 14(a) shows both RF and optical electrical fields simultaneously tuned on resonance. To confirm that modulation is a result of simultaneous resonance of RF and optical electric fields within the disk, we individually detune the applied RF frequency, and optical wavelength from that of resonance. In Fig. 14(b) we keep the RF on resonance, while tuning the optical wavelength off resonance, showing that there is only residual modulation at less than $-40\ \text{dB}$ as compared with the simultaneously on resonance modulation. This is a result of optical

excitation of low- Q higher-order modes while tuned off resonance. Fig. 14(c) shows complete loss of modulation as the RF electric field is detuned from resonance.

6. Conclusion

A new type of *mm*-wave RF receiver architecture with direct electrical-to-optical conversion has been described. Simulation of a microphotonic modulator which uses simultaneous resonance of optical and RF electric fields demonstrates that efficient modulation is achievable at *mm*-wave frequencies through the use of a periodic metal electrode. In addition, experimental results confirm our model and demonstrate modulation at *mm*-wave frequencies.

Acknowledgements

This work is supported in part by the National Science Foundation under contract ECS-9979331 and the DARPA RFLICs program.

References

- [1] Ohata K, Inoue T, Funabashi M, Inoue A, Takimoto Y, Kuwabara T, Shinozaki S, Maruhashi K, Hosaya K, Nagai H. IEEE Trans Microwave Theory Techn 1996;44:2354–60.
- [2] Robertson WM, Arjavalingam G, Kopcsay GV. Electron Lett 1991;27:175–6.
- [3] Properties of Lithium Niobate. EMIS Data Reviews Series No. 5. INSPEC, London. 1989 (ISBN 085296 482 X).
- [4] Tien PK, Ulrich R. J Opt Soc Am 1970;60:1325–37.
- [5] Hill SC, Benner RE. In: Barber PW, Chang RK, editors. Optical effects associated with small particles, Singapore: World Scientific; 1988. p. 3.
- [6] Braginsky VB, Ilchenko VS. Phys Lett 1989;A-137:393–7.
- [7] Kourogi M, Nakagawa K, Ohtsu M. IEEE J Quantum Electron 1993;29:2693–701.

REPORT DOCUMENTATION PAGE				Form Approved OMB No. 0704-0188	
<p>The public reporting burden for this collection of information is estimated to average 1 hour per response, including the time for reviewing instructions, searching existing data sources, gathering and maintaining the data needed, and completing and reviewing the collection of information. Send comments regarding this burden estimate or any other aspect of this collection of information, including suggestions for reducing the burden, to Department of Defense, Washington Headquarters Services, Directorate for Information Operations and Reports (0704-0188), 1215 Jefferson Davis Highway, Suite 1204, Arlington, VA 22202-4302. Respondents should be aware that notwithstanding any other provision of law, no person shall be subject to any penalty for failing to comply with a collection of information if it does not display a currently valid OMB control number.</p> <p>PLEASE DO NOT RETURN YOUR FORM TO THE ABOVE ADDRESS.</p>					
1. REPORT DATE (DD-MM-YYYY) June 15, 2004		2. REPORT TYPE Final Report		3. DATES COVERED (From - To) April 1, 2000 - March 31, 2004	
4. TITLE AND SUBTITLE Microphotonic RF Receiver Components				5a. CONTRACT NUMBER N/A	
				5b. GRANT NUMBER N00014-00-1-0458	
				5c. PROGRAM ELEMENT NUMBER N/A	
6. AUTHOR(S) Hossein-zadeh, Mani Harriague Fernando David Cohen Levi, A.F.J. (Principal Investigator)				5d. PROJECT NUMBER N/A	
				5e. TASK NUMBER N/A	
				5f. WORK UNIT NUMBER N/A	
7. PERFORMING ORGANIZATION NAME(S) AND ADDRESS(ES) University of Southern California 3620 S. Vermont Ave., KAP 132 Los Angeles, CA 90089-2533				8. PERFORMING ORGANIZATION REPORT NUMBER N/A	
9. SPONSORING/MONITORING AGENCY NAME(S) AND ADDRESS(ES) Office of Naval Research Ballston Centre Research Tower One 800 North Quincy Sreet Arlington, VA 22217-5660				10. SPONSOR/MONITOR'S ACRONYM(S) ONR	
				11. SPONSOR/MONITOR'S REPORT NUMBER(S) N/A	
12. DISTRIBUTION/AVAILABILITY STATEMENT Approved for Public Release					
13. SUPPLEMENTARY NOTES N/A					
14. ABSTRACT A novel microphotonic RF wireless receiver that exploits nonlinear modulation in a LiNbO3 microdisk to achieve direct photonic down-conversion from a RF carrier without using any high-speed electronic elements has been demonstrated. Laboratory experiments include receiving a wireless Ku band RF signal by conversion to an optical carrier, processed in the optical domain, and then extracting base band information using self-homodyne direct detection.					
15. SUBJECT TERMS microphotonic RF wireless receiver, self-homodyne direct detection, optical signal processing					
16. SECURITY CLASSIFICATION OF:			17. LIMITATION OF ABSTRACT	18. NUMBER OF PAGES	19a. NAME OF RESPONSIBLE PERSON
a. REPORT U	b. ABSTRACT U	c. THIS PAGE U			Lourdes Creus, Contracts & Grants Administrator
					19b. TELEPHONE NUMBER (Include area code) (213) 740-6058